Seismic Performance Characterization of Beams with High-Strength Reinforcement

Duy V. To

Jack P. Moehle

Department of Civil and Environmental Engineering

University of California, Berkeley

December 2017

Performance Characterization of Beams with High-Strength Reinforcement

Principal Investigator: Dr. Jack P. Moehle

Graduate Student Researcher: Duy V. To

ACKNOWLEDGEMENT

ABSTRACT

A laboratory test and analytical research program was undertaken to characterize the performance of reinforced concrete beams with high-strength reinforcement subjected to reversed cyclic lateral loading simulating earthquake effects. The beams are representative of beams used in special moment frames. Four beams were tested in the laboratory test investigation, one with A706 Grade 60 reinforcement, one with Grade 100 reinforcement having tensile-to-yield strength ratio (T/Y) of 1.18, one with Grade 100 reinforcement with T/Y = 1.30, and one with A1035 Grade 100 reinforcement. In each beam, the noted reinforcement grade was used for both longitudinal and transverse reinforcement. Overall, all beams achieved rotation capacity of at least 0.045 radians. The beams with A706 Grade 60 and Grade 100 (T/Y = 1.30) reinforcement failed by buckling of longitudinal bars over several hoop spacings. The other two beams with Grade 100 reinforcement failed by fracture of longitudinal bars at the maximum moment section. Strain gauges installed on longitudinal bars indicated that beams with higher T/Y achieved greater spread of plasticity compared to beams with lower T/Y.

In the analytical study, the seismic performance of tall reinforced concrete special moment resisting frames with high-strength reinforcement was investigated through nonlinear dynamic analyses. Four 20-story reinforced concrete moment frames, three reinforced with Grade 100 steel and one with Grade 60 steel were designed in accordance with ASCE 7-16 and ACI 318-14 at a hypothetical site in San Francisco, California. All four frames had the same dimensions and concrete properties, resulting in identical design drifts. Frames with Grade 100 reinforcement were designed to have reduced amount of longitudinal reinforcement to provide equivalent nominal strength as was provided in the Grade 60 reinforcement model. Tests had demonstrated that frames with higher-grade reinforcement had greater strain penetration into beam-column joints, resulting in greater slip of reinforcement from connections. This effect combined with reduced reinforcement ratios caused the frames with Grade 100 reinforcement to be more flexible than the frame with Grade 60 reinforcement. In addition, some currently available types of Grade 100 reinforcement have lower tensile-to-yield strength ratio and lower uniform elongation compared with Grade 60 reinforcement. The reduced T/Y results in reduced strain-hardening, increased strain localization, and increased P-Delta effects. The effects of these local behaviors on overall frame performance are studied through the nonlinear dynamic analyses. The various types of reinforcement were found to result in minor differences in overall frame seismic performance.

TABLE OF CONTENTS

LIST OF FIGURES

LIST OF TABLES

1. INTRODUCTION

1.1. MOTIVATION

The use of higher grade reinforcing steel has the potential benefit of reducing material quantities, thereby leading to reduced reinforcement congestion and reduced construction costs in reinforced concrete construction. Several steel mills in the United States can produce reinforcing steel of grade 100 (nominal yield strength of 100 ksi) and higher. However, at the time of this writing, none of these higher grades can match the benchmark mechanical properties of Grade 60 A706 steel. This raises questions about the performance characteristics of reinforced concrete construction that uses the higher-grade reinforcement.

Figure 1.1.1 depicts typical stress-strain behaviors of A706 Grade 60 reinforcement and three different types of Grade 100 reinforcement. The stress-strain relations were obtained from tests of reinforcing bars used in the present study. Of note are differences in the yield point characteristics, tensile-to-yield strength ratios (T/Y), and ultimate uniform elongations (defined as the strain at the ultimate stress). The A706 Grade 60 reinforcement shows a defined yield plateau with T/Y = 1.45 and ultimate elongation of 14% (ASTM A706-16). Two of the Grade 100 bars also show a defined yield plateau, but with reduced T/Y (1.30 and 1.18, respectively) and reduced ultimate elongation (9.4% and 6.8%, respectively). The third Grade 100 reinforcement (A1035) does not have a defined yield plateau but instead has a roundhouse curve with high T/Y and ultimate elongation around 0.05. The lower T/Y is believed to reduce the spread of plasticity in a beam after onset of yielding, and that effect combined with reduced elongation may result in lower rotational capacity of reinforced concrete members with some types of higher-grade reinforcement.

The primary motivation of this research is to explore the seismic performance characteristics of beams constructed of higher-grade reinforcement. The study includes both laboratory tests to characterize the beam behavior and numerical studies to understand the effects on seismic performance of multi-story frames.
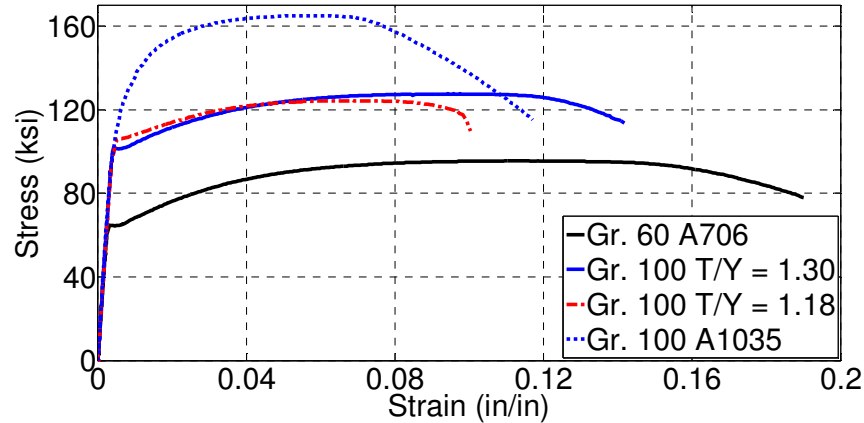
Figure 1.1.1: Mechanical Properties of Grade 60 and Grade 100 Steels

1.2. OBJECTIVES AND SCOPE

The objective of this study is to characterize and quantify the seismic performance of reinforced concrete beams typical of those used in special moment frames reinforced with high-strength steel bars having yield strength of 100 ksi. The scope includes both laboratory testing of representative beams and numerical modeling of archetype buildings using high-strength reinforcement.

The laboratory tests include tests on four representative beams. For an individual beam, longitudinal and transverse reinforcement uses one of the four types shown in Figure 1.1.1. The beams are designed to have nominally identical moment strengths, with nominal shear strengths exceeding the maximum shear expected during the test. The tests specimens are instrumented to record overall load-deformation behavior, as well as spread of plasticity, inelastic rotation capacity, longitudinal reinforcement buckling characteristics and related requirements for transverse reinforcement, and local bond stress-slip relationships for reinforcement anchored in adjacent connections.

The numerical study begins with development of numerical models for each of the beams, including relatively simple models for stiffness, strength, and deformation capacity, as well as relatively complex models to represent the reversed-cyclic behavior of the beams under force reversals. Additionally, four 20-story reinforced concrete moment frames, three reinforced with Grade 100 reinforcement and one reinforced with A706 Grade 60 reinforcement, are designed in accordance with ASCE 7-16 and ACI 318-14 at a hypothetical site in San Francisco, California. Nonlinear dynamic analyses are carried out to investigate the seismic performance characteristics of tall, reinforced concrete special moment resisting frames with Grade 60 and Grade 100 reinforcement.

2. LABORATORY TEST PROGRAM

Important and general information about the laboratory test program is presented in this chapter including test specimen design, test setup and apparatus, instrumentation, preliminary estimate of load-resisting capacity, and loading procedure. More details on actual dimensions, actual material properties, instrumentation, loading protocols, data acquisition systems, and data reduction methods are described in Appendix A.

2.1. TEST SPECIMEN DESIGN

All four beams were designed to have cross section and span that are up-scaled (scale factor is 1.5) from beam specimens previously tested by Ma and Bertero (Ma et al., 1976) that used conventional A615/706 Grade 60 reinforcing bars having T/Y equal to 1.45. Three of the four beams in this experimental program have Grade 100 longitudinal reinforcement, in which two have yield plateau and the other one has round-hound shape in stress-strain relation (Table 2.1.1). The fourth beam was reinforced longitudinally with conventional Grade 60 A706 steel. All longitudinal steel was laterally supported by hoops and crossties of the same grade steel used in each test specimen, except Beams SBL100 and SBH100. They both had the same transverse reinforcement, which was Grade 100 with distinct yield plateau and T/Y of 1.30.

The beam designs were also to result in low nominal shear stress (approximately $3\sqrt{f_c'}\ psi$), which was to minimize shear cracking along with associated effect of increasing tension shift (Park and Paulay, 1975) and rotation capacity (Moehle, 2014). The design also satisfied confinement requirements of ACI 318 for special moment resisting frame (SMRF) beams with spacing being reduced to $5d_b$ as recommended (ATC-98, 2014) for higher strength reinforcement with smaller T/Y ratio. For Beam SBH60 with No. 9 Grade 60 A706 longitudinal reinforcement, the transverse steel spacing was governed by a quarter of section depth per ACI 318-14, which also resulted in 5-inch spacing. Concrete was normal weight with design compressive strength of 5,000 psi. Table 2.1.1 summarizes the design and material properties used during design process. Figure 2.1.2 through Figure 2.1.4 display the general design drawings of test specimens in this research program and that by Ma and Bertero, respectively.

Similar high-strength reinforcing bars with distinct yield plateau of No. 8 bar size have been tested in the laboratory at University of Texas, Austin in a companion research program. Early test data on mechanical properties of these types of Grade 100 reinforcement have been shared with UC Berkeley for the purpose of estimating expected moment and shear strength of our test beams. Grade 100 A1035 mechanical properties are taken from previous research (Rautenberg et al., 2013). Grade 60 A706 expected yield and tensile strengths are taken to be 69 ksi and 95.2 ksi, respectively (Bournonville et al., 2004). These mechanical properties of reinforcing bars and specified concrete strength of 5,000 psi are used to calculate expected moment and shear strength of test specimens (Table 2.1.1).

Table 2.1.1: Summary of Design and Material Properties of Test Specimens Used During Design

Author	Ma, Bertero & Popov	To & Moehle			
Specimen name	BEAM R-6	SBL100	SBH100	SBM100	SBH60
Scale factor		1.5	1.5	1.5	1.5
Width (in)	9	13.5	13.5	13.5	13.5
Height (in)	16	24	24	24	24
Length (in)	62.5	93.75	93.75	93.75	93.75
Effective depth (in)	14	22.125	22.125	22.125	22.125
f_c' (ksi)	4	5	5	5	5
Longitudinal reinforcement					
Top reinforcement	4 No. 6	3 No. 8	3 No. 8	3 No. 8	4 No. 9
Bottom reinforcement	4 No. 6	3 No. 8	3 No. 8	3 No. 8	4 No. 9
Type of steel	ASTM A615				ASTM A706
Grade	60	100	100	100	60
f_y (ksi)	66	100	100	100	60
f_t (ksi)	95	118	130	140	87.6
Tensile-to-yield strength ratio T/Y	1.45	1.18	1.30	1.40	1.46
Transverse reinforcement	4 No. 2	3 No. 4	3 No. 4	3 No. 4	4 No. 4
Hoop & crosstie spacing (in)	3.5	5	5	5	5
Grade	60	100	100	100	60
f_y (ksi)	66	100	100	100	60
f_t (ksi)	95	130	130	140	87.6
T/Y ratio	1.44	1.30	1.30	1.40	1.46
Shear strength from transverse steel (kips) [*]	47.12	258	258	258	206
Expected Strength					
f_y (ksi)	65.5	105	101	120	69
f_t (ksi)	94.2	124	128.5	168	95.2
Yield moment strength of beam (kips-in)	1500	4916	4739	5577	5435
Probable moment strength of beam (kips-in) [*]	1844	5752	5947	7617	7383
Shear demand (kips) [*]	29.5	61.4	63.4	81.2	78.8
Nominal shear stress [**]	$3.5\sqrt{f_c'}$	$3.0\sqrt{f_c'}$	$3.1\sqrt{f_c'}$	$4.0\sqrt{f_c'}$	$3.8\sqrt{f_c'}$

[*]Strength calculations are in accordance with procedures defined in ACI 318-14 for special moment frame beams.

[**]This report uses the inch-lb measurement system, in which f_c' is in units of psi.

In Table 2.1.1, moment strengths and shear demand of Beam R-6 were taken directly from test data reported in Ma et al. (1976). Those shown for beams SBH60, SBH100, SBL100, and SBM100 were estimated based on simple moment strength calculations with the assumption that concrete reached crushing strain of 0.003 (ACI 318-14). Shear demand was calculated using probable moment strength and shear stress was determined as

$$v = \frac{V}{b_w d \sqrt{f_c'}} \qquad \text{Eq. (1)}$$
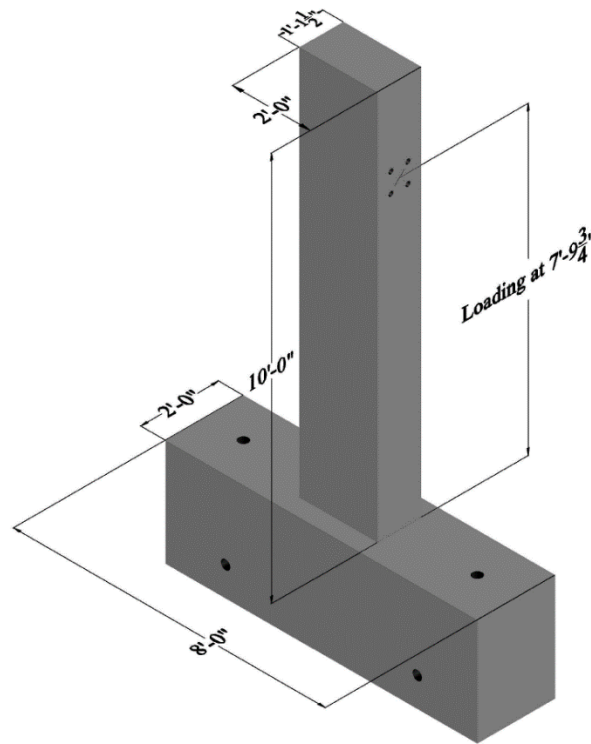
Figure 2.1.1: Geometry and Dimensions of Test Beam Designs
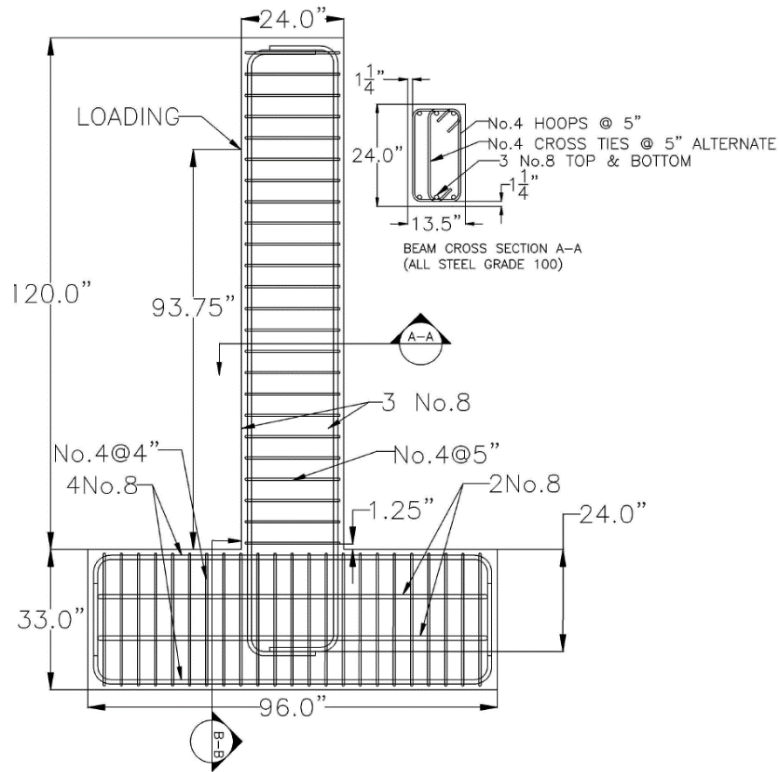
Figure 2.1.2: Reinforcement Details for Beams SBL100, SBH100, and SBM100
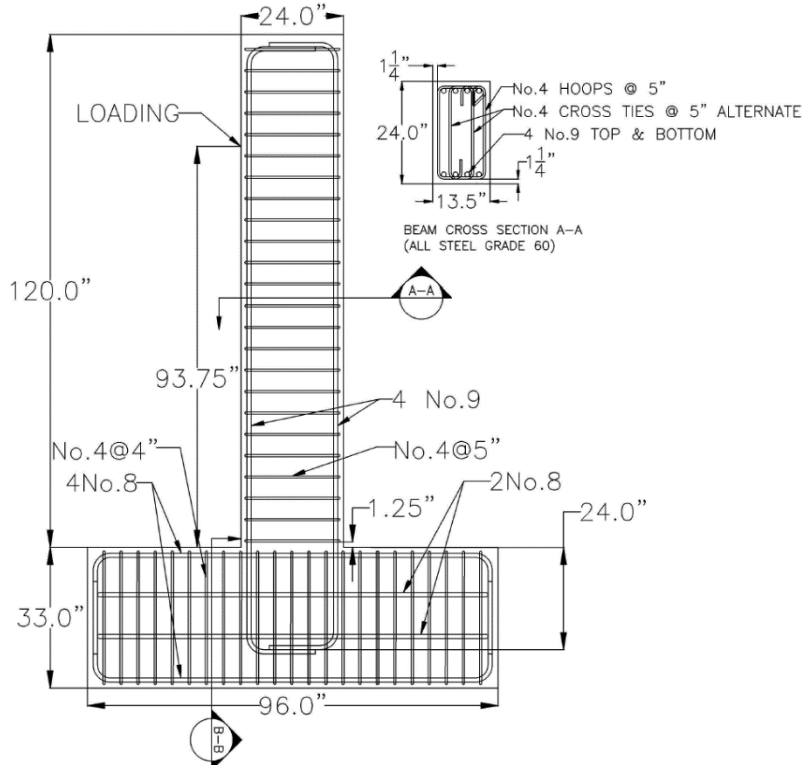
Figure 2.1.3: Reinforcement Details for Beam SBH60

18
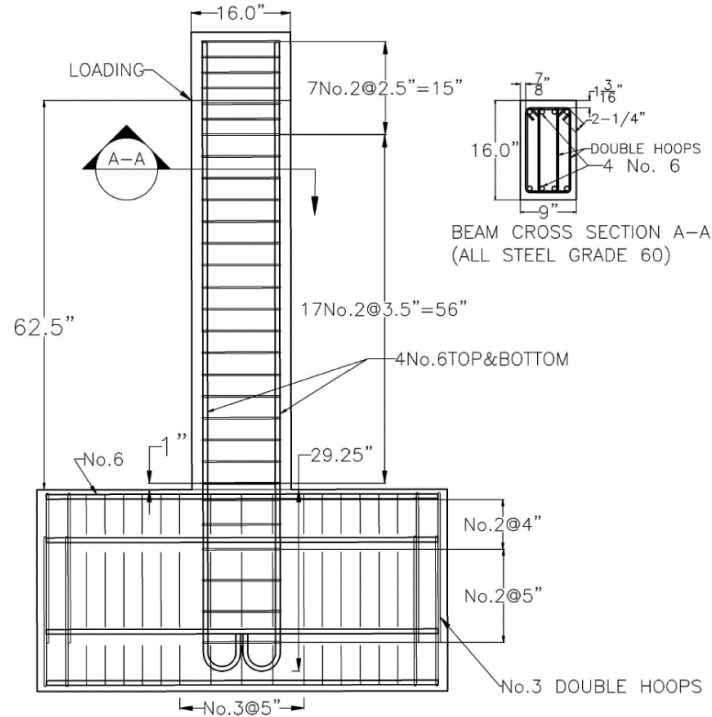
Figure 2.1.4: Reinforcement Details for Beam R-6 (Ma et al.) (Drawing has been redone for clarity)

2.2. TEST PROCEDURE

Cured specimens were oriented vertically and anchored down on the strong floor of the laboratory (Figure 2.2.1 & Figure 2.2.2). Since each hole on the strong floor has nominal capacity of 100 kips under tension, two large W-section steel beams were used to engage three holes on each side of test beam, resulting in total of 450 kips on each side (post-tensioning at the middle hole directly compressed together the concrete block and the floor, enabling a peak post-tensioning force of 250 kips). The anchorage force on both sides together created large enough friction on the interface between test specimen and laboratory floor to resist sliding caused by applied lateral load on top of the beam.

Two actuators were used to apply reversed cyclic lateral load on the specimen. Each of actuators formed an angle of about sixty (60) degrees with the horizontal steel beam on the reaction frame and was connected to the specimen through a loading fixture to restrain accidental out-of-plane bending of the specimen during test.
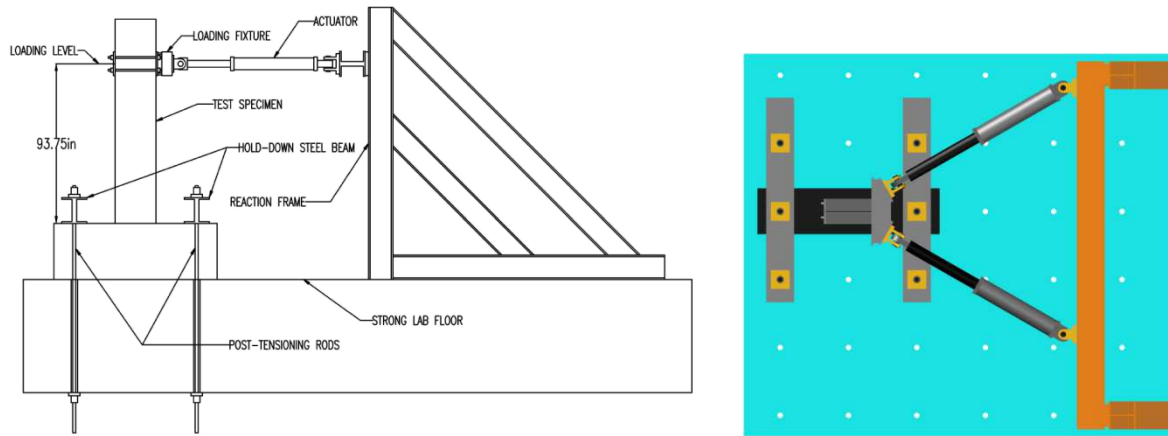
Figure 2.2.1: Schematic test setup – Left: Elevation View; Right: Plan View
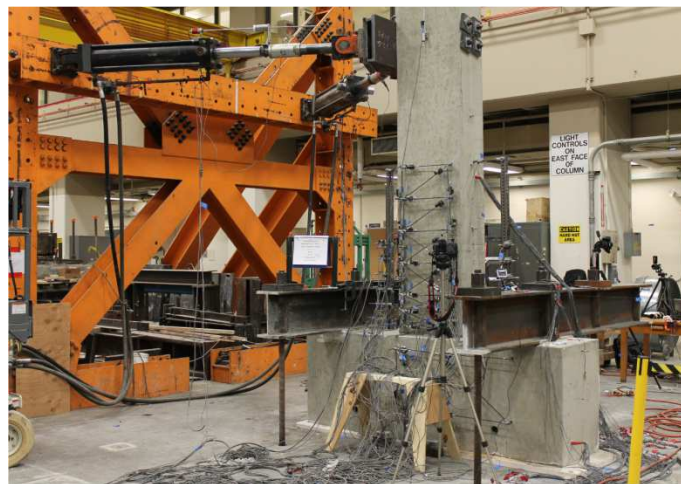
Figure 2.2.2: General Test Setup

Strain gauges were installed onto reinforcing bars as interior instrumentation. Typical locations of these strain gauges are shown in Figure 2.2.3. These strain gauges were installed to measure strain primarily along middle longitudinal bars on both sides of beam, hoops and crossties, and along anchorage length of middle longitudinal bars.

Exterior instrumentation included displacement transducers set up to measure global deflection and local deformations along test specimen length (Figure 2.2.4). Global deflection was measured by wire potentiometers. Lateral force was measured by load cells attached on two actuators that were used to apply force on test specimens. The total force was the sum of the force measured by two load cells projected on direction of loading. Local deformation was measured by LVDTs. From a truss system of LVDTs as shown in Figure 2.2.4, total deformation was computed from measurement of local deformation based on principle of virtual force (Appendix A).

20
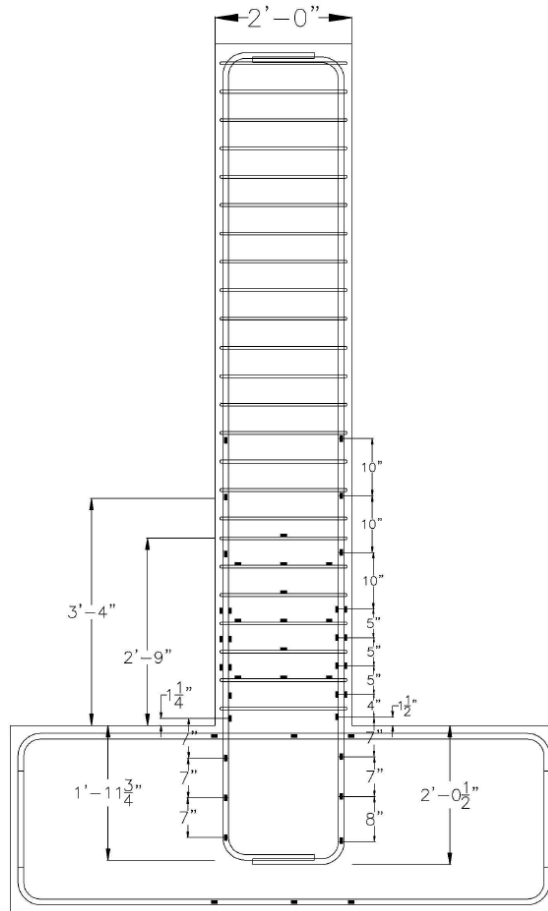
Figure 2.2.3: Interior Instrumentation – Strain Gauges
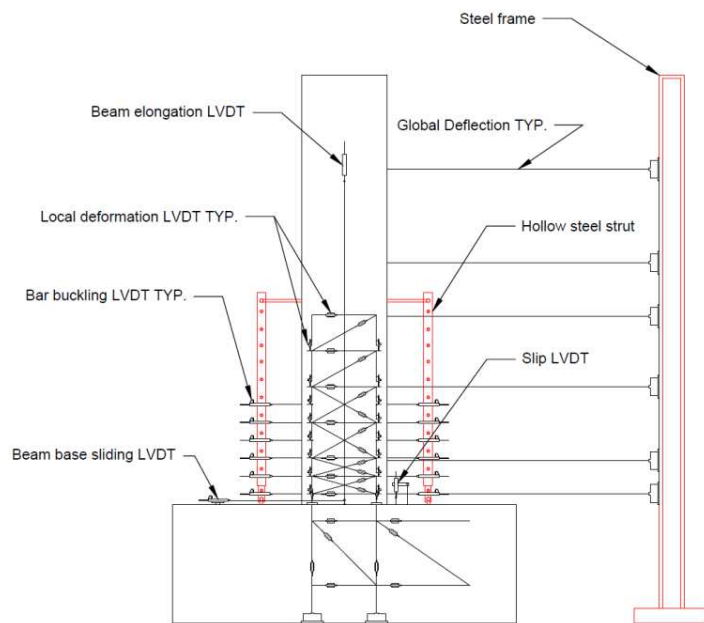
Figure 2.2.4: Schematic Drawing of Exterior Instrumentations

The loading history was developed based on recommendations of FEMA 461 (FEMA, 2007). It consists of two major loading types: load controlled, and displacement controlled. Figure 2.2.5 displays a typical loading time series being imposed on test specimens. More details on loading protocol can be found in Appendix A. For each loading amplitude of either force- or displacement-controlled, the test beams were loaded from initial position to the peak in East direction first, followed by another peak in the West direction, and one cycle was completed by loading the beam back to initial position. The test was stopped for marking cracks when the specimen was loaded to the peak on the East, and West direction of the first cycle, and the end of loading cycles (either second or third) when the pre-determined applied load or displacement became zero.
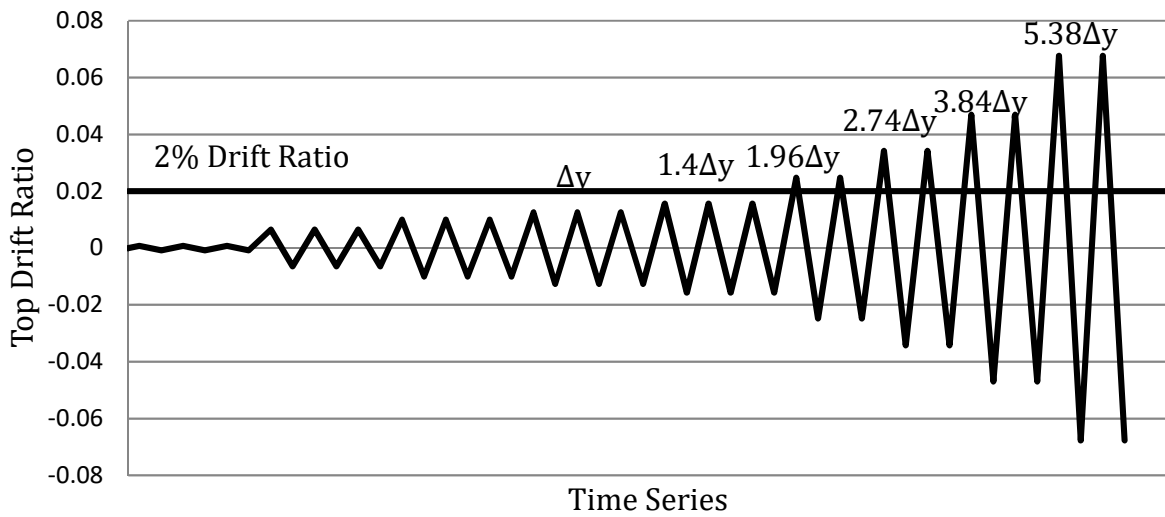
Figure 2.2.5: Loading History

3. TEST RESULTS

3.1. GENERAL OBSERVATIONS

Important observations on both beams tests are summarized below:

1) Flexural cracks in all beams were first observed at loads of approximately 60 percent of yield force.
2) Flexural crack patterns were similar in either direction of loading.
3) From the beginning of test to the end of loading stage of 1.96Δy, curvature was visibly apparent along the length of all of the beams.
4) After several loading cycles of large displacement and starting from loading stage of 2.744Δy, a couple of major large cracks opened up and caused significant shear distortion in beams SBH100 and SBL100. Also, importantly, beam SBL100 started to have concentrated rotation at the base, giving the appearance that the rest of the beam remained straight to eyes.
5) All beams yielded when loaded to pre-computed force corresponding to nominal yield stress of reinforcement. Peak strain in longitudinal reinforcement measured by strain gauges also indicated yield strain of approximately 0.002 and 0.0034 for Grade 60 and Grade 100 reinforcement, respectively.
6) Beam SBH60 with conventional Grade 60 A706 reinforcement yielded at drift ratio of 0.9%, which is lower than the others with Grade 100 steel yielding at drift ratio of 1.25%.
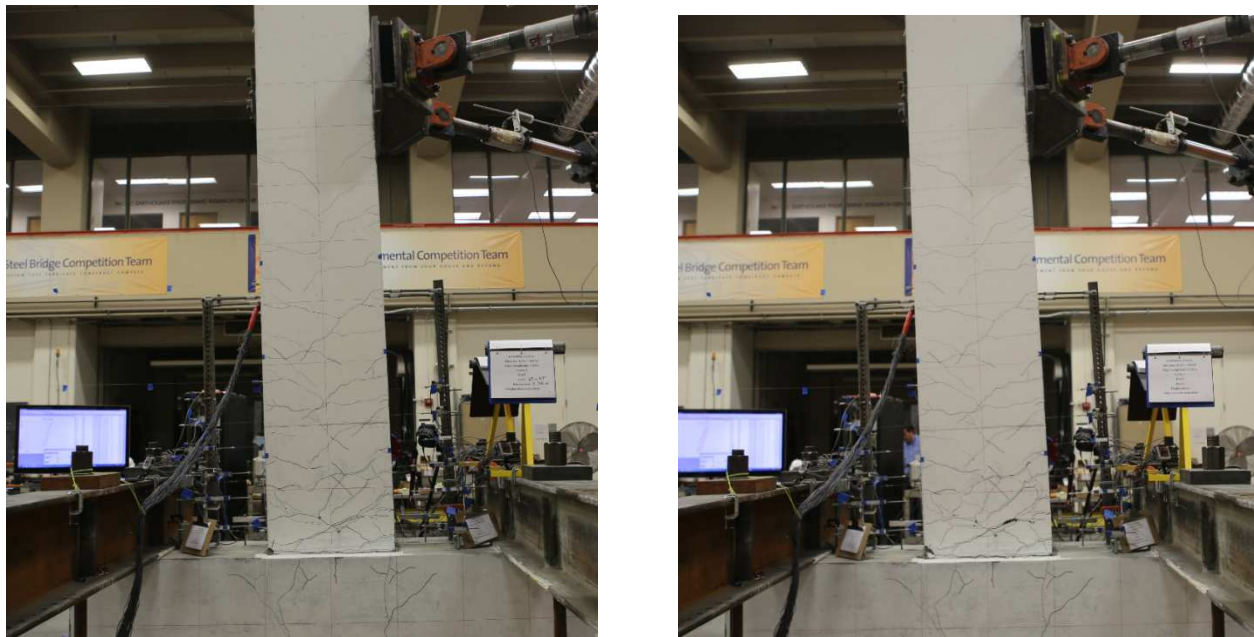
Figure 3.1.1: Deflected Shape of SBH60 at Drift Ratio 2.45% (Left) and 3.45% (Right)

Figure 3.1.2: Deflected shape of SBH100 at Drift Ratio 2.45% (Left) and 3.45% (Right).

Figure 3.1.3: Deflected shape of SBL100 at Drift Ratio 2.45% (Left) and 3.45% (Right).

Figure 3.1.4: Deflected shape of SBM100 at Drift Ratio 2.45% (Left) and 3.45% (Right).

3.2. CRACK DEVELOPMENT

First cracks were observed to occur when test specimens were loaded to 0.6% drift ratio in all tests, except for test of beam with Grade 60 reinforcement, in which first cracks were visible at 0.35% drift ratio. These cracks were primarily horizontal, consistent with expectations for flexure-dominated cracks. As loading progressed, several inclined cracks appeared, consistent with expectations for combined flexure and shear. Figure 3.2.1 through Figure 3.2.4 depict development of cracks. Table 3.2.1 and Table 3.2.2 show crack widths measured during tests on the East and West sides of test beams, respectively.
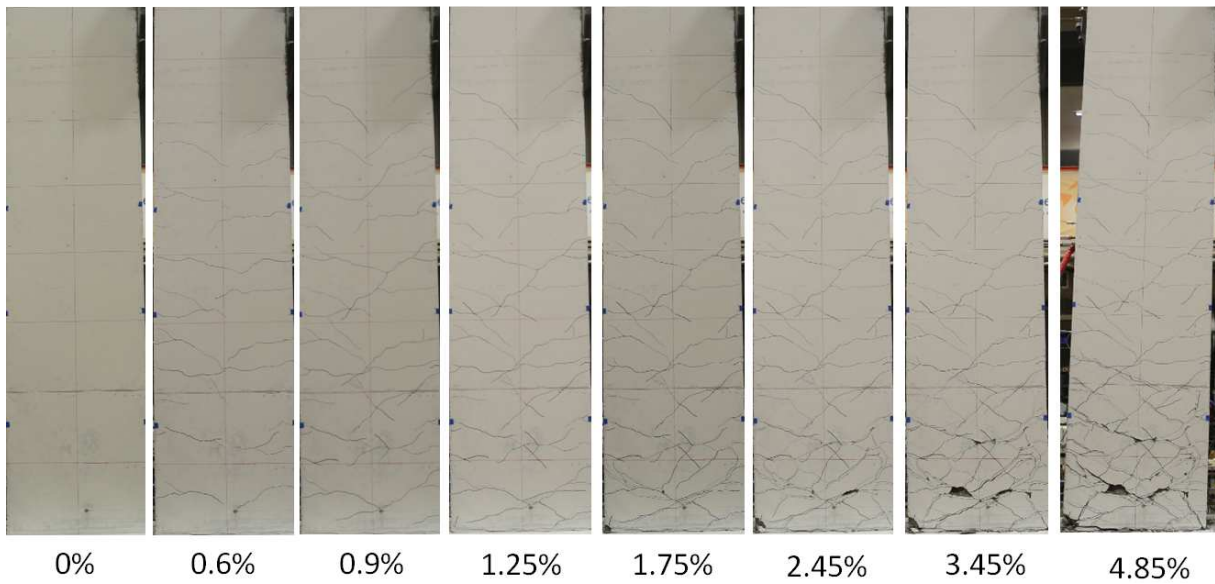
Figure 3.2.1: Crack Development on SBH60
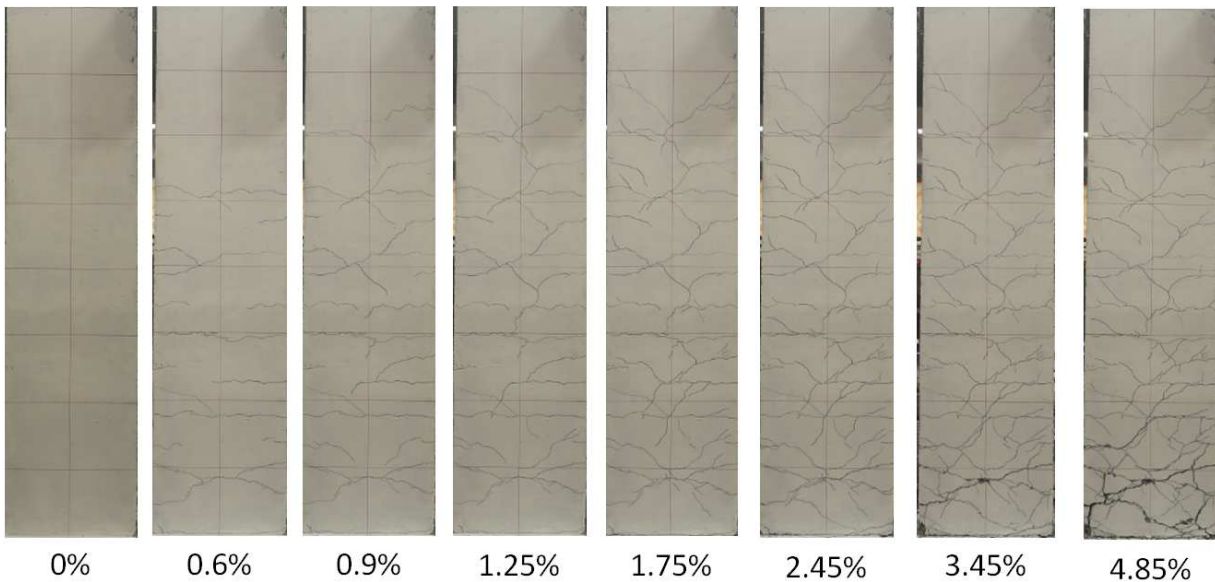
Figure 3.2.2: Crack Development on SBH100

| 0% | 0.6% | 0.9% | 1.25% | 1.75% | 2.45% | 3.45% | 4.85% |
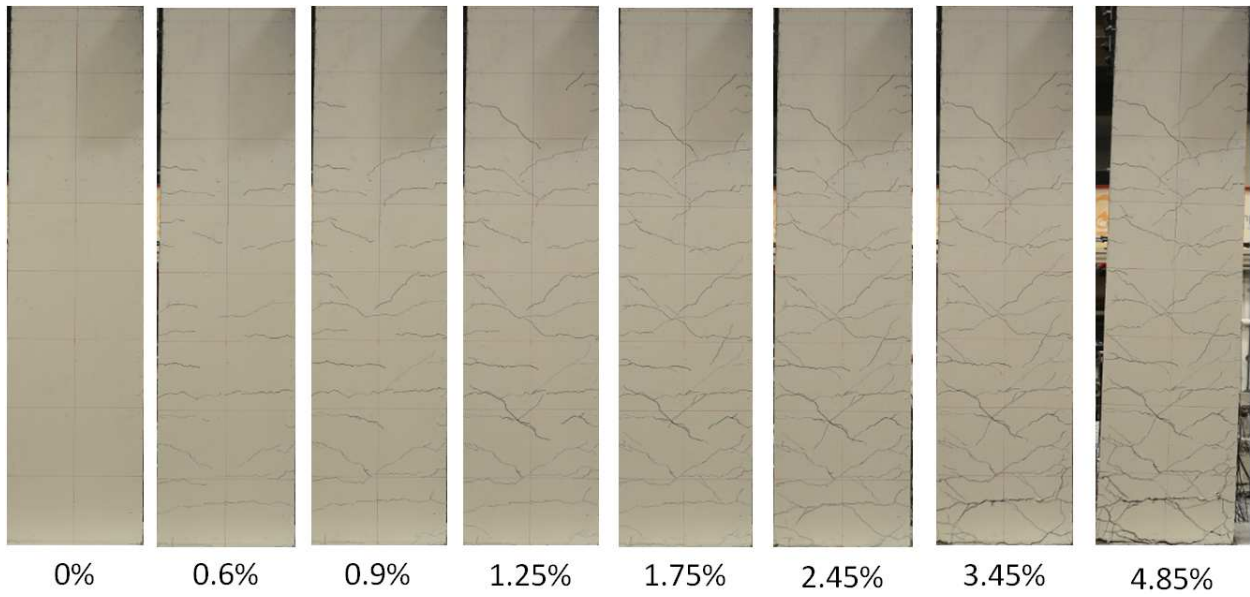
Figure 3.2.3: Crack Development on SBL100

| 0% | 0.6% | 0.9% | 1.25% | 1.75% | 2.45% | 3.45% | 4.85% |
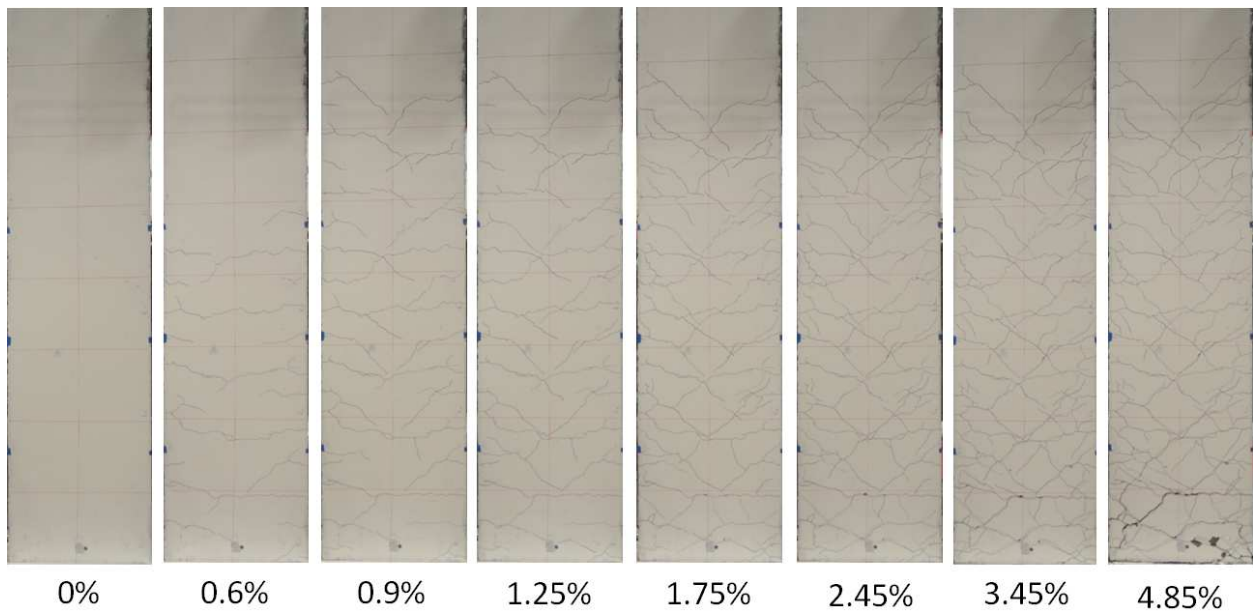
Figure 3.2.4: Crack Development on SBM100

Table 3.2.1: Measured Crack Widths on East Side (Loading to West direction)

Drift Ratio	Location (percentage of beam length)*	Crack Width (inch)			
		SBH60	**SBH100**	**SBL100**	**SBM100**
0.6%	100	0.016	0.005	0.020	0.000
	80	0.008	0.010	0.010	0.008
	60	0.008	0.005	0.005	0.005
	40	0.008	0.000	0.010	0.005
0.9%	100	0.035	0.047	0.030	0.000
	80	0.012	0.015	0.015	0.012
	60	0.008	0.010	0.010	0.012
	40	0.008	0.010	0.010	0.008
1.25%	100	0.040	0.110	0.050	0.030
	80	0.012	0.025	0.025	0.020
	60	0.008	0.010	0.010	0.020
	40	0.008	0.015	0.015	0.012
1.75%	100	0.070	0.156	0.075	0.060
	80	0.012	0.030	0.030	0.020
	60	0.012	0.015	0.015	0.016
	40	0.012	0.015	0.020	0.012
2.45%	100	0.125	0.156	0.110	0.094
	80	0.035	0.075	0.040	0.040
	60	0.016	0.015	0.015	0.030
	40	0.012	0.015	0.015	0.016
3.45%	100	0.219	0.175	0.180	0.125
	80	0.070	0.140	0.050	0.060
	60	0.012	0.015	0.020	0.020
	40	0.012	0.020	0.015	0.016
4.85%	100	0.313	0.220	0.250	0.219
	80	0.125	0.188	0.075	0.094
	60	0.012	0.015	0.020	0.040
	40	0.012	0.020	0.020	0.016

*: This location of the crack with measured width is at a distance as a percentage of beam length (beam length is 93.75 inches) away from application of lateral load.

Table 3.2.2: Measured Crack Widths on West Side (Loading to East direction)

Drift Ratio	Location (percentage of beam length)	Crack Width (inch)			
		SBH60	**SBH100**	**SBL100**	**SBM100**
0.6%	100	0.012	0.063	0.025	0.000
	80	0.012	0.010	0.010	0.012
	60	0.008	0.010	0.005	0.012
	40	0.005	0.000	0.005	0.005
0.9%	100	0.025	0.094	0.050	0.000
	80	0.016	0.015	0.015	0.016
	60	0.008	0.015	0.00	0.016
	40	0.005	0.005	0.010	0.012
1.25%	100	0.050	0.125	0.050	0.040
	80	0.016	0.010	0.025	0.025
	60	0.008	0.020	0.010	0.020
	40	0.005	0.005	0.010	0.012
1.75%	100	0.050	0.188	0.075	0.094
	80	0.012	0.030	0.025	0.040
	60	0.008	0.020	0.010	0.020
	40	0.008	0.005	0.015	0.012
2.45%	100	0.125	0.156	0.180	0.094
	80	0.060	0.120	0.020	0.030
	60	0.008	0.025	0.010	0.016
	40	0.005	0.005	0.015	0.012
3.45%	100	0.188	0.250	0.250	0.156
	80	0.070	0.188	0.050	0.080
	60	0.012	0.030	0.005	0.020
	40	0.008	0.005	0.015	0.012
4.85%	100	NR*	0.313	0.250	0.344
	80	NR*	0.313	0.020	0.094
	60	NR*	0.025	0.000	0.040
	40	NR*	0.005	0.000	0.020

*: Width was not measured for these cracks at this loading stage as condition of test beam was deemed too dangerous to measure crack width

3.3. FAILURE MODES

Specimen SBH60 with conventional Grade 60 A706 steel failed by twisting of the entire beam about its longitudinal axis after it achieved rotation capacity of 4.85% drift ratio. This phenomenon was associated with overall instability of the flexural compression zone (Figure 3.3.1). Beam SBH100 with Grade 100 T/Y = 1.30 also failed by beam twisting after buckling of all three longitudinal bars on one side over several hoop spacings were observed in previous loading cycle (Figure 3.3.2).

Both beams SBL100 and SBM100 failed by fracture of longitudinal bars (Figure 3.3.3 and Figure 3.3.4). On the loading cycle to 4.85% drift ratio, specimen SBL100 had the first bar fracture while SBM100 was observed to have bar necking. During the last loading stage to target drift ratio of 6.8%, the remaining two bars on the same side of first fracture in beam SBL100 ruptured, and all three longitudinal bars in SBM100 ruptured simultaneously. Table 3.3.1 summarizes the failure mechanism of all test specimens. Values in Table 3.3.1 indicate the drift ratio that test specimens had achieved before failure was observed.

Table 3.3.1: Failure Mechanisms of Test Beams

	Specimen			
Failure Mode	SBH60	SBH100	SBL100	SBM100
Bar Buckling		4.85%		
Global Instability	4.85%	6.80%		
Bar Fracture			4.85%	4.85%

Figure 3.3.1: Failure Mechanism of SBH60 by Twisting of Beam (Global Instability)

Figure 3.3.2: Failure Mechanism of SBH100 by Buckling of Longitudinal Bars Over Several Hoop Spacings

Figure 3.3.3: Failure Mechanism of SBL100 by Fracture of Longitudinal Bars

Figure 3.3.4: Failure Mechanism of SBM100 by Fracture of Longitudinal Bars

3.4. OVERALL FORCE-DEFORMATION RELATONS

Overall force-deformation relations of all test specimens are presented in Figure 3.4.1 through Figure 3.4.4. Figure 3.4.5 shows the envelopes of these force-deformation relations. It is apparent that all beams have equivalent yield strength as intended (the scaled values of the quantity $A_s f_y$ were the same for all beams). The three beams with Grade 100 reinforcement are less stiff than the one with conventional Grade 60 as expected due to lower reinforcement ratio. Specimens SBH60 and SBM100 had higher peak strength than the other two Grade 100 beams because Grade 60 A706 and Grade 100 A1035 reinforcement have more strain-hardening. All test beams had achieved at least 4.5% drift ratio in rotation capacity.
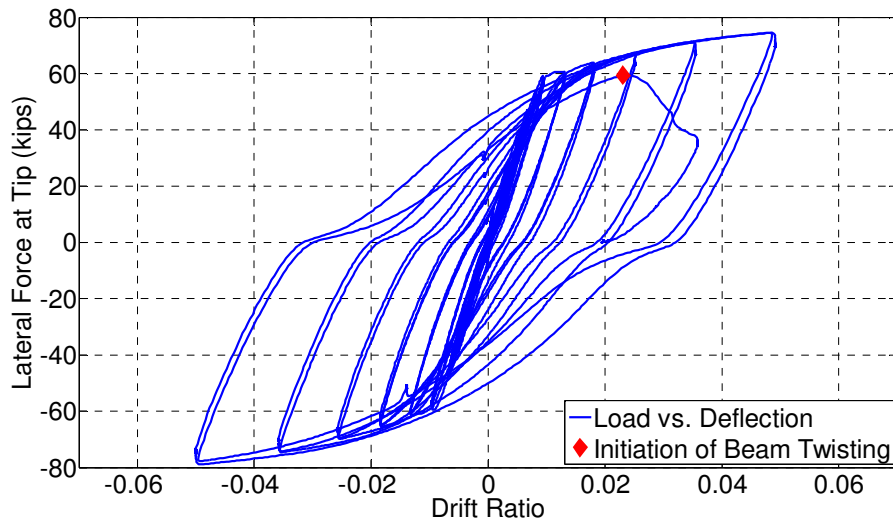
Figure 3.4.1: Lateral Force vs. Deformation – SBH60
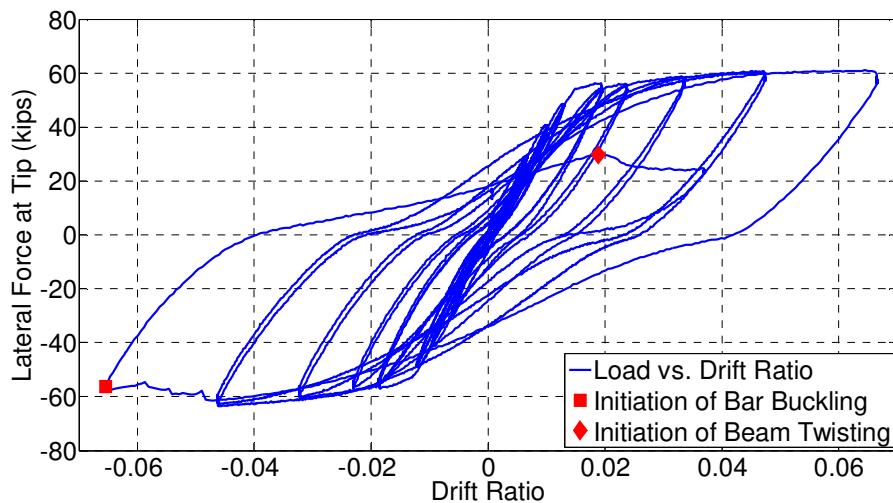
Figure 3.4.2: Lateral Force vs. Deformation – SBH100

32
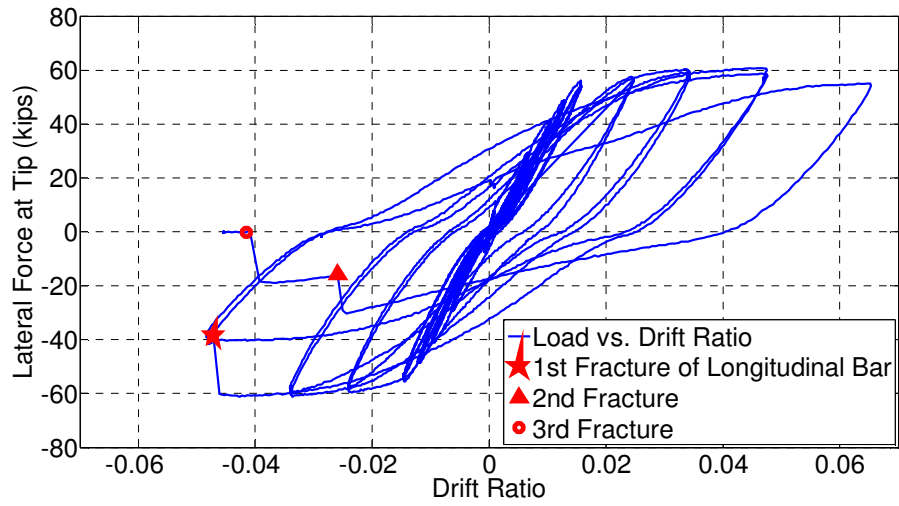
Figure 3.4.3: Lateral Force vs. Deformation – SBL100
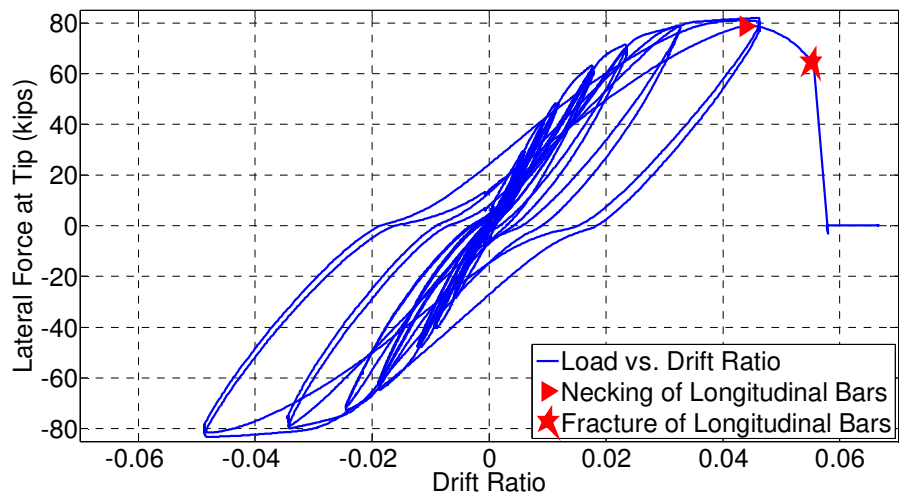
Figure 3.4.4: Lateral Force vs. Deformation – SBM100
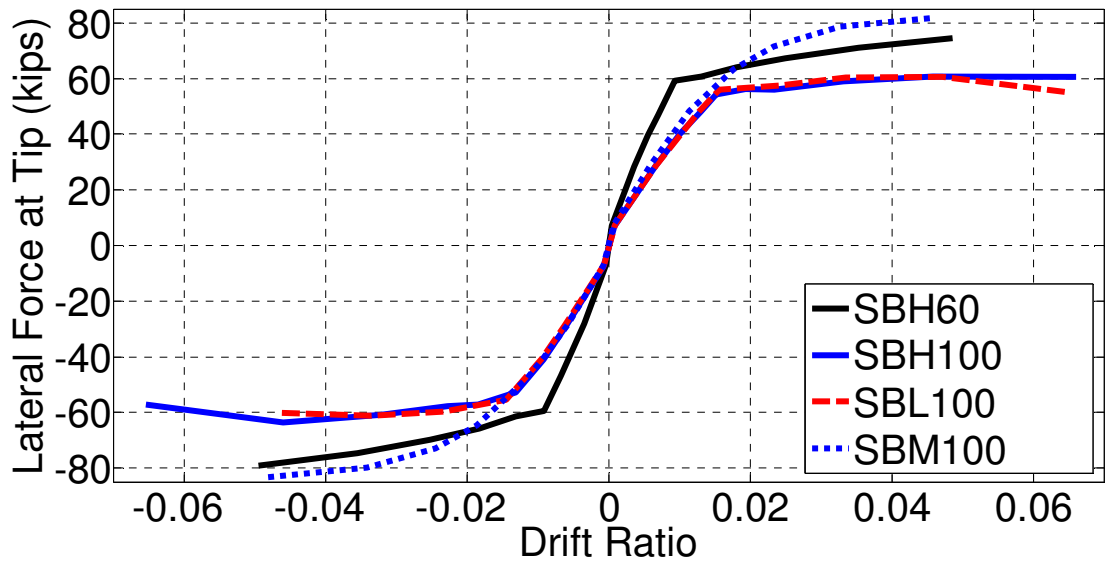
Figure 3.4.5: Force-Deformation Envelopes

3.5. DEFORMATION COMPONENTS

Total deformation of all test specimens was separated into three major components including flexural, shear, and slip by applying the principle of virtual forces to the grid of displacement transducers affixed to the side face of each beam (APPENDIX A). These three major components of deformation are plotted in Figure 3.5.1 through Figure 3.5.4 for all four beams. It is worth noting that the contribution of flexural deformations was slightly greater for beam SBH60 with Grade 60 reinforcement than for the other beams with Grade 100 reinforcement. This may be partly attributable to the higher T/Y ratio for the Grade 60 reinforcement, which tends to spread inelastic flexural deformations along a greater length of the beam. It may also be partly due to the greater contribution of slip in the beams with Grade 100 reinforcement. In all beams, shear deformation provided as much as 5-8% of total deformation.
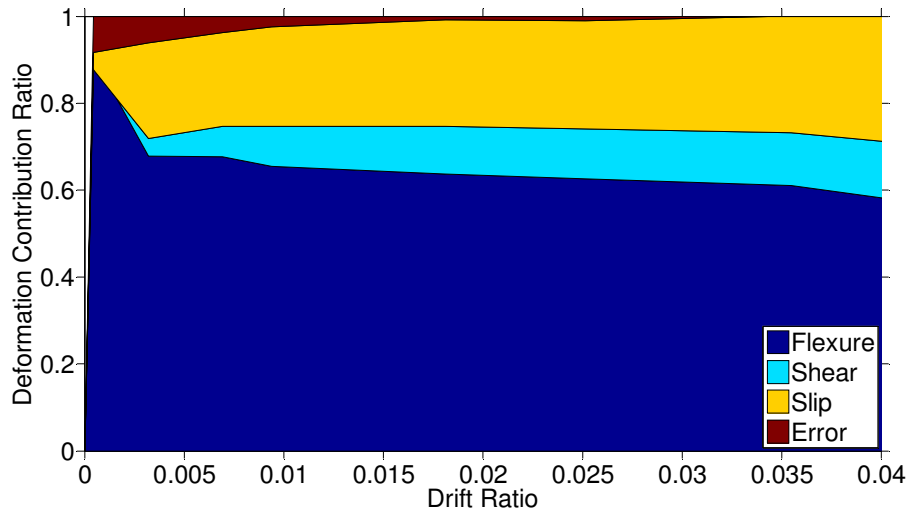
Figure 3.5.1: Deformation Components – SBH60
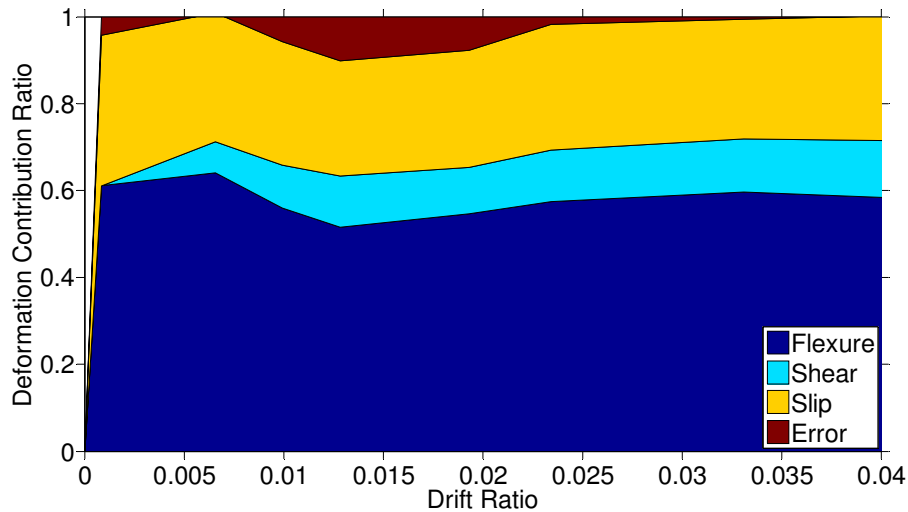
Figure 3.5.2: Deformation Components – SBH100
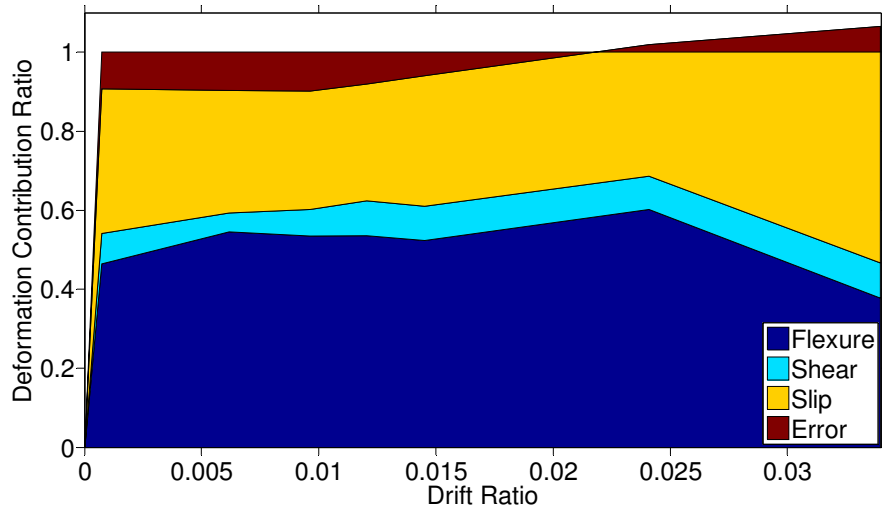
Figure 3.5.3: Deformation Components – SBL100
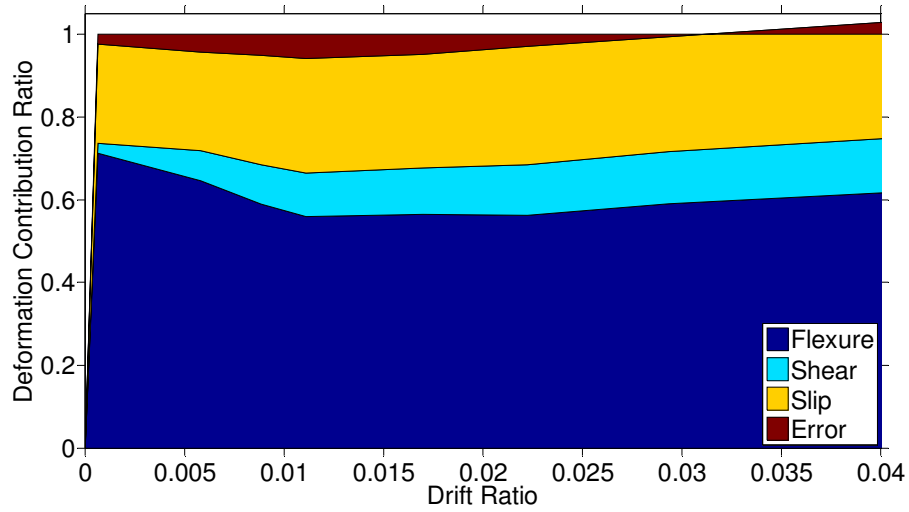
Figure 3.5.4: Deformation Components – SBM100

3.6. SPREAD OF PLASTICITY

The strain profile of the longitudinal reinforcement along the height of a beam was examined to identify if there was a trend for varying types of reinforcement. Figure 3.6.1 presents typical results, in this instance for the 1st loading cycle to drift ratio of 4.85%. Comparing the profiles of beams SBH100 and SBL100, it is apparent that strain is more localized and concentrated at the base of the beam having lower T/Y. A direct consequence of the localized strains is that the beam having lower T/Y has higher maximum strain under the same drift demand. It is also observable that the peak strain at the base is almost the same for beams SBH60 and SBH100 even though conventional Grade 60 A706 has higher T/Y or more strain hardening. It is because higher-grade steel in SBH100 has more slip of longitudinal reinforcement out of anchorage, providing more slip deformation to achieve the same drift as SBH60.
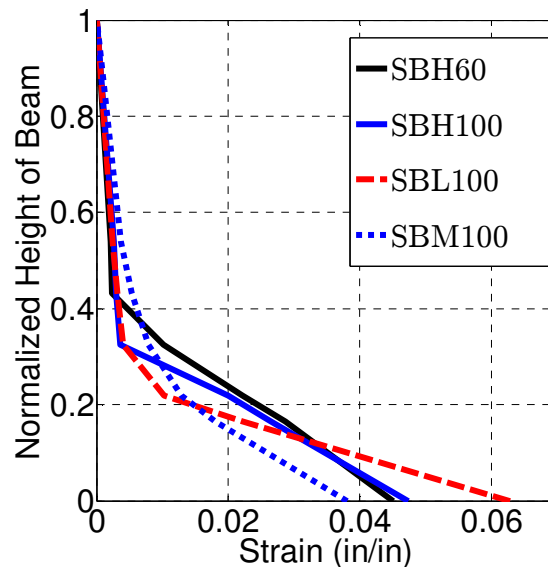
Figure 3.6.1: Strain Profiles along Length of Test Beams at Drift Ratio 4.85%.

3.7. DEVELOPMENT OF STRAIN AT BASE

The progression of peak longitudinal reinforcement strain with increasing lateral drift ratio is plotted in Figure 3.7.1. Grade 60 A706, Grade 100 T/Y = 1.18, and Grade 100 T/Y = 1.30 all exhibit a jump in strain after yielding, apparently because they all have distinct yield plateau in their stress-strain relation. In contrast, Grade 100 A1035 reinforcement with a roundhouse stress-strain relation experiences a more gradual increase in strain as drift ratio increases.
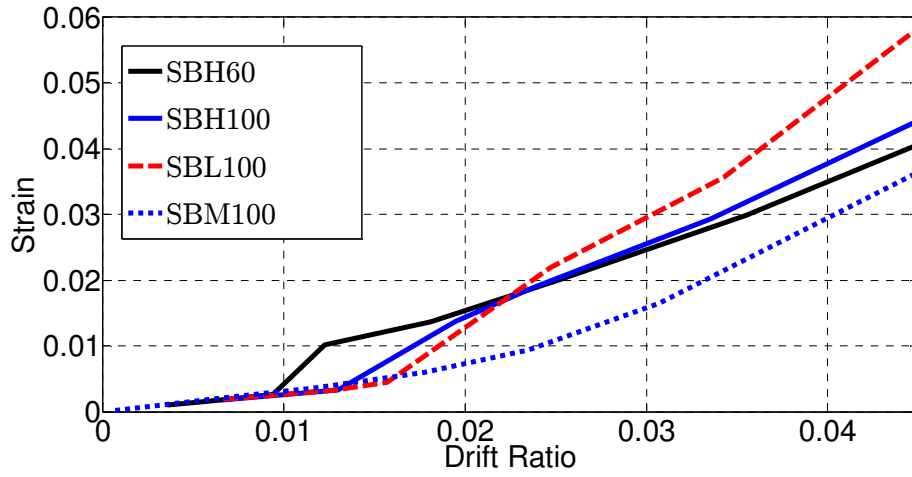
Figure 3.7.1: Strain Development of Longitudinal Bars at Base

4. COMPARISON WITH ANALYTICAL MODELS

4.1. STIFFNESS

It is important in analysis of moment frame to model appropriately the cracked-section stiffness of beams. According to ACI 318 requirements, effective, cracked stiffness of beam element is within the range of $0.35 - 0.50 E_c I_g$, where I_g = gross section moment of inertia and $E_c = 57,000\sqrt{f_c'(psi)} \, (psi)$ = elastic modulus of concrete. Alternatively, ASCE 41 (2013) recommends using $0.30 E_c I_g$ for $P/A_g f_c' \leq 0.1$, which applies for beams. Figure 4.1.1 compares the stiffnesses suggested by ACI 318 and ASCE 41 against those of test beams shown by their envelopes of load-deflection relations.

Lateral stiffness suggested by ASCE 41 agrees very well with effective stiffness of beam SBH60 with conventional Grade 60 A706 steel. As expected, all other beams with higher-grade reinforcement and reduced amount of steel are less stiff than the stiffness recommended by both ACI 318 and ASCE 41.
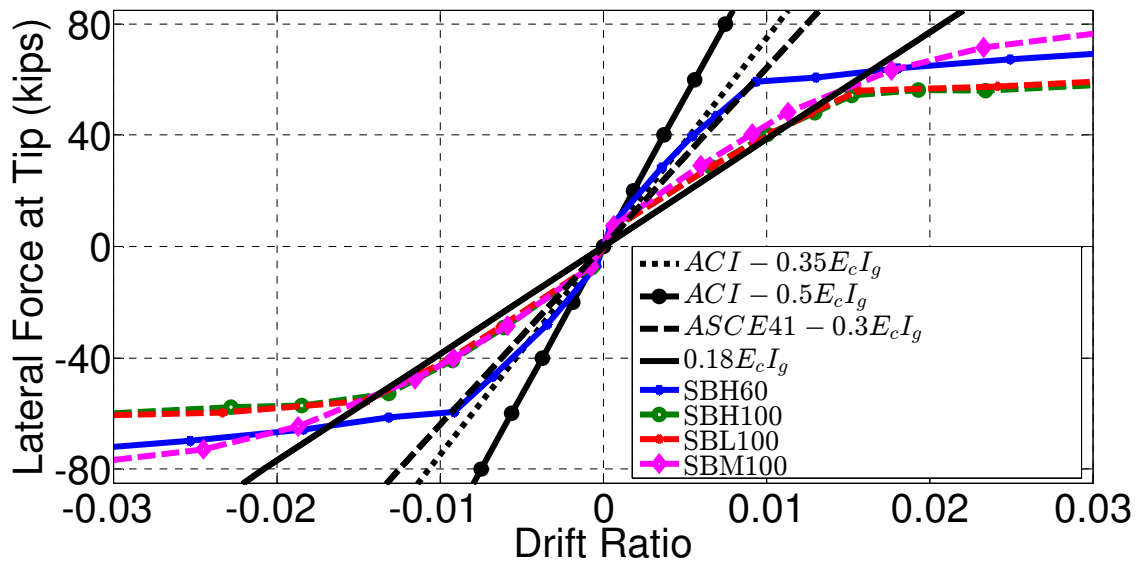
Figure 4.1.1: Lateral Stiffness Comparison

4.2. STRENGTH IN MOMENT AND SHEAR

Moment strength: Probable flexural strength M_{pr} for all test specimens is calculated in accordance with ACI 318-14 and compared to test data (Figure 4.2.1 to Figure 4.2.4). By ACI 318, M_{pr} is computed by using nominal (specified) concrete compressive strength $f_c' = 5000\ psi$ and elasto-plastic stress-strain relation for steel with yield stress equal to 1.25 times specified yield stress. By design, all four test specimens are expected to have equivalent nominal strength. Therefore, M_{pr} calculated by ACI 318 is the same for all test beams.

As shown in Figure 4.2.1 through Figure 4.2.4, the probable moment strength by ACI 318 underestimates the ultimate flexural strength of beams SBH60 and SBM100. This is due to high strain-hardening property of Grade 60 A706 and Grade 100 A1035 reinforcement. ACI 318 M_{pr}, however, slightly overestimates moment strength of beams SBH100 and SBL100.
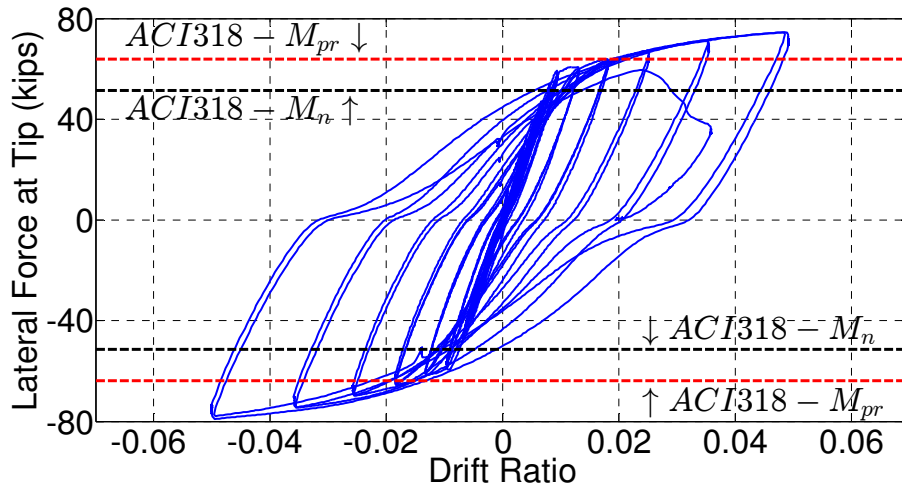
Figure 4.2.1: Lateral Force – Drift Ratio Relation of Beam SBH60
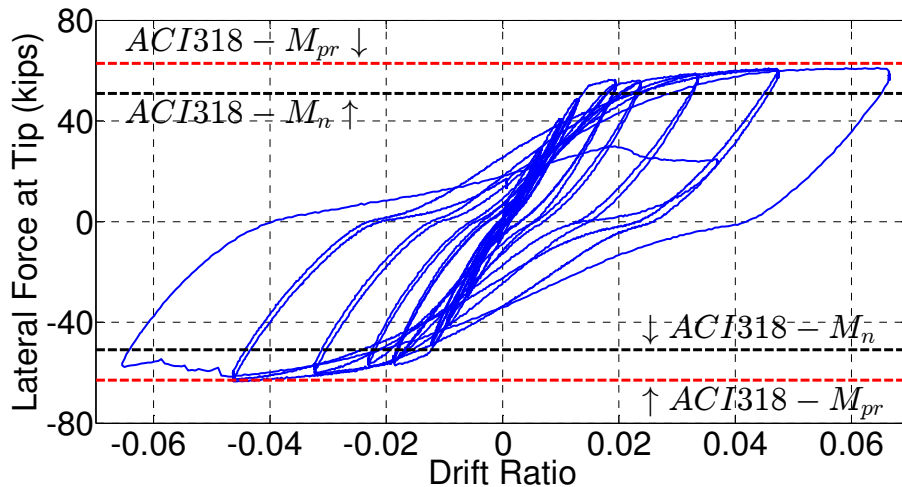
Figure 4.2.2: Lateral Force – Drift Ratio Relation of Beam SBH100
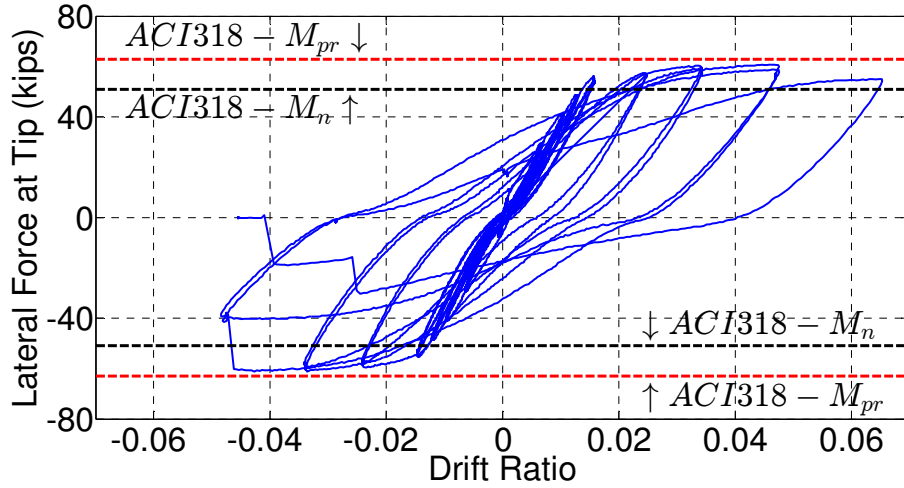
Figure 4.2.3: Lateral Force – Drift Ratio Relation of Beam SBL100
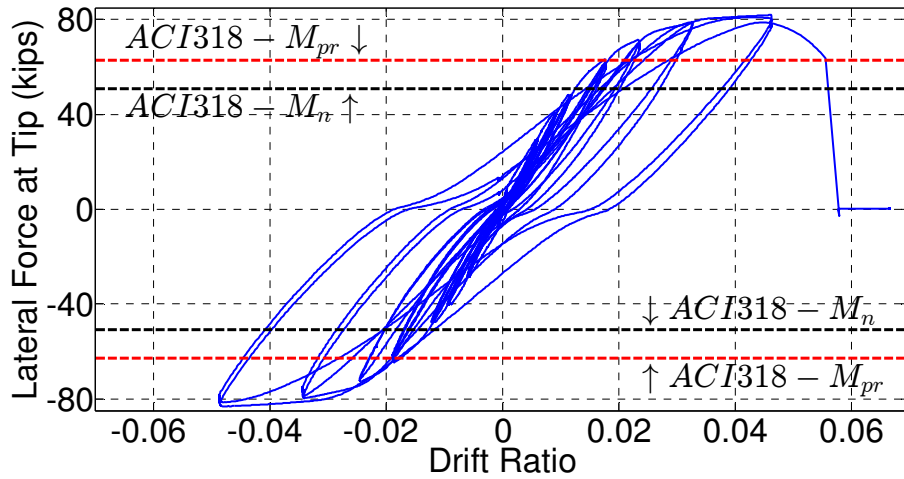
Figure 4.2.4: Lateral Force – Drift Ratio Relation of Beam SBM100

Shear strength: According to ACI 318, nominal shear strength is computed as follows:

$$V_n = V_c + V_s \qquad \text{Eq. (2)}$$

$$V_c = 2\sqrt{f_c'}\,b_w d \qquad \text{Eq. (3)}$$

$$V_s = \frac{A_v f_{yt} d}{s} \qquad \text{Eq. (4)}$$

To accommodate shear strength decay that can occur within plastic hinge regions, ACI 318 specifies $V_c = 0$ within twice the member depth of intended critical sections. Table 4.2.1 summarizes calculated shear strength of the test specimens. As designed, all the test beams have low shear demand of about $3\sqrt{f_c'}$ to minimize the tension shift effect. As measured, shear stress

demand on all specimens is below $4\sqrt{f_c'}$ or 40% of shear capacity provided by transverse reinforcement only.

Table 4.2.1: Shear Strength of Test Specimens

	SBH60	SBH100	SBL100	SBM100
V_c $(kips)$	41	41	41	41
V_s $(kips)$	206	258	258	258
$V_{measured}$ $(kips)$	75	61	61	82
$V_{measured}/(b_w d\sqrt{f_c'})$	3.7	3.0	3.0	4.0
$V_{measured}/V_s$	0.36	0.24	0.24	0.32
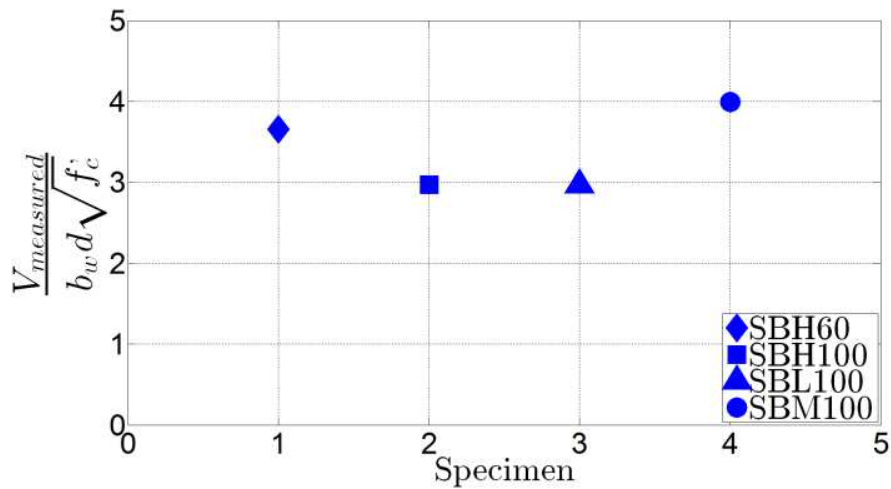
Figure 4.2.5: Normalized Shear Demand
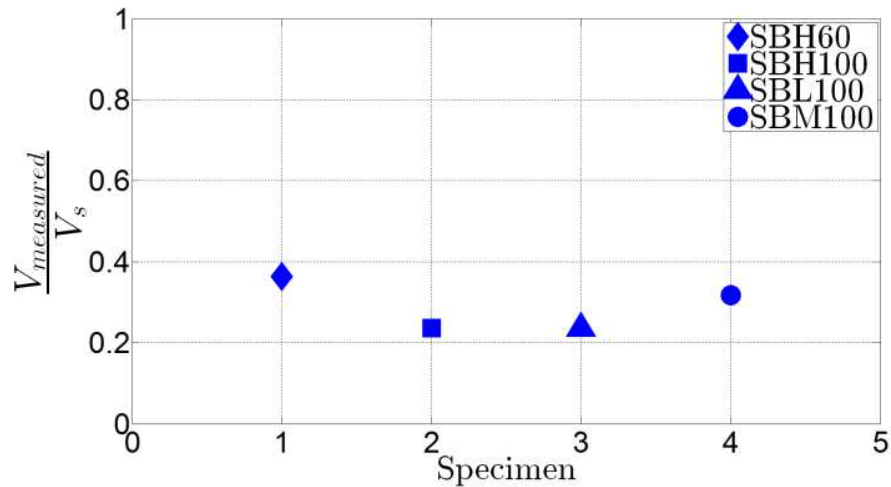
Figure 4.2.6: Shear Demand Normalized by Transverse Reinforcement Capacity

42

4.3. DEFORMATION CAPACITY PER ASCE 41

The monotonic load-deformation relation is calculated in accordance with ASCE 41-13 and compared against those response envelopes of beam test data in Figure 4.3.1 to Figure 4.3.4. Deformation at B is computed by taking nominal flexural strength of the cross section divided by effective stiffness $0.30E_cI_g$ suggested by ASCE 41. Nominal flexural strength is taken as strength when concrete strain reaches 0.003 and estimated by using expected concrete compressive strength f_c' of approximately 5000 psi for all test specimens, and expected yield stresses (f_y) of 69 ksi and 100 ksi for Grade 60 A706 and Grade 100 reinforcement, respectively. Plastic rotation recommended by ASCE 41, which is 0.025 radians for all test beams, is added to deformation at B to obtain ultimate deformation at C. Strength at C is defined as strength when concrete strain reaches 0.003 and ultimate steel stresses (f_u) are $1.25 \times 69 = 86\ ksi$ and $1.25 \times 100 = 125\ ksi$ for Grade 60 A706 and Grade 100 reinforcement, respectively.

The ASCE 41-13 load-deformation relations agree well with test data for beam SBH60 with conventional Grade 60 reinforcement even though the ultimate rotation is slightly underestimated. The correlation is less agreeable for the beams with Grade 100 steel. The larger effective stiffness suggested by ASCE 41-13 as discussed in the previous section results in much lower deformation at B. Secondly, M_{pr} computed according to ACI 318-14 using overstrength factor of 1.25 to account for reinforcement strain-hardening provides overestimation of ultimate strength for beams SBH100 and SBL100 with higher-grade reinforcement having T/Y = 1.30 and 1.18, respectively. On the other hand, this M_{pr} underestimates ultimate strength of specimen SBM100 as discussed in previous section. Disagreement in effective stiffness and ultimate strength results in poor correlation of load-deformation between model and test data for beams with higher-grade reinforcement.
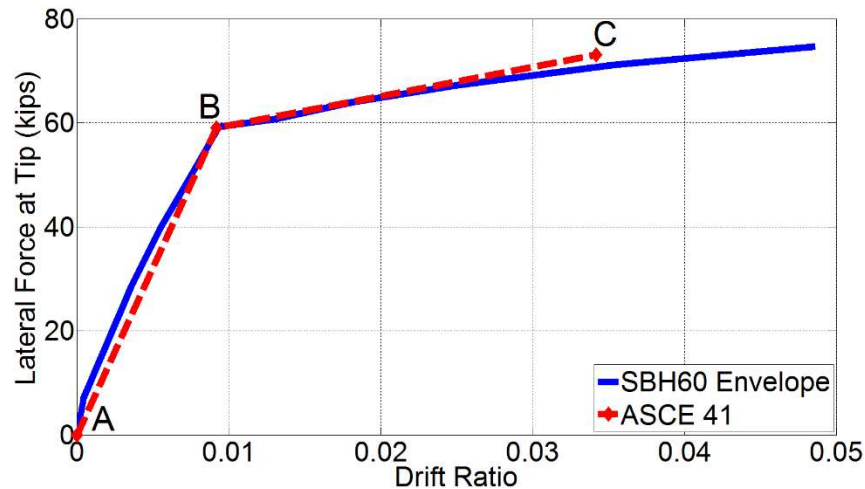
Figure 4.3.1: Monotonic Load-Deformation Comparison for Specimen SBH60
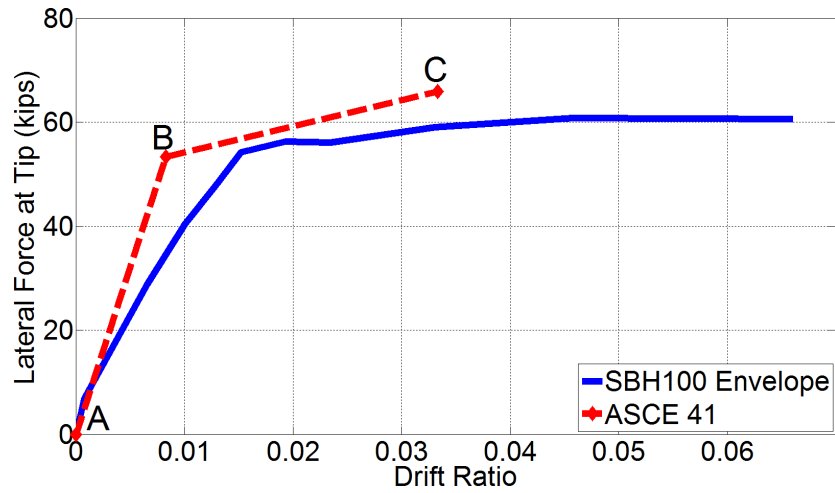
Figure 4.3.2: Monotonic Load-Deformation Comparison for Specimen SBH100
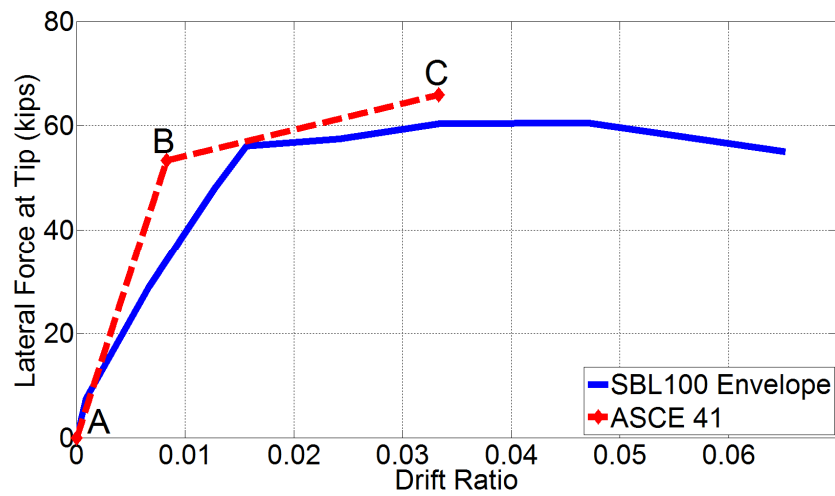
Figure 4.3.3: Monotonic Load-Deformation Comparison for Specimen SBL100
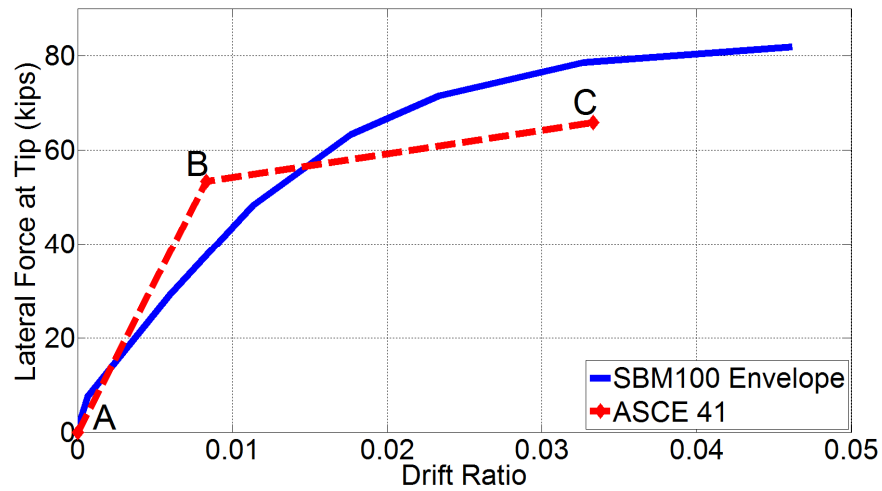
Figure 4.3.4: Monotonic Load-Deformation Comparison for Specimen SBM100

4.4. EFFECTIVE PLASTIC HINGE LENGTH

The plastic-hinge model utilizes the idealized elasto-plastic moment-curvature relation with a plastic hinge length to estimate displacement capacity. The member is assumed to develop linear-elastic curvature along its length. The inelastic curvature of magnitude $(\emptyset_u - \emptyset_y)$ is assumed to extend over plastic hinge length l_p (Figure 4.4.1). According to the model, plastic rotation is

$$\theta_p = (\phi_u - \phi_y)l_p \quad \text{Eq. (5)}$$

And the displacement at the tip of a flexural member resisting a concentrated load at its tip is

$$\delta_u = \frac{\phi_y l^2}{3} + (\emptyset_u - \emptyset_y)l_p\left(l - \frac{l_p}{2}\right) \quad \text{Eq. (6)}$$
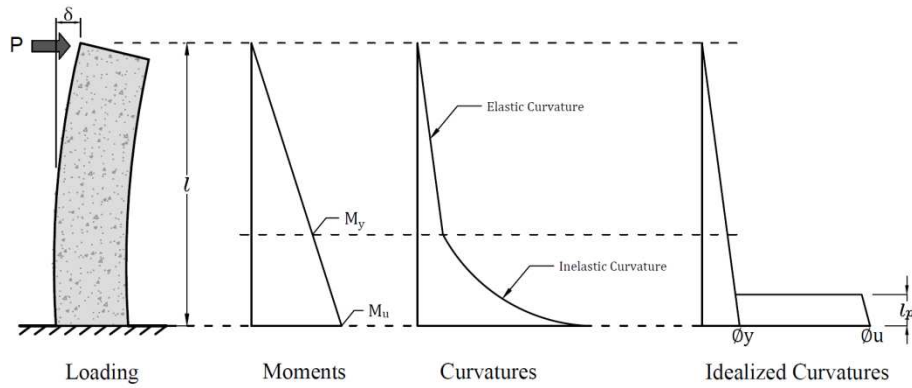
Figure 4.4.1: Conventional Plastic Hinge Model

In the plastic-hinge model, the plastic hinge length has been determined empirically. The tip displacement δ_u, and curvatures ϕ_u and ϕ_y are measured from laboratory experiment. The plastic hinge length l_p is then computed to satisfy Eq. (6). As a result, deformations contributed from shear and slip are accounted for implicitly in the plastic hinge length.

Several researchers have proposed expressions for computing plastic-hinge length. Priestley and Park (1987) recommended

$$l_p = 0.08l + 0.00015d_b f_y, psi$$

Berry et al. (2008) suggested

$$l_p = 0.05l + 0.008d_b f_y/\sqrt{f_c'}, psi$$

In practice, a simpler expression that provides reasonable accuracy is

$$l_p = 0.5h$$

These expressions for calculating plastic-hinge length had been developed from laboratory tests of column specimens reinforced with conventional Grade 60 steel. Consequently, the expressions do not consider the effect of tensile-to-yield strength ratio (T/Y), which has been shown to significantly affect the spread of plasticity from the test results of this research program.

Applying plastic hinge model with measured test data on tip deflection and curvatures at yield and ultimate, the plastic-hinge length is back-calculated for loading cycles with target drift ratio of 3% for all beam tests and presented in Table 4.4.1 and Figure 4.4.2 and Figure 4.4.3. Measured strain used to calculate curvatures are taken from strain gauge reading on longitudinal reinforcement at base of beam during tests. In Table 4.4.1, yield curvature is also computed by moment-curvature analysis for beam cross-section under monotonic loading, and strain at yielding is taken as corresponding nominal yield stresses (60 ksi and 100 ksi) divided by Young's modulus of elasticity (E = 29000 ksi). Curvatures at yield measured during tests agree well with that from moment-curvature analysis, providing confidence on performance of strain gauges and accuracy of strain data.

Under the same drift demand, SBL100 with higher-grade reinforcement provides more slip deformation, and its flexural deformation is more localized close to its base than those in SBH60 with conventional Grade 60 A706 steel. As a result, similar plastic hinge length can be expected for beams SBL100 and SBH100. Plastic hinge lengths of both specimens SBH100 and SBM100 are approximately 1.5 times the beam cross-sectional height, which are longer than that of SBH60. Plastic hinge lengths of all test beams are longer than half of beam cross-sectional height that is widely used in practice as explained in preceding paragraphs.

Table 4.4.1: Plastic Hinge Length at 3% Drift Ratio

	SBH60	SBH100	SBL100	SBM100
Computed Yield Curvature ($1/in$)	0.00014	0.00022	0.00022	0.00022
Measured Yield Curvature ($1/in$)	0.00015	0.00021	0.00022	0.00026
Measured Curvature at 3% Drift Ratio ($1/in$)	0.0014	0..00097	0.0014	0.00097
Plastic Hinge Length l_p (in)	30	48	27	46
l_p/h	1.25	2.00	1.13	1.92
l_p/l	0.32	0.51	0.29	0.49
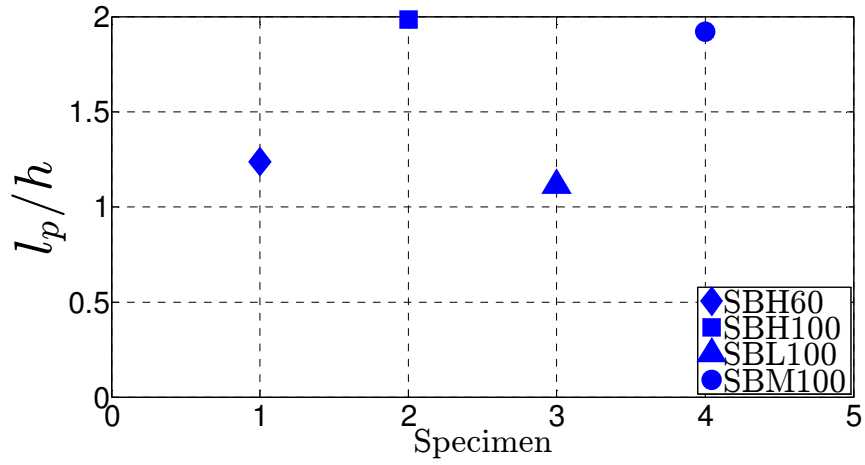
Figure 4.4.2: Plastic Hinge Length Normalized by Beam Cross-Sectional Height
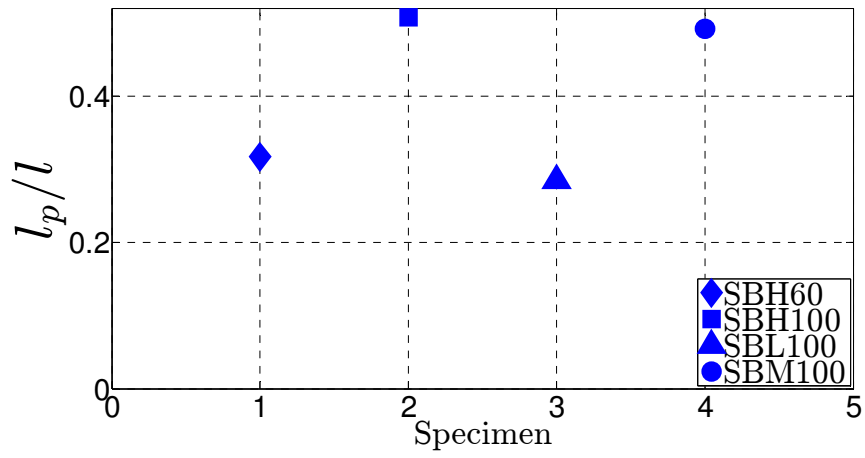
Figure 4.4.3: Plastic Hinge Length Normalized by Beam Length

5. NUMERICAL MODELING OF REINFORCED CONCRETE BEAMS AND COLUMNS

5.1. BEAMS

The load-deflection response of test beams can be calculated using conventional mechanics approaches. The total displacement is the sum of three components (Figure 5.1.1):

$$\delta = \delta_f + \delta_v + \delta_s \qquad \text{Eq. (7)}$$

where δ_f = displacement due to flexural curvature
δ_v = displacement due to conventional shear distortion
δ_s = rigid-body displacement due to reinforcement slip from anchorage zone
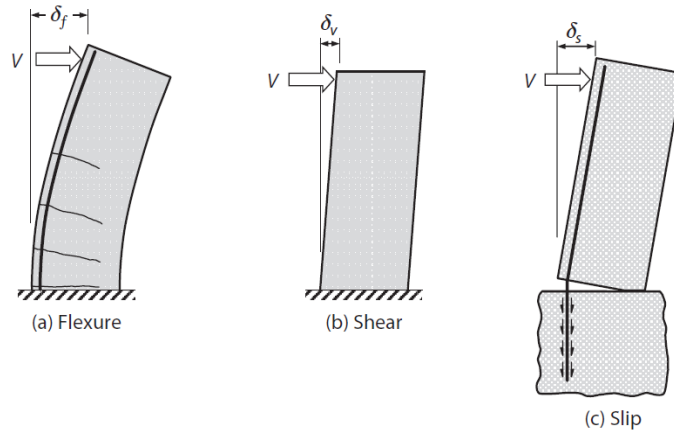
Figure 5.1.1: Components of Displacement in Beam (used with permission from Moehle, 2014)
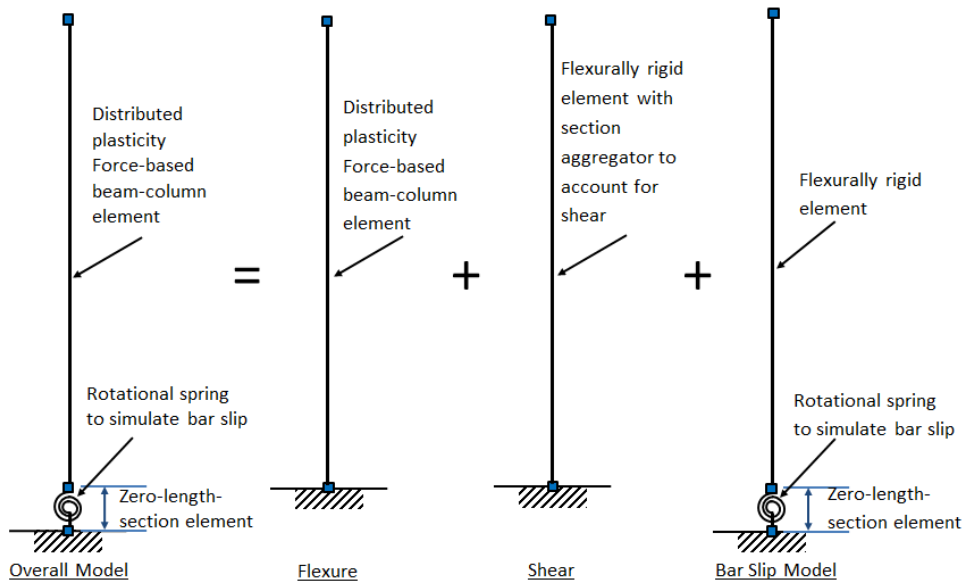
Figure 5.1.2: Overall OpenSees Model of Test Beams

Each of displacement components can be modeled separately with sufficient accuracy within the linear range of response. Nonlinear inelastic range response, however, poses challenges because of interaction between flexure and shear. To simplify the calculations, a common practice is to model shear with a linear elastic spring that is implicitly accounted for within flexural element through section aggregator.

The test beams were modeled in the computer software package OpenSees (McKenna et al. 2000) and analyzed for cyclic response by displacement control with input displacement values taken from measured test data.

The overall model has a distributed plasticity force-based beam-column element and zero-length section element to simulate the response of flexure and bar slip, respectively (Figure 5.1.2). Both elements have a fiber cross section with concrete and steel fibers having properties as described in the next section on materials. Shear behavior is modeled by imposing its properties onto flexural element through section aggregator.

a. Materials

Concrete

A simple model of stress-strain relationship is adopted here for cover (unconfined) concrete with peak strength f_c' taken from the cylinder test of 5 ksi (Figure 5.1.3). A linearly descending branch is assumed after reaching f_c' until complete loss of strength at strain of 0.006. Core (or confined) concrete properties were modeled by the algebraic form proposed by Mander et al. (1988a). The resulting confined concrete properties and stress-strain relation of the test beams are shown in Figure 5.1.4.
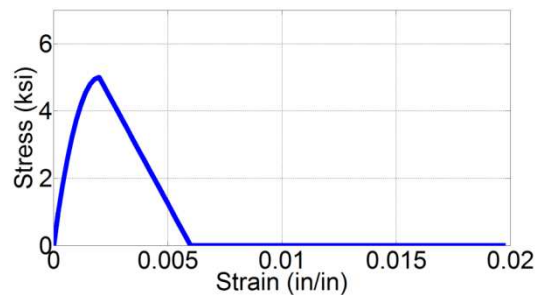
Figure 5.1.3: Cover (Unconfined) Concrete Stress-Strain Relation
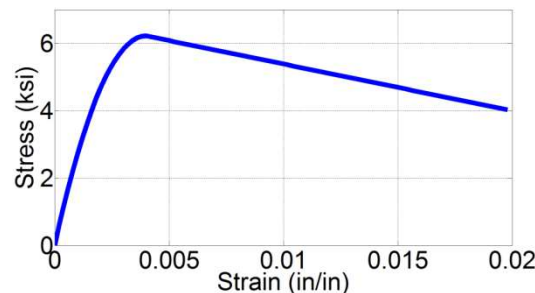
Figure 5.1.4: Core (Confined) Concrete Stress-Strain Relation

Steel

Uniaxial material ReinforcingSteel (Kunnath et al. 2009) based on Chang and Mander (1994) hysteretic behavior is used to model cyclic properties of reinforcement used in test beams SBH60, SBH100, and SBL100. Table 5.1.1 lists all the parameters used in ReinforcingSteel material to model the reinforcement properties in specimens SBH60, SBH100, and SBL100.

Grade 100 A1035 steel has distinctly different properties than the other three by the round-shaped stress-strain relationship without yield plateau. A new mathematical model has been developed in OpenSees platform for this research program to simulate the behavior of Grade 100 A1035. This new uniaxial material model has the behavior under loading in tension described by the Ramberg-Osgood equation (Ramberg and Osgood 1943). When the loading is reversed in direction to compression after the material has yielded in tension under large strain, the material responds following the Bauschinger effect. For response in large strain region (greater than 0.02), this material behaves according to Bauschinger effect in both tension and compression loading conditions (Figure 5.1.8).

All the parameters shown in Table 5.1.1 were selected to obtain the best correlation with the stress-strain relations of steel bars used in test beams. Steel specimens were taken from the same batch used to construct test beams and tested in the laboratory under cyclic loading. Grip spacing was five times bar diameter, which was also the transverse reinforcement spacing in the test beams. The strain histories measured during beam tests were imposed onto steel specimens under displacement control. Stress-strain relationship of the steel models and actual steel bar tests are shown in Figure 5.1.5 through Figure 5.1.8.

Table 5.1.1: Steel Material Model Parameters

| Steel Model | Parameters | Description | Steel used in | | | |
			SBH60	SBH100	SBL100	SBM100
Reinforcing Steel	f_y	Yield stress (ksi)	64.5	101.5	105	
	f_u	Ultimate stress (ksi)	95.5	127.5	124	
	E_s	Young's modulus (ksi)	29000	29000	29000	
	E_{sh}	Tangent stiffness at initiation of strain hardening	950	950	750	
	ε_{sh}	Strain at initiation of strain hardening	0.0055	0.007	0.007	
	ε_{su}	Strain at ultimate stress	0.15	0.08	0.08	
	l_{SR}, β, r, γ	Parameters for buckling model based on Gomes and Appleton (1997)	5, 1.0, 0.75, 0.0	5, 1.0, 0.85, 0.0	5, 1.0, 0.75, 0.0	
	a1, limit	Parameters for controlling isotropic hardening	4.3, 0.01	4.3, 0.01	4.3, 0.01	
	R1, R2, R3	Parameters for controlling transition from elastic to plastic branches	0.333, 20, 6	0.333, 25, 4	0.5, 40, 1	

	f_y	Yield stress (ksi)				160
	E_s	Young's modulus (ksi)				29,000
	β_{steel}	Strain hardening ratio				0.001
New Steel Model	Ro, cR1, cR2	Parameters for controlling transition from elastic to plastic branches				25, 0.925, 0.15
	a1, a2, a3, a4	Parameters for controlling isotropic hardening				0.0, 1.0, 0.0, 1.0
	a	Yield offset in Ramberg Osgood's model				0.015
	n	Parameter for controlling transition from elastic to plastic branches in Ramberg Osgood's model				10
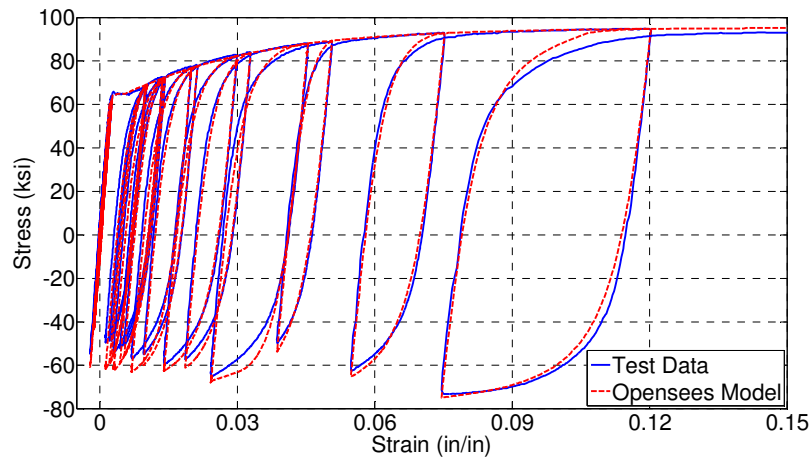
Figure 5.1.5: Stress-Strain Relationship for No. 9 Grade 60 A706 Steel Model
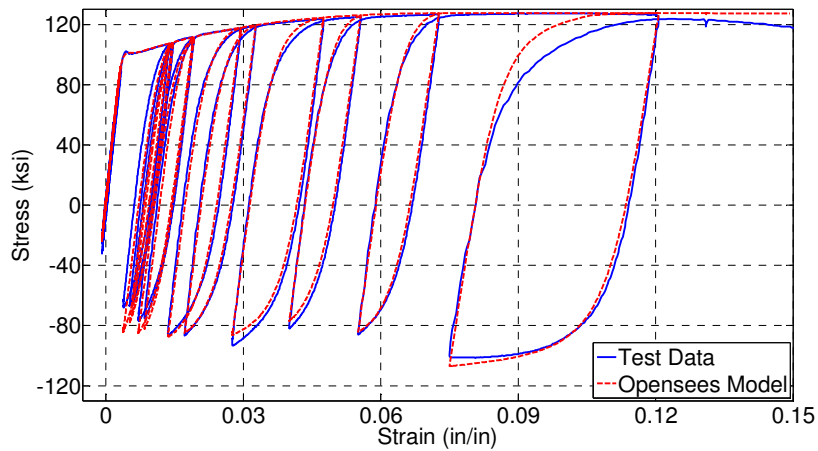
Figure 5.1.6: Stress-Strain Relationship for No. 8 Grade 100 T/Y = 1.30 Steel Model
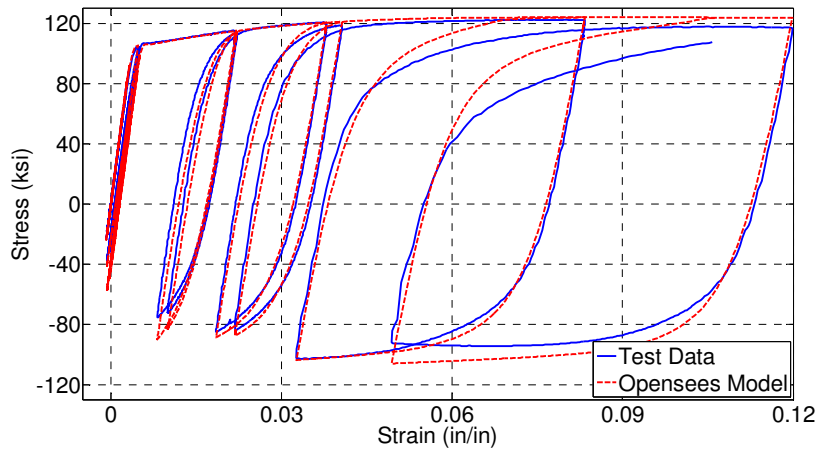
Figure 5.1.7: Stress-Strain Relationship for No. 8 Grade 100 T/Y = 1.18 Steel Model
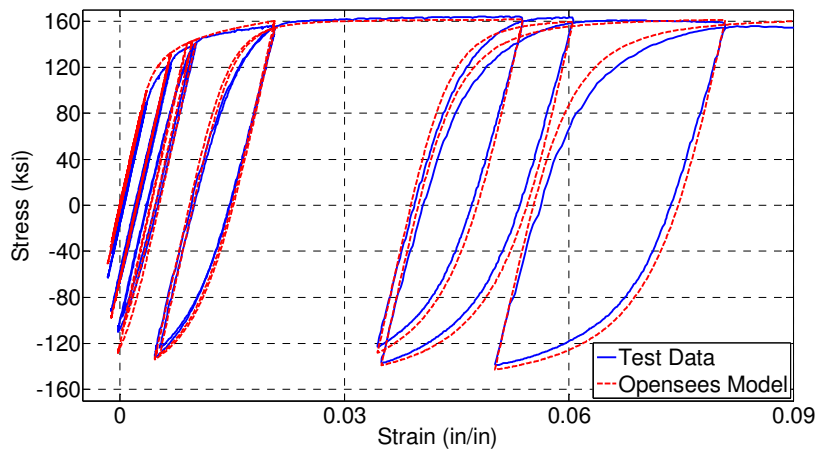
Figure 5.1.8: Stress-Strain Relationship for Grade 100 A1035 Steel Model

In the following sections, test data of beam SBH100 is used to calibrate numerical models. Subsequently, numerical models are extended to model all other beams tested in this research program, as well as all column tests in the companion program conducted at the University of Texas, Austin.

b. Flexural Element – Force-Based Beam-Column Element

Flexural response of the test beams can be modeled by using the distributed plasticity force-based beam-column element in OpenSees. The force-based beam-column element is formulated based on interpolation of force so that equilibrium between element and section forces is satisfied exactly, which holds in the range of constitutive nonlinearity. Section forces are determined from the element forces by interpolation within the element that comes from static equilibrium with constant axial force and linear distribution of bending moment in absence of distributed element loads.

Gauss-Lobatto quadrature is used in force-based elements because it places integration points at the element ends, where bending moments and associating curvatures are largest in absence of element load. To represent accurately the nonlinear material response of a force-based beam-column element, four to six Gauss-Lobatto integration points are typically used (Neuenhofer and Filippou, 1997).

Flexural response of the test beams is modelled by using distributed plasticity force-based beam-column element with four Gauss-Lobatto integration points including two points at ends of beam to account for locations of largest moment and curvature (Figure 5.1.9).
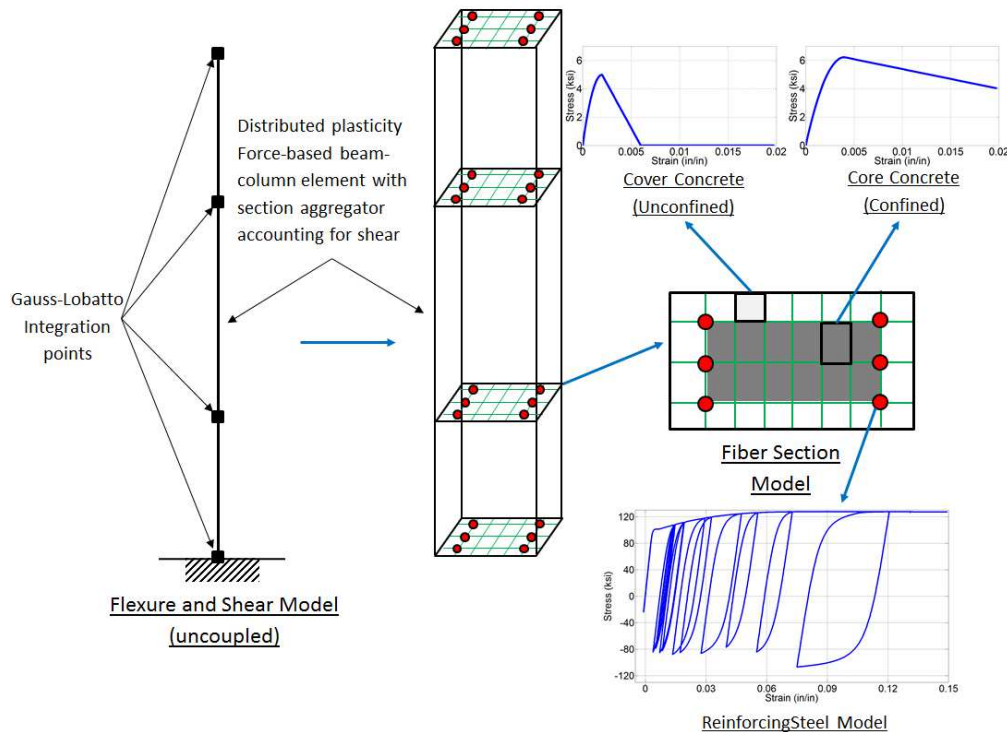
Figure 5.1.9: Force-Based Beam-Column Element with Fiber Section to Model Flexural Response of Test Beam

Applying displacement values at tip of the beam obtained from test data and lateral force required to achieve specified displacement was computed through iterative procedure. The lateral load vs. tip displacement for both analytical model and test data of specimen SBH100 is plotted in Figure 5.1.10.
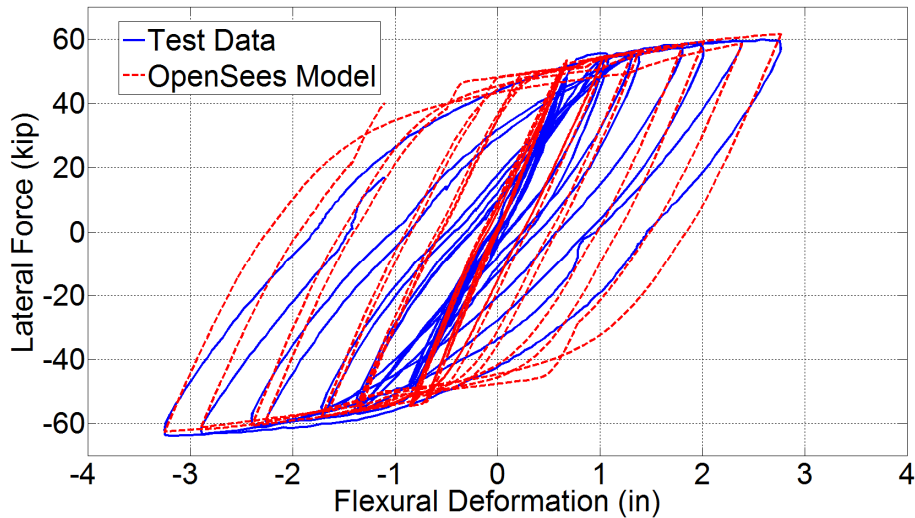
Figure 5.1.10: Flexural Hysteretic Response

c. Shear Element – Section Aggregator

It is common in practice that linear elastic shear behavior is incorporated in flexural element through section aggregator to model overall response of reinforced concrete beams. In this case, flexure and shear are uncoupled within the element. A simple force-based beam-column element is again used with very large flexural stiffness to model shear behavior only for the test beams (Figure 5.1.11). Two types of shear properties are presented in this figure including linear elastic typically used in design office and Modified Ibarra-Medina-Krawinkler Deterioration Model with Pinched Hysteretic Response (MIMK) (Ibarra et al. 2005). Figure 5.1.12 presents the shear behavior of the two models using these two types of shear properties (specimen SBH100).

Incorporating these two shear responses into flexural element developed in preceding section, the overall responses of the beam model for two cases of shear properties are computed and shown in Figure 5.1.13. Apparently, using MIMK gives better overall hysteretic response as it results in more accurate post-yield strength and unloading behavior compared to elastic shear model. They both do not yield accurate initial lateral stiffness of the beam.
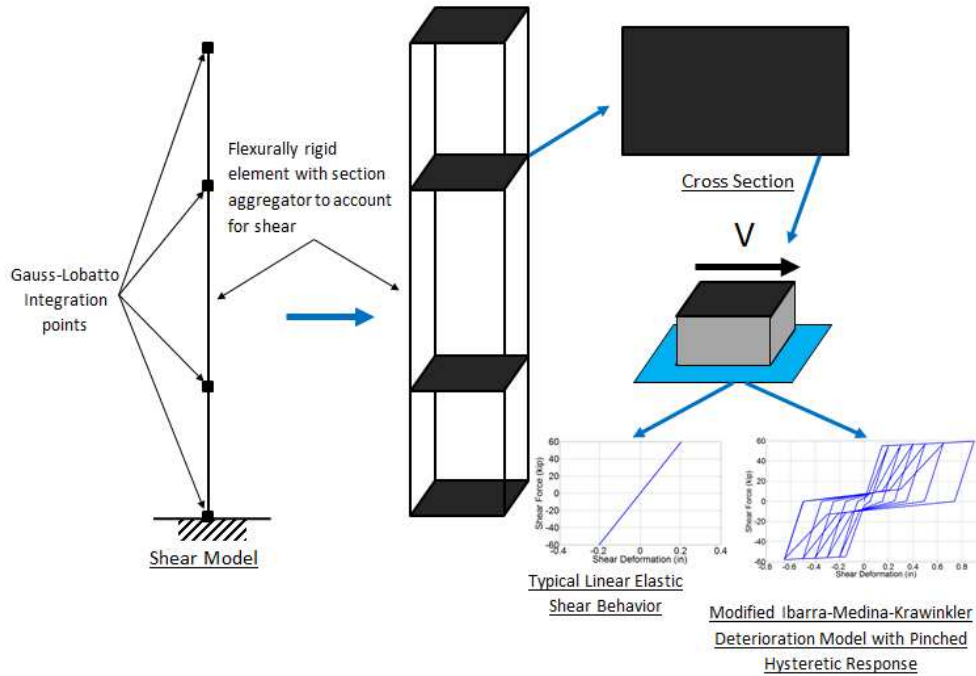
Figure 5.1.11: Shear Model
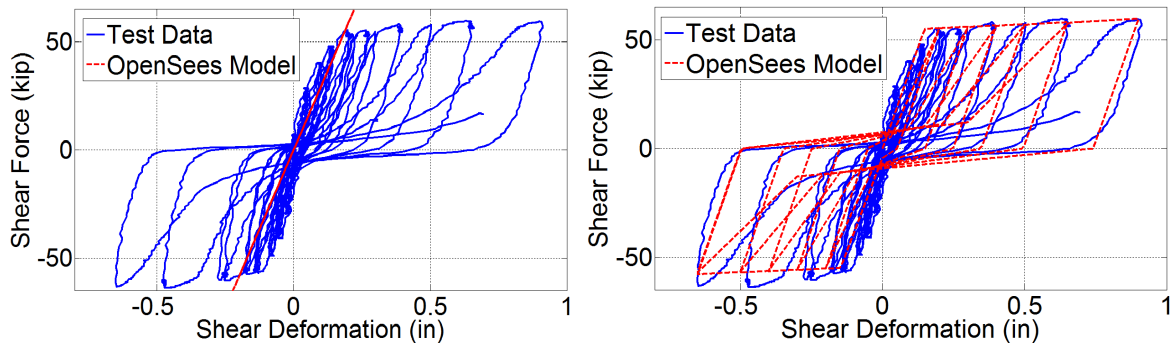
Figure 5.1.12: Shear Behavior – Left: Linear Elastic – Right: Ibarra-Medina-Krawinkler Model
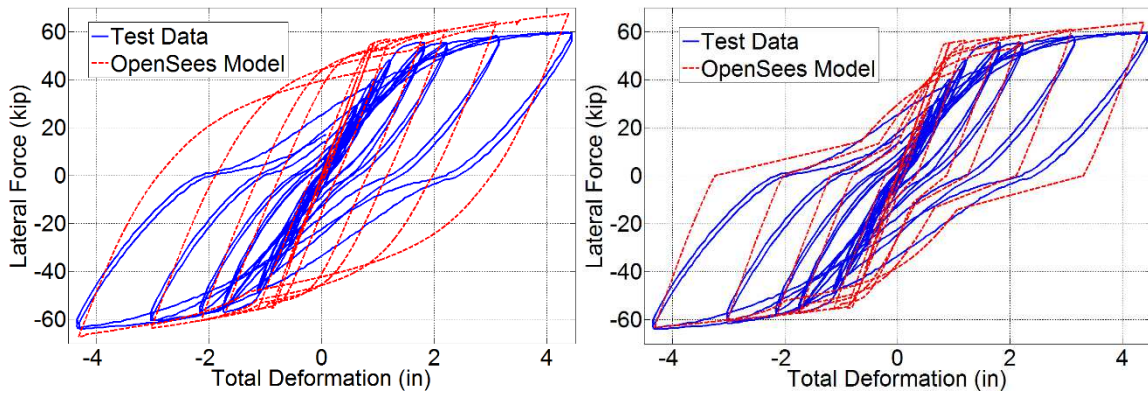
Figure 5.1.13: Overall Response with Flexure and Shear Models Combined – Left: Linear Elastic – Right: Ibarra-Medina-Krawinkler Model

d. Slip Element – Zeo-Length Section Element

To model bar slip from the anchorage block, a linear elastic rotational spring is often used in practice and implemented at the base of beam element through the zero-length section element. An improved model to estimate hysteretic response of bar slip involves constructing fiber section and assigning its properties to the zero-length section element (Figure 5.1.17). The fiber section has cover and core concrete properties similar to those described in fiber section of flexural element. The hysteretic model by Zhao and Sritharan (2007) is adopted to describe the cyclic response of steel fiber in the fiber section (Figure 5.1.14 and Figure 5.1.15). In this model, stress and slip at yielding and ultimate were taken from test data. A zero-length section element, which actually has unit length implicitly, is used for section analysis to calculate the moment-rotation response.

Further refinement of the bond-slip model was introduced as it was recognized that the model lacked the ability to adjust the center of fixed-end rotation based on the changing neutral axis depth in the adjacent flexural element. A modification of fiber-section spring that results in the fixed-end rotations caused by bar-slip being centered at the location of neutral axis of the flexural element was proposed by Ghannoum (2007). This can be achieved by using the same fiber discretization of steel and concrete in the zero-length section as in the frame section, and scaling material strain in this bar-slip element by the same factor r_y:

$$r_y = \frac{E_s}{E_{slip}} = \frac{S_y}{\varepsilon_y} \qquad E_{slip} = \frac{f_y}{S_y} \qquad\qquad \text{Eq. (8)}$$

where: E_s = Young's modulus of steel (ksi)
$\quad\quad f_y$ = yield stress of steel (ksi)
$\quad\quad \varepsilon_y$ = strain at yield of steel (in/in)
$\quad\quad S_y$ = amount of slip of steel out of anchorage at yield stress (in)

Based on test data, the behavior of the rotational spring is calibrated to have similar stiffness as the slip response of the test beams for the elastic rotational spring and as well as reasonably close hysteretic response for the fiber section rotational spring. The behavior of the slip from models and test data of specimen SBH100 are presented in Figure 5.1.18.
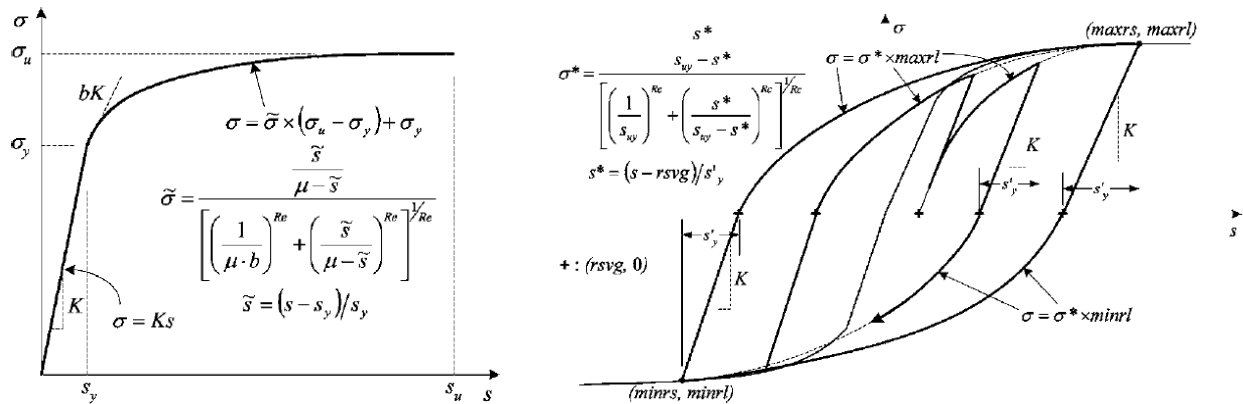
Figure 5.1.14: *BondSP1* Hysteretic Model Proposed by Zhao and Shritharan (2007)
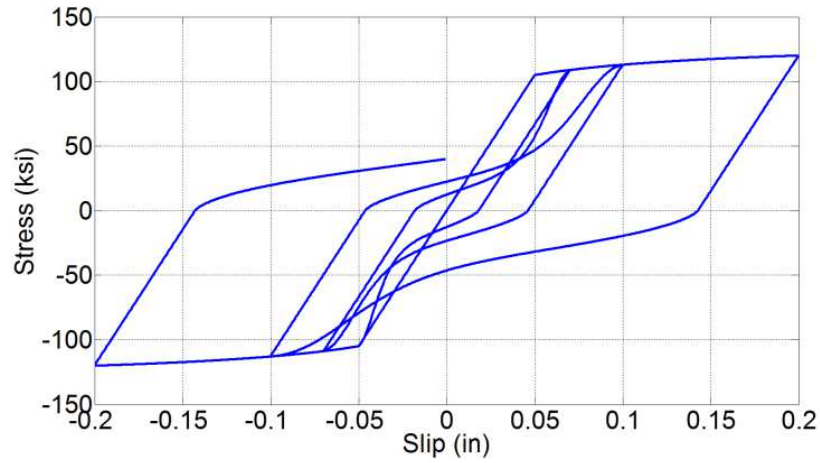
Figure 5.1.15: Cyclic Behavior of Steel in Fiber Section of Zero Length Section Element
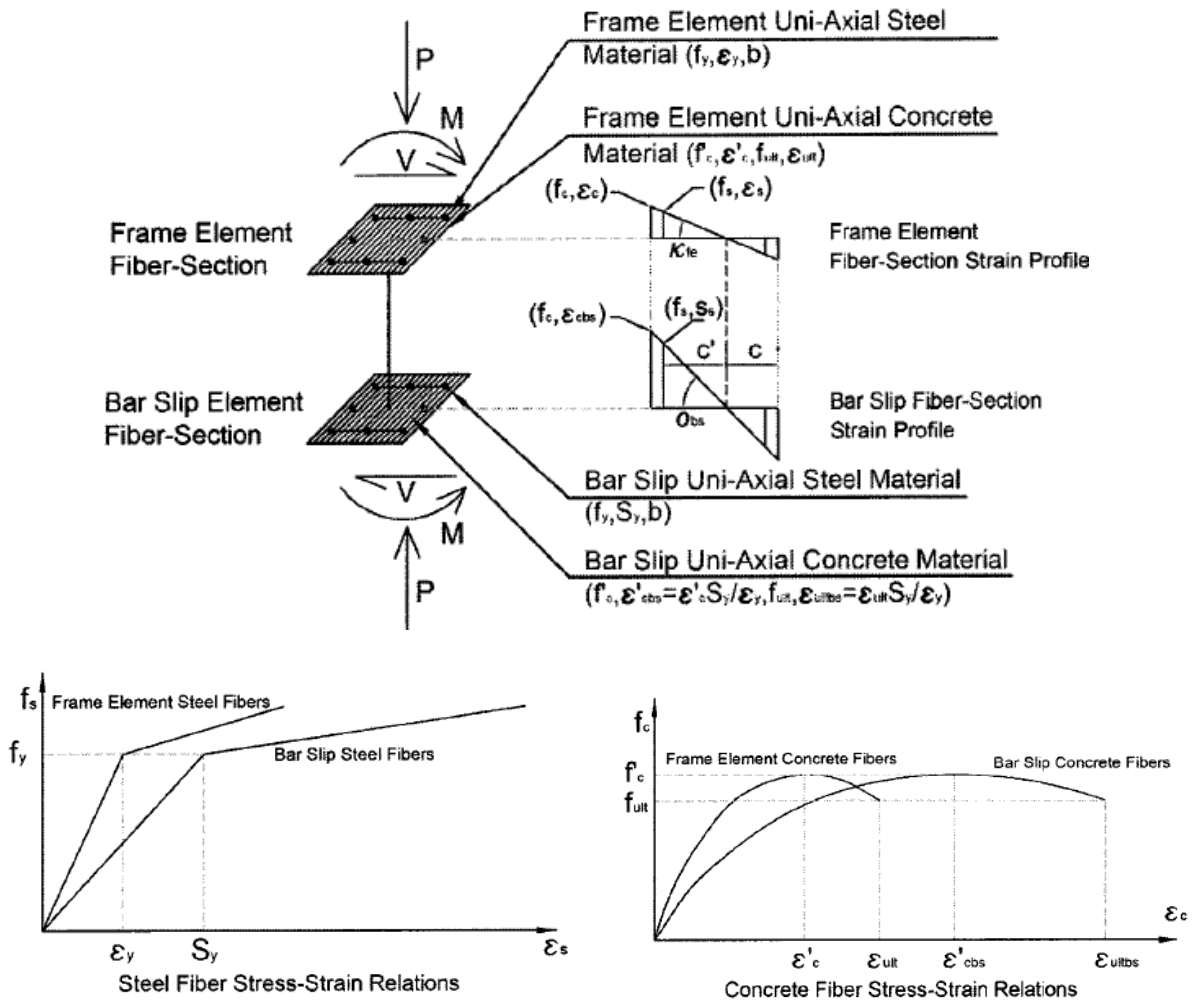
Figure 5.1.16: Bar-Slip Section Equilibrium, Strain Profiles, and Materials (Ghannoum 2007)
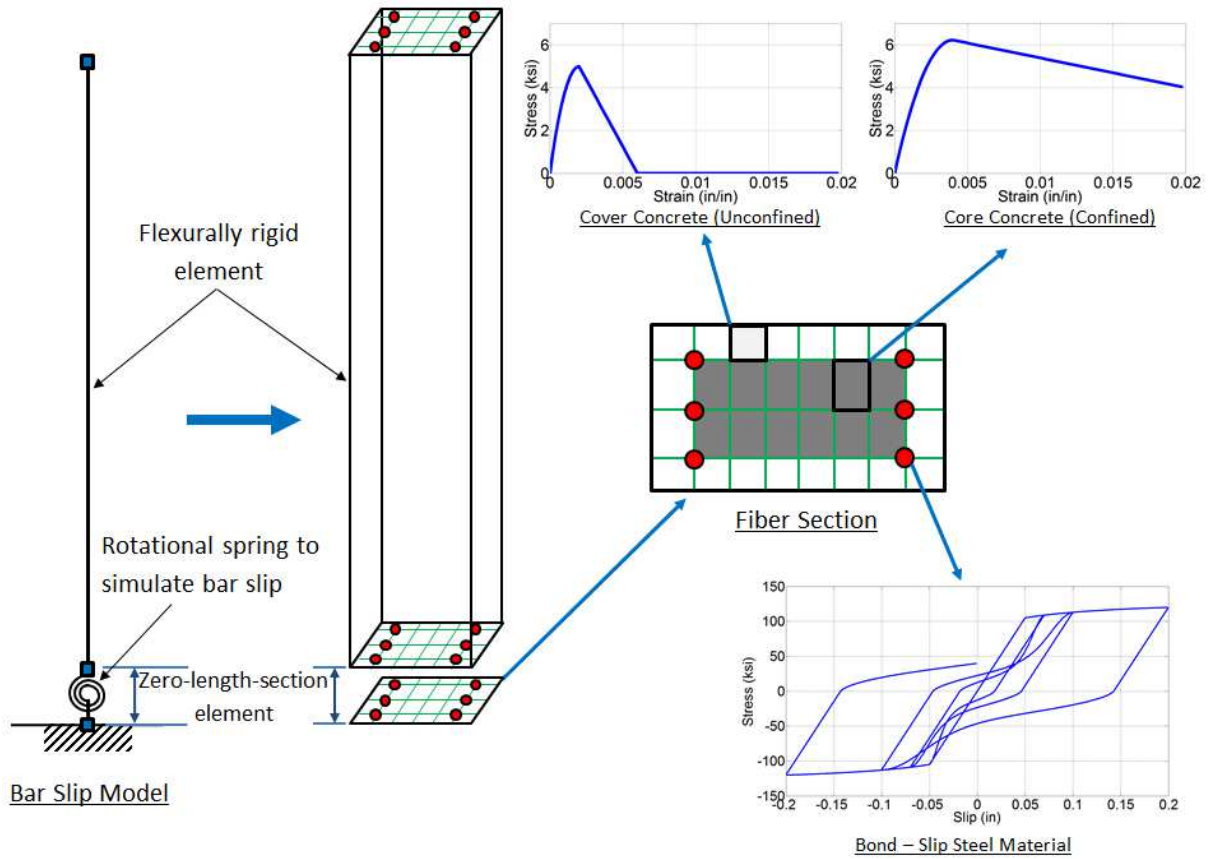
Figure 5.1.17: Bar Slip Model
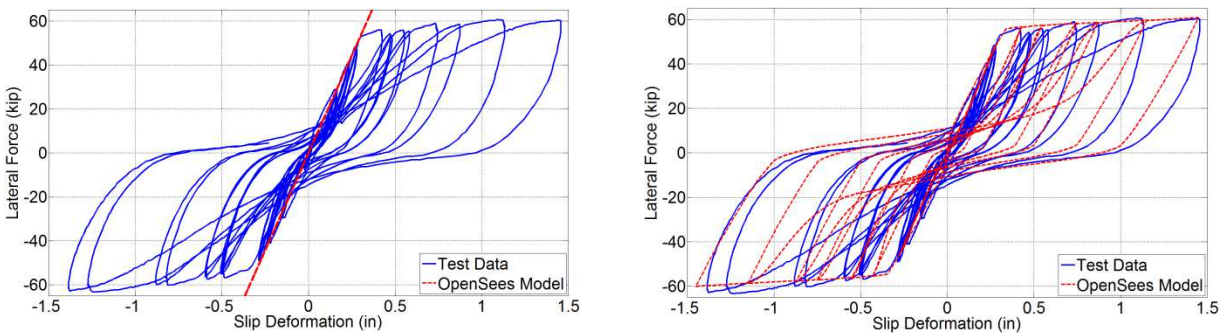
Figure 5.1.18: Slip Behavior – Left: Linear Elastic – Right: Fiber Section

e. Overall Model Response

Three versions of the analytical model were developed and subjected to the displacement history measured during the test of specimen SBH100. The comparison of the calculated and measured load-displacement relations provides information on the importance of including various components in the overall analytical model (Figure 5.1.19).

(a)

(b)

(c)
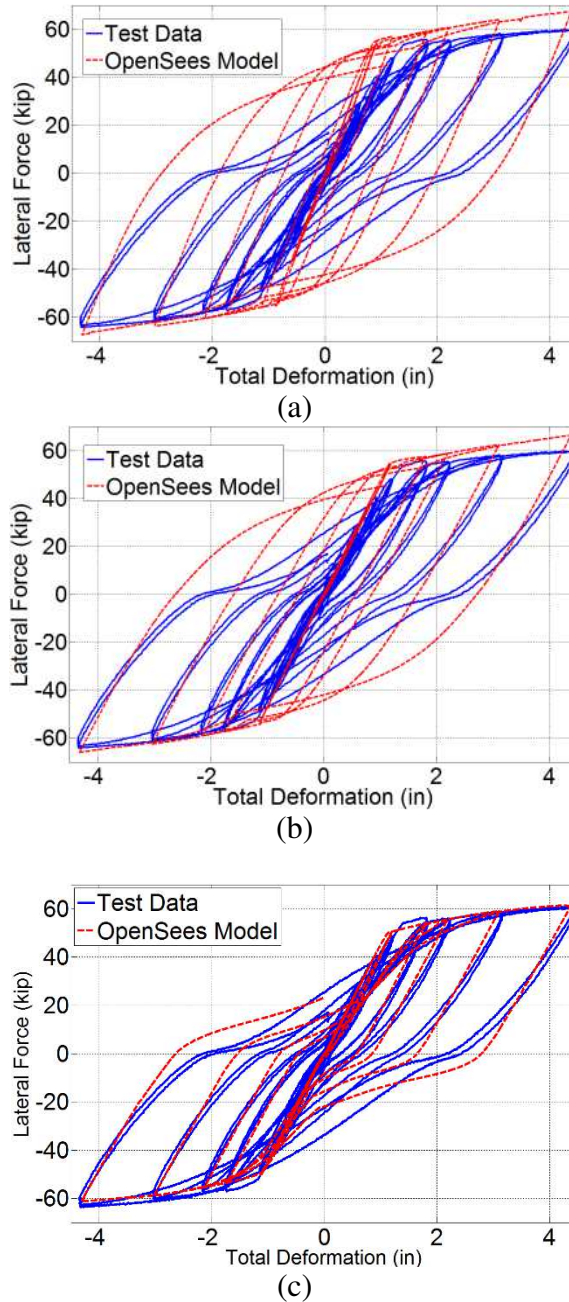
Figure 5.1.19: Overall Response of OpenSees Models. (a): Inelastic Flexure and Elastic Shear; (b): Inelastic Flexure, Elastic Shear and Slip; (c): Inelastic Flexure, Shear by Modified Ibarra-Medina-Krawinkler Model, and Slip by Fiber Section with Bond-Slip Steel Model by Zhao and Sritharan

Figure 5.1.19a presents results for an analytical model that considers inelastic flexure and elastic shear. Although the strength (which is limited by flexural strength) is well modeled, the initial stiffness is overestimated and the shapes of the load-displacement loops are wider than those of the test beam, which indicates excessive energy is being dissipated by the analytical model.

Figure 5.1.19b presents results for an analytical model that considers inelastic flexure, elastic shear, and elastic slip. By including slip, the analytical model produces a better match to the measured stiffness. However, the shape of the load-displacement relation is still too wide.

Figure 5.1.19c presents results for an analytical model that considers inelastic flexure, shear, and slip, as described previously. This model produces the best hysteretic response as it matches the initial stiffness, inelastic lateral strength, and load reversal behavior of the test beam reasonably well throughout the entire deformation history.

f. All Beam Models

Modeling elements described in preceding sections are implemented and calibrated for all other test beams. Important parameters used in beam models are listed in Table 5.1.2. These are taken from test data measured during tests. Overall model responses are plotted and compared against those measured during all beam tests in Figure 5.1.20 to Figure 5.1.23.

Table 5.1.2: Modeling Parameters in Beam Models

Parameters	SBH60	SBH100	SBL100	SBM100
Shear stiffness in section aggregator (kips/rad)	35000	35000	35000	35000
Slip at yield (inches)	0.025	0.045	0.055	0.055
Slip at ultimate (inches)	0.35	0.25	0.35	0.30
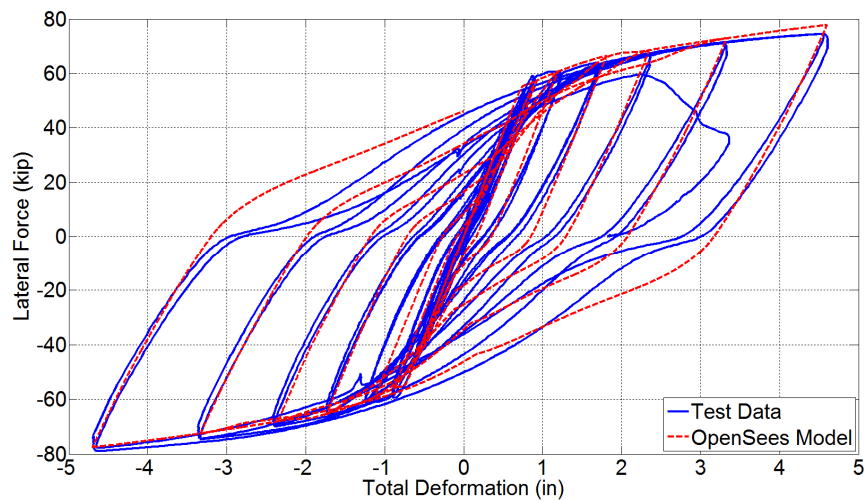
Figure 5.1.20: Overall Response of SBH60
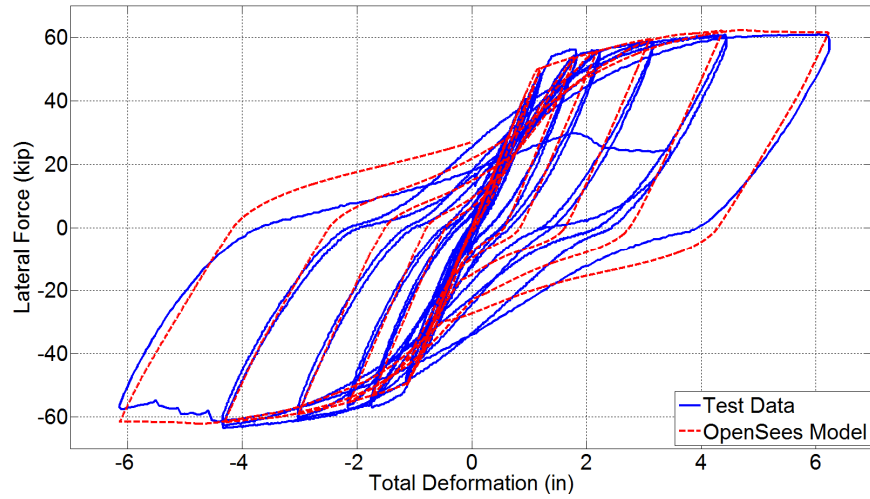
Figure 5.1.21: Overall Response of SBH100
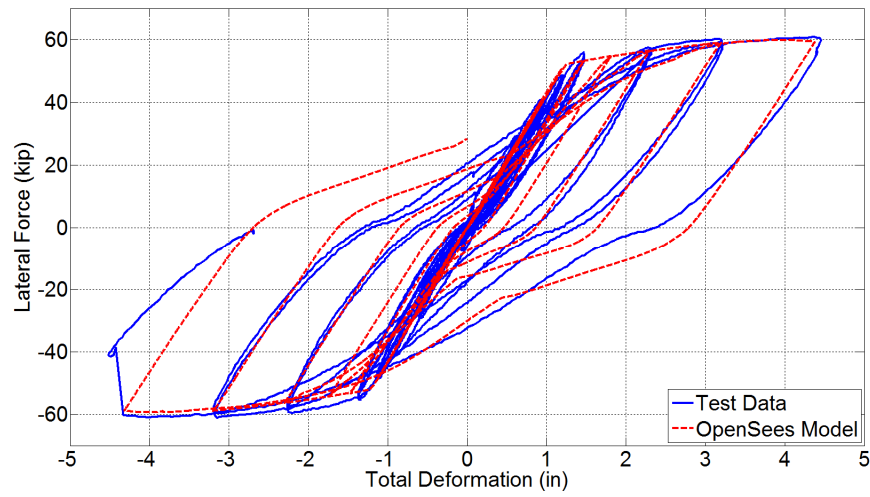
Figure 5.1.22: Overall Response of SBL100
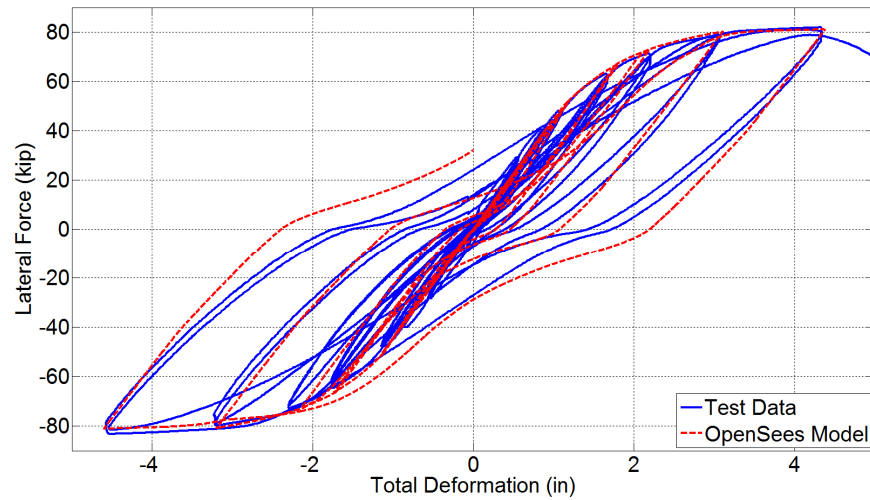
Figure 5.1.23: Overall Response of SBM100

5.2. COLUMNS

Similar development of OpenSees modeling is carried out to simulate the response of columns that were tested in a companion laboratory test program at the University of Texas, Austin. It has been observed through test data in the report of column test program (Sokoli et al., 2017) that shear deformation contributes a relatively small percentage to total deformation of all column tests. This is apparently because the axial load applied on the columns during the tests resulted in fewer flexural cracks and ultimately less deformation caused by shear. Therefore, the analytical model of the columns does not have the section aggregator to model shear deformation. The overall model includes only the force-based beam-column and the zero-length section elements to model flexure and slippage of longitudinal bar behaviors. The amount of slip is scaled proportionally from the measured slip in beam tests by the product $d_b \sqrt{f_c'}$ of the column over that of a beam, where d_b (inch) is the longitudinal bar diameter and f_c' (psi) is the concrete compressive strength, and is listed in Table 5.2.1. Responses of the OpenSees models and column test data are presented in Figure 5.2.1 through Figure 5.2.4.

Table 5.2.1: Slip Parameters in Column Models

Parameters	CH60	CH100	CL100	CM100
Slip at yield (inches)	0.02	0.034	0.041	0.041
Slip at ultimate (inches)	0.28	0.19	0.27	0.27
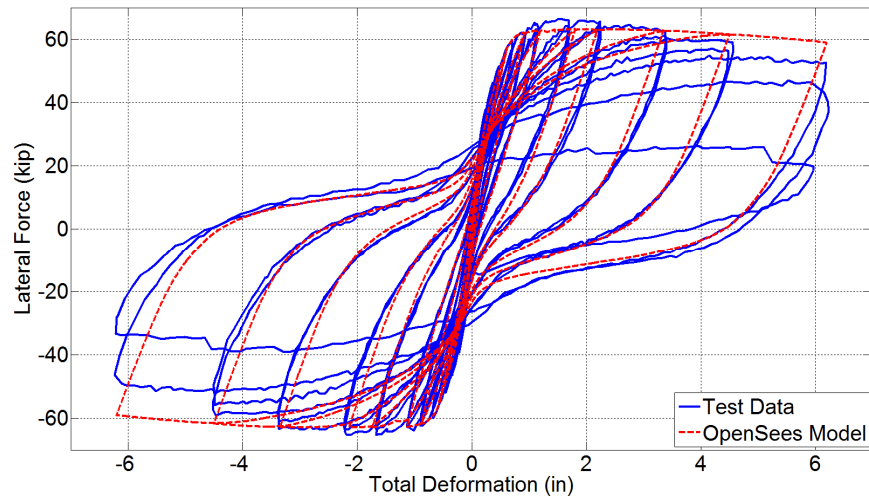
Figure 5.2.1: Overall Response of CH60
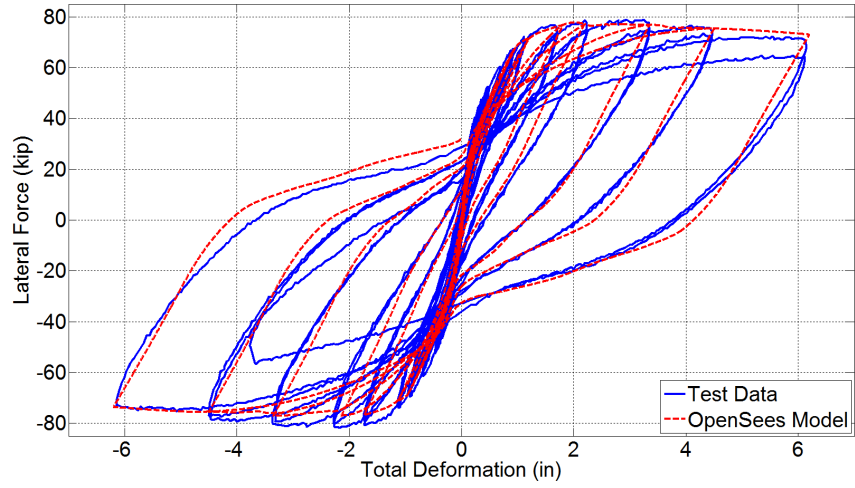
Figure 5.2.2: Overall Response of CH100
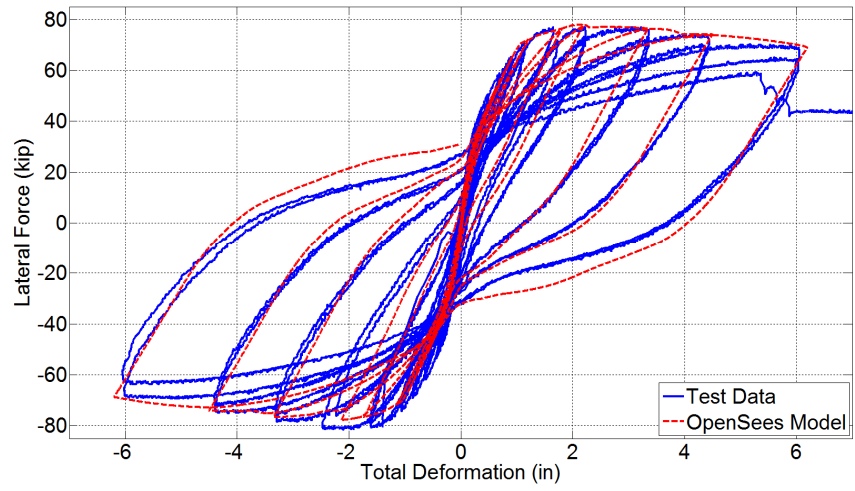
Figure 5.2.3: Overall Response of CL100
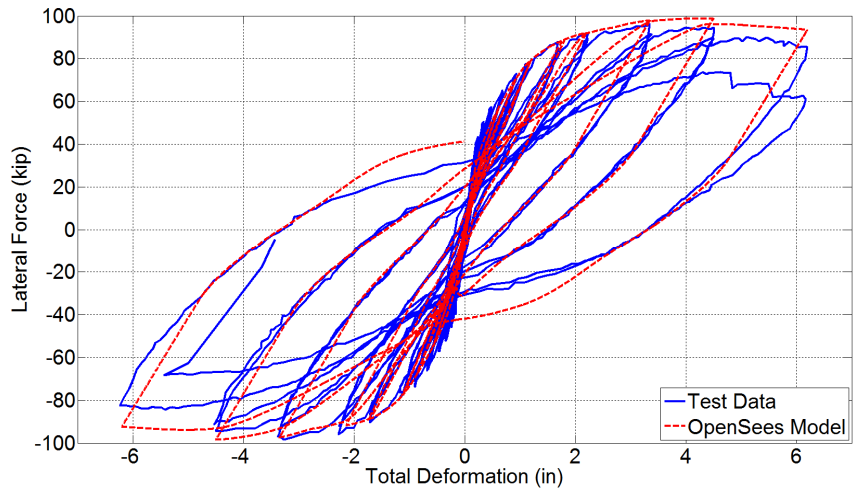
Figure 5.2.4: Overall Response of CM100

6. SEISMIC PERFORMANCE OF 20-STORY REINFORCED CONCRETE SPECIAL MOMENT RESISTING FRAMES

With the representative analytical model developed for beams and columns, representative frame buildings were designed and studied to explore the effects of high-strength reinforcement on seismic performance of frame buildings through nonlinear dynamic analyses.

6.1. BUILDING DESCRIPTION

Previous studies completed at UC Berkeley investigated seismic response of 20-story tall reinforced concrete office buildings with special moment resisting frames and conventional Grade 60 reinforcement (Visnjic, 2014). The same archetype building, shown in Figure 6.1.1, is re-designed with Grade 100 reinforcement based on design requirements per ASCE-7-16 and detailing requirements per ACI 318-14. As a result, there are total of four building models being studied including one building with conventional Grade 60 A706 (SBH60), one with Grade 100 having T/Y = 1.30 (SBH100), one with Grade 100 having T/Y = 1.18 (SBL100), and the last one with Grade 100 A1035 (SBM100). The naming convention of test beams is used for these archetype buildings.

These buildings have two reinforced concrete special moment resisting frames (SMRFs) as the seismic-force-resisting system in each of the two principal directions of the buildings. The special moment frame frames are located on the perimeter. They have four 21-ft long bays and twenty 12-ft tall stories to result in building height of 144 ft.
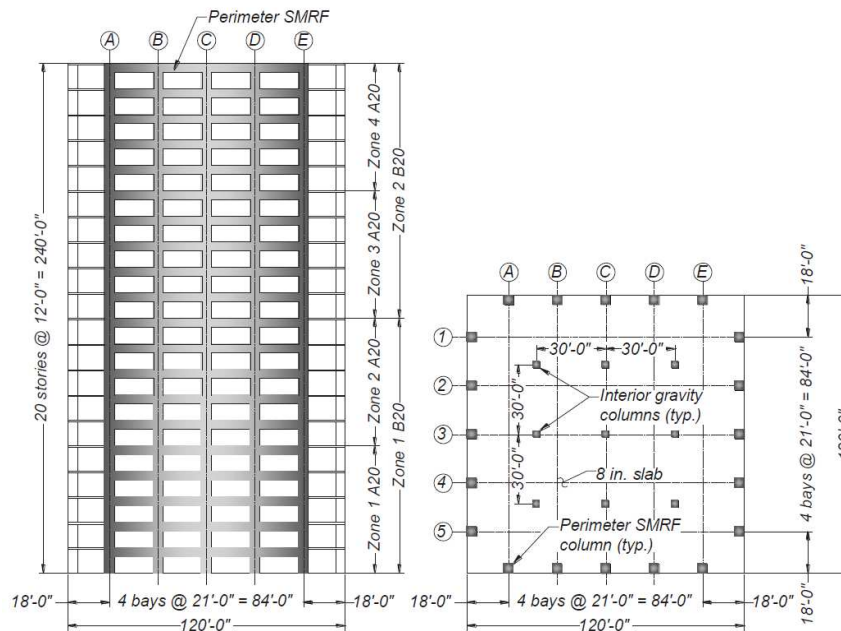
Figure 6.1.1: Elevation (Left) and Floor Plan (Right) of Archetype Buildings (used with permission from Visnjic 2014)

6.2. SEISMIC HAZARD

All four archetype buildings are hypothetically located in the financial district of downtown San Francisco, California (Figure 6.2.1). The soil condition at the selected location is categorized as stiff soil and site class D (ASCE 7). From the USGS seismic design map, the ordinates of the pseudo-acceleration spectrum at short- and 1-s-periods are $S_{DS} = 1.0g$ and $S_{D1} = 0.6$, respectively, where g is gravitational acceleration, for a design earthquake level and 5% damping. For the maximum considered earthquake hazard, the corresponding spectral ordinates are $S_{MS} = 1.5g$ and $S_{M1} = 0.9g$. Based on these spectral ordinates, the design and maximum considered earthquake spectra are constructed according to ASCE 7 and plotted in Figure 6.2.2. In this figure, the RotD50 component of the design spectrum is also plotted. The RotD50 spectrum is computed by dividing the MCE-level spectrum by 1.1 for period less than 0.6 second and by 1.3 otherwise.

Figure 6.2.1: Hypothetical Location of Archetype Buildings (marked with a bull's-eye)
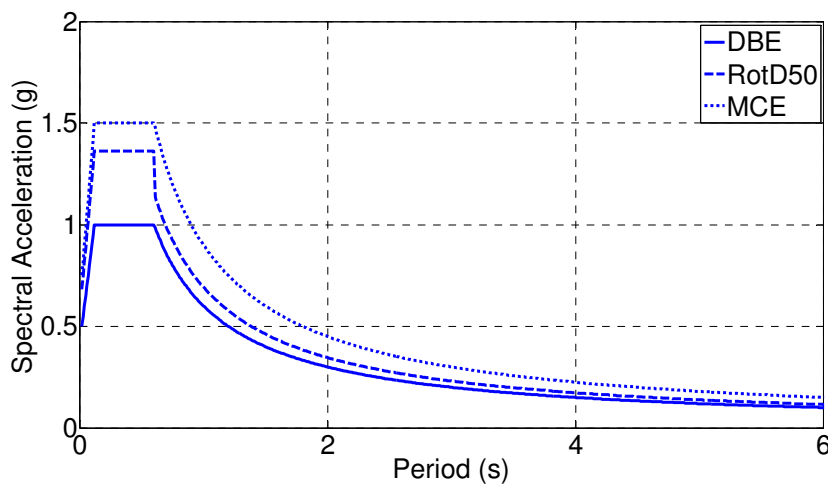
Figure 6.2.2: Pseudo-Acceleration Spectra for DE, RotD50, and MCE Hazard Level at 5% Damping

6.3. DESIGN OF BUILDINGS

The designs of four archetype buildings conform to the ASCE 7-16 and ACI 318-14 provisions. The design with conventional Grade 60 reinforcement serves as the base model. From this base design, the dimensions of all structural members are kept the same and all reinforcement is replaced with Grade 100 steel. Thus, the amount of reinforcement in all structural members is reduced appropriately to provide equivalent nominal strengths. By code-based design with linear elastic analysis, the designs of all four archetype frame buildings with normal and higher-grade steel are similar except the amount of reinforcement. All three buildings with Grade 100 are identical in design. The reason for this design approach is that most frames are designed near the building code design drift limit and, consequently, the gross cross sections cannot be decreased without violating the drift limit.

According to ASCE 7-16, the archetype buildings have Risk Category II, Seismic Importance Factor $I_e = 1.0$, and Seismic Design Category D. The design floor live load is 60 psf. Gravity loads include self-weight of structure and permanent non-structural components and contents.

The seismic weight of the archetype buildings includes 100% of dead load and 25% of live load. In each principal direction of the building, there are two special moment resisting frames that are symmetric over the center line of building plan. Therefore, half of total seismic weight is assigned to each frame and each frame is assumed to resist half of the total seismic force. Note that this sets aside the complication of accidental torsion.

The nominal concrete compressive strengths in design are 5.0 ksi for all beams, 8.0 ksi for all columns from the base to the 10th floor, and 7.0 ksi for all columns above the 10th floor. High-strength concrete is used in columns so as to follow the recommendation on column axial load that $P_u \leq 0.40 f_c' A_g$ (LATBSDC 2014). During the design procedure, there are two types of reinforcement used including Grade 60 and Grade 100 with nominal yield strengths of 60 ksi and 100 ksi, respectively.

The load combinations (numbered consistent with ASCE 7) considered in the design are the following:
2. $1.2D + 1.6L$
5. $1.2D + 0.5L \pm 1.0E + 0.2S_{DS}D$
7. $0.9D \pm 1.0E - 0.2S_{DS}D$
where:
    D = dead load,
    L = live load,
    E = earthquake load,
    S_{DS} = design spectral acceleration parameter at short periods (ASCE 7).

The design procedure follows guidance provided in a technical brief NIST GCR 16-917-40 document (Moehle and Hooper, 2016) and LATBSDC (2014). In design, the effective stiffnesses (cracked stiffnesses) used for beams and columns are $0.35 E_c I_g$ and $0.5 E_c I_g$, respectively, where $I_g =$ gross section moment of inertia and $E_c = 57,000 \sqrt{f_c'(psi)} \ (psi) =$ elastic modulus of concrete. Beam-column joints are modelled as partially rigid using the assumptions shown in Figure 6.3.1 (Birely et al. 2012). Columns at the base are fixed to the foundation at the ground level in the model as permitted by ASCE 7 §12.7.1 (Foundation Modeling).
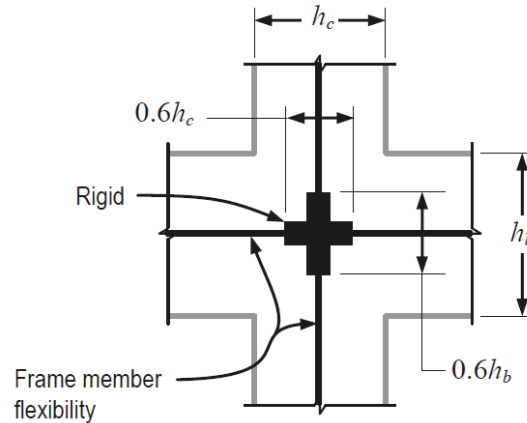
Figure 6.3.1: Partially Rigid Joint Model

The design model of the archetype frame is constructed in the computer software ETABS 2016 (Computers and Structures, Inc.) with all modeling recommendations described in the previous paragraph implemented. The code-prescribed Modal Response Spectrum Analysis (MRSA) procedure was used for seismic design. The complete quadratic combination (CQC) was used as the modal combination rule for the first twelve (12) modes in the MRSA, which accounted for more than 98% of the modal mass. The applicable response modification factor was $R = 8$. ASCE 7-16 requires that design base shear given by MRSA procedure must be scaled to 100% of calculated base shear using the Equivalent Lateral Force procedure.

From linear elastic frame model in ETABS, design flexural strength in beams is governed by the load combinations considered. Beam shear strength demand is computed using probable moment strength of beam M_{pr}. Design axial force in columns is determined assuming an all-beams yielding mechanism with reduction factor of 0.8. Gravity load is also included in column axial demands in accordance with the controlling load combination. Column flexural strength is governed by design principle of strong columns and weak beams, as specified by the requirement $\sum M_{nc} \geq \frac{6}{5} \sum M_{nb}$ (ACI 318-14).

Peak story drifts were calculated in the MRSA procedure with design spectrum being scaled such that modal base shear is equal to base shear determined in accordance with Eq. 12.8-6 in ASCE 7-16. They are then multiplied by appropriate deflection amplification factor $C_d = 5.5$ for reinforced concrete frame buildings. All four buildings satisfy story drift limit of $0.02 h_{sx}$ per ASCE 7-16 ($h_{sx} =$ story height).

Table 6.3.1 summarizes important design criteria; Table 6.3.2 presents the dimensions and longitudinal reinforcement. Note that beams and interior columns have constant cross section in the lower ten stories, with reduced sections in stories 11-20. Exterior columns were constant in stories 1-5, 6-10, and 11-20. Table 6.3.3 displays design drift ratio of the archetype frames determined by linear elastic analysis under design level hazard.

Table 6.3.1: Summary of Design Criteria

Building	Grade 60	Grade 100
Name	SBH60	SBH100, SBL100, SBM100
Risk Category	II	II
Seismic Importance Factor, I_e	1.0	1.0
Seismic Design Category	D	D
Seismic Response Modification Factor, R	8	8
Drift Amplification Factor, C_d	5.5	5.5
Live load (psf)	60	60
Seismic Weight per Frame, W ($kips$)	23,000	23,000
Design Base Shear Coefficient, V_b/W	0.044	0.044
Base Shear Coefficient for Scaling of Drift	0.038	0.038
Concrete strength in beams, f_c' (ksi)	5.0	5.0
Concrete strength in columns (1st-10th floors), f_c' (ksi)	8.0	8.0
Concrete strength in columns (11th -20th floors), f_c' (ksi)	7.0	7.0
Steel yield strength, f_y (ksi)	60	100
Beam effective stiffness	$0.35E_cI_g$	$0.35E_cI_g$
Column effective stiffness	$0.5E_cI_g$	$0.5E_cI_g$

Table 6.3.2: Dimensions and Reinforcement of Design Frames

Design		Grade 60				Grade 100			
Zone		1	2	3	4	1	2	3	4
Story		1-5	6-10	11-15	16-20	1-5	6-10	11-15	16-20
Beam	b (in.)	24	24	24	24	24	24	24	24
	h (in.)	40	40	40	40	40	40	40	40
	Top & Bottom Reinforcement	7 No. 10	7 No. 10	7 No. 9	7 No. 9	5 No. 9	5 No. 9	5 No. 8	5 No. 8
Ext. Col	b (in.)	42	42	36	36	42	42	36	36
	h (in.)	42	42	36	36	42	42	36	36
	Perimeter Reinforcement	28 No. 10	20 No. 9	20 No. 9	20 No. 9	24 No. 9	16 No. 8	16 No. 8	16 No. 8
Int. Col	b (in.)	42	42	36	36	42	42	36	36
	h (in.)	42	42	36	36	42	42	36	36
	Perimeter Reinforcement	20 No. 9	20 No. 9	20 No. 9	20 No. 9	16 No. 8	16 No. 8	16 No. 8	16 No. 8

Table 6.3.3: Design Drift of Archetype Frames

Story	Design Level Drift Ratio
20	0.005
19	0.007
18	0.008
17	0.010
16	0.011
15	0.012
14	0.013
13	0.013
12	0.014
11	0.014
10	0.014
9	0.014
8	0.014
7	0.015
6	0.015
5	0.015
4	0.016
3	0.016
2	0.014
1	0.008

6.4. NUMERICAL MODEL

A two-dimensional numerical model of a single special moment frame in the archetype building was constructed and nonlinear history analysis (NRHA) was performed using the Open System for Earthquake Engineering Simulation software platform (McKenna et al. 2007, OpenSees 2016).

Mass and load: seismic mass is lumped and gravity load is applied at the joints. Both seismic mass and gravity load include 100% of dead load and 25% of live load in accordance with ASCE 7.

Gravity framing and foundation: gravity framing is assumed to have sufficient strength and stiffness to resist $P - \Delta$ effects under gravity load. It is also assumed to not provide lateral resistance (Haselton et al. 2008). Foundation flexibility is not modeled and all columns at base level are fixed to the "ground."

Frame elements and joints: all beams and columns are modeled as described in Chapter 5. Force-based Euler-Bernoulli nonlinear fiber-section frame elements with five Gauss-Lobatto integration points and $P - \Delta$ geometric transformation are used to model flexural behavior. Axial force – bending moment interaction is modeled but shear force – bending moment and/or axial force interaction is not considered. Beam-column joints are modeled with rigid end zones in both columns and beams (Figure 6.4.1). Slab effects are not considered in the numerical model.

Rotational springs (slip of reinforcement): strain penetration of beam longitudinal reinforcement into joints and column longitudinal reinforcement into the foundation are modeled through nonlinear rotational spring by using zero-length section element as described in Chapter 5. For different sizes of reinforcement, the amount of slip is scaled linearly proportionally from the measured slip in beam tests by the product $d_b\sqrt{f_c'}$ where d_b (inch) is the longitudinal bar diameter and f_c'(psi) is the concrete compressive strength.

Section aggregator (shear): shear behavior in beams is only modeled by linear elastic property. The reason is that under ground motion excitation, effect of beam elongation, and kinematics with different column elements, axial force is developed in beams and moment strength of beam constantly changes as a result. The Ibarra-Medina-Krawinkler model for shear response through the use of section aggregator does not model shear-moment interaction. Since deformation contribution from shear into total deformation of beam is very little as observed in beam tests and discussed in Chapter 3, shear response modeled only by linear elastic property is deemed sufficient and overall behavior of beam models remain very similar to that shown in Chapter 5. Elastic stiffness of shear in frame elements is proportionally scaled from the measured one in beam tests by the product $A_g\sqrt{f_c'}$ where A_g (in^2) is the frame element cross-sectional area and f_c'(psi) is the concrete compressive strength. Shear is not modeled in columns.

Material properties: expected material properties are used in the frame model (TBI 2016). Yield strength of Grade 60 A706 is taken to be 65 ksi, the value measured in test of specimen SBH60. Expected yield strengths of Grade 100 with distinct yield plateau (SBH100 and SBL100) are both 105 ksi in frame model but frame SBH100 has Grade 100 steel with higher strain hardening ratio as the intent of dynamic analysis study is to explore this effect on the seismic performance of two archetype frames with different types of reinforcement. Concrete strength is 1.3 times specified compressive strength of 8 ksi.
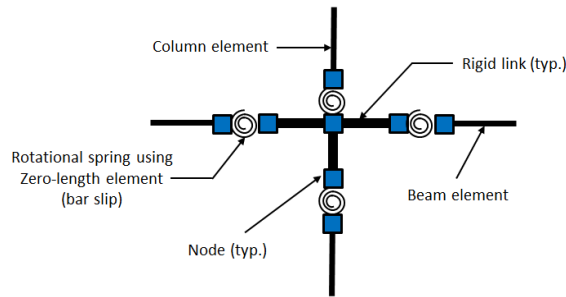
Figure 6.4.1: Typical Model at the Joint

Damping forces: as studied by many researchers, initial stiffness Rayleigh damping has been recognized to cause spurious forces in the system and equilibrium is not maintained (Chopra and McKenna, 2016). Therefore, tangent stiffness Rayleigh damping is implemented in the frame model such that equilibrium is satisfied everywhere in the system. The damping matrix is defined as a linear combination of mass matrix and tangent stiffness matrix Rayleigh damping with 2% damping ratio applied in modes 1 and 3. Damping coefficients calculated from 1st and 3rd modal properties of frame SBH60 are used to define the damping matrix in analyses of all frames studied here.

Cyclic response of typical beam and column in studied frames is presented in **Figure 6.4.2** through **Figure 6.4.7**. Figure 6.4.2 displays cyclic behavior of typical beam from base to 10th floor of frames SBH60 and SBL100. Beams in frame SBH60 are apparently stiffer and have higher peak strength than those in frame SBL100 because of greater longitudinal reinforcement area and material strain hardening. They both have similar yield strength as expected in the design. Figure 6.4.3 shows comparison of response between beams of frames SBH100 and SBL100. They both have equivalent stiffness and strength at yield. Beam in SBH100 is stronger after yielding as its longitudinal reinforcement has higher strain hardening ratio. In **Figure 6.4.4**, it is also obvious that beam in frame SBH60 is stiffer than that of beam in frame SBM100.

Similar trend can be made for response of a typical exterior column in frame models. The column in frame SBH60 clearly shows higher initial stiffness than other columns in frames with high-strength steel. It has slightly higher strain hardening behavior after yielding. In **Figure 6.4.6**, the column in frame SBH100 obviously responds better after yield than that in frame SBL100

due to higher strain hardening ratio. The column in frame SBM100 has the higher peak strength but its strength degrades quicker than the column in SBH60 (Figure 6.4.7).
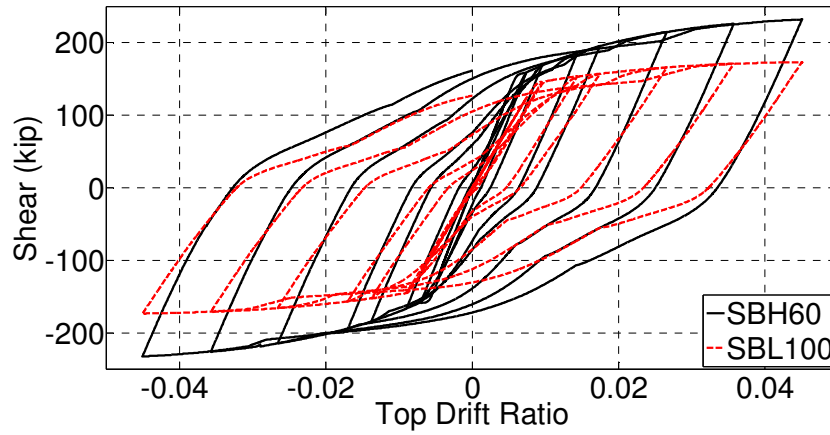
Figure 6.4.2: Cyclic Response of Typical Beams in Frames SBH60 and SBH100
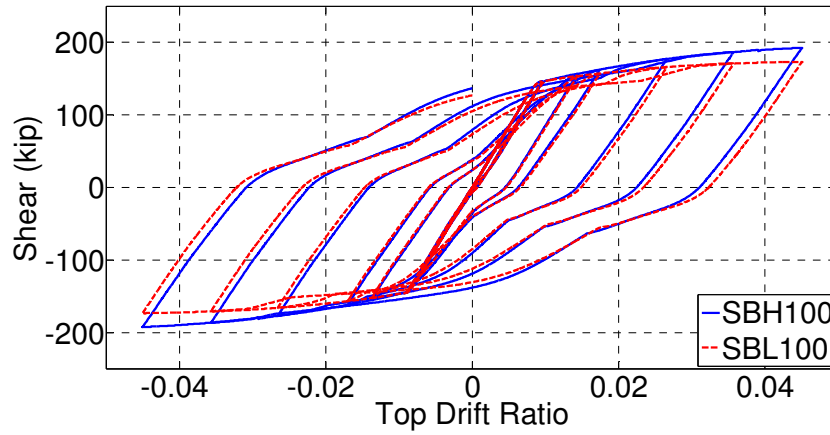
Figure 6.4.3: Cyclic Response of Typical Beams in Frames SBH100 and SBL100
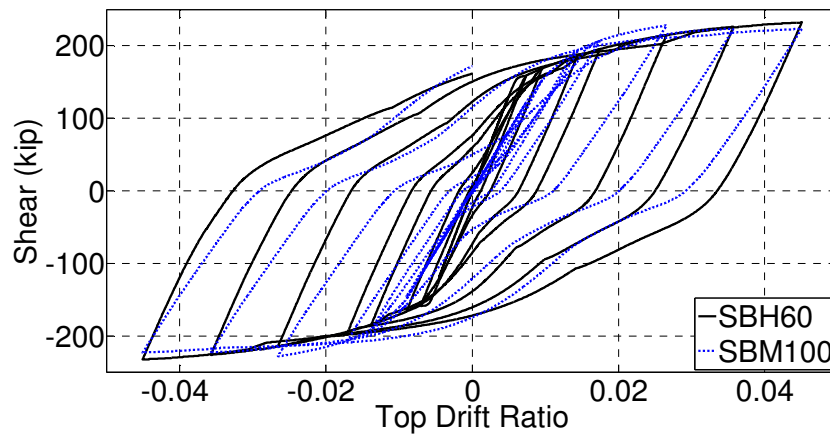
Figure 6.4.4: Cyclic Response of Typical Beams in Frames SBH60 and SBM100
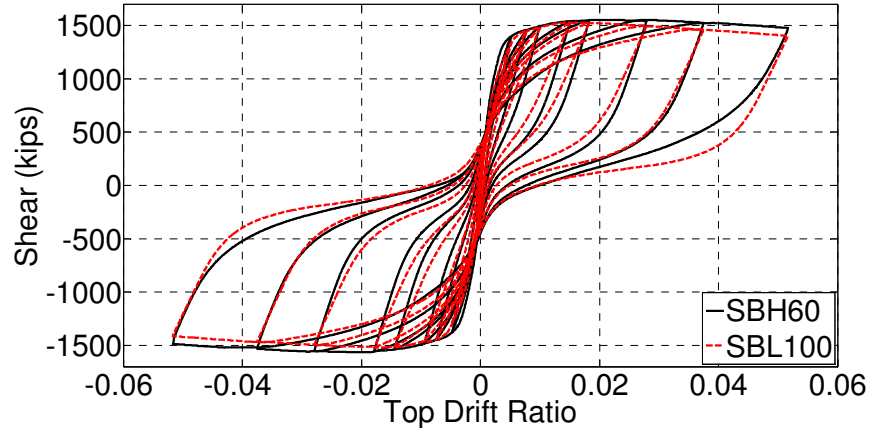
Figure 6.4.5: Cyclic Response of Typical Exterior Column in Frames SBH60 and SBH100
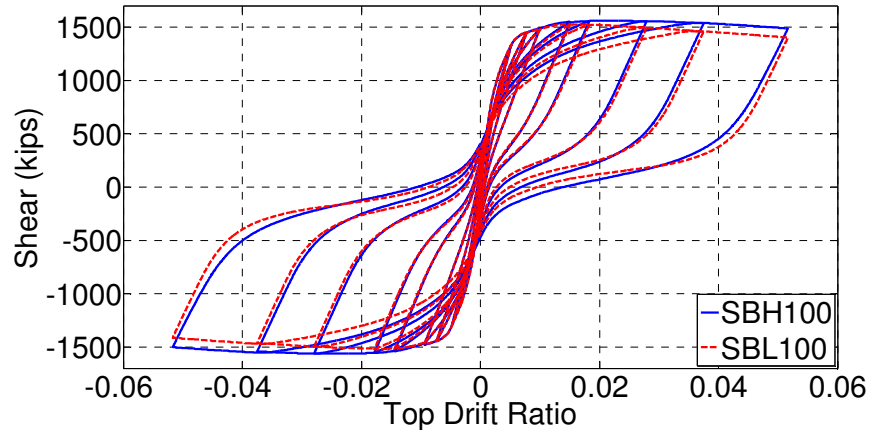
Figure 6.4.6: Cyclic Response of Typical Exterior Column in Frames SBH100 and SBL100
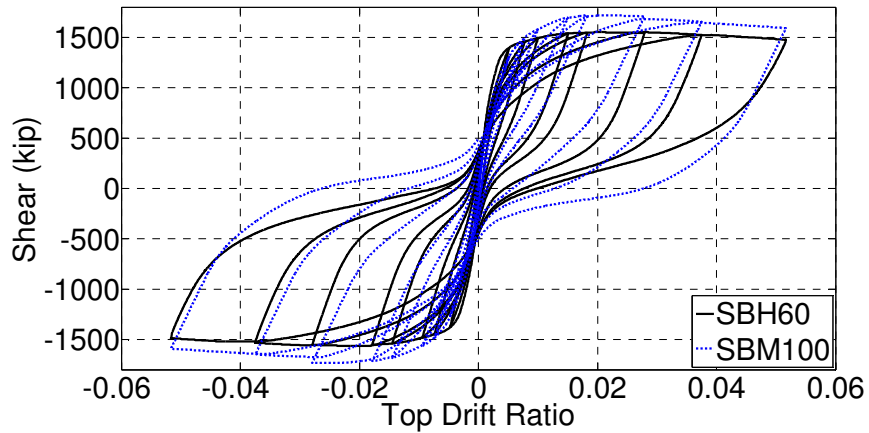
Figure 6.4.7: Cyclic Response of Typical Exterior Column in Frames SBH60 and SBM100

6.5. VIBRATION PROPERTIES AND STRENGTH

Modal periods of the first three translational modes of the planar model based on cracked section properties are listed in Table 6.5.1. In the ETABS model, cracked-section properties are modeled by applying effective stiffness for beams and columns of $0.35E_cI_g$ and $0.5E_cI_g$, respectively. In the OpenSees model with fiber sections, modal periods are computed after gravity load is applied onto the frame.

A nonlinear static push-over analysis under lateral load pattern that is similar to the ASCE 7 Equivalent Lateral Force is performed for all frame models after application of gravity loads. The results are plotted in Figure 6.5.1. It is worth noting that frame SBH60 reinforced with conventional Grade 60 A706 steel and larger amount of longitudinal reinforcement is stiffer than the other three frames with Grade 100 reinforcement. All frames with higher-grade steel have the same initial stiffness. Additionally, frame SBH100 is stronger than SBL100 after yielding as its reinforcement has higher strain hardening. Similar observation is made for SBH60 as compared to the response of SBH100 and SBL100. SBM100 has the highest peak strength as expected because Grade 100 A1035 has the highest ultimate stress of the four types of steels.

Table 6.5.1: Period of First Three Translational Modes of Archetype Buildings

Building	Mode	ETABS Period (s)	OpenSees Period (s)
SBH60	1	3.41	3.18
	2	1.16	1.07
	3	0.65	0.60
SBH100, SBL100, SBM100	1	3.41	3.82
	2	1.16	1.29
	3	0.65	0.71
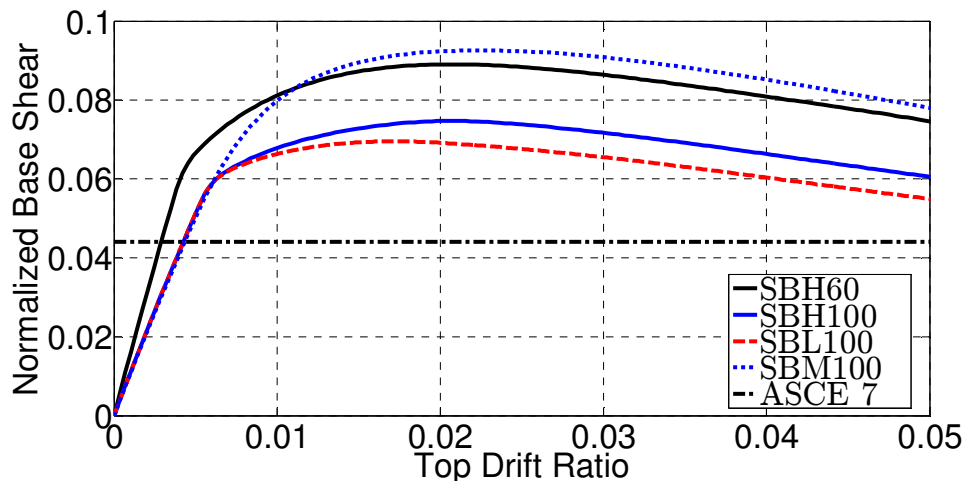
Figure 6.5.1: Push-Over Curves for All Frame Models under ASCE 7 Lateral Load Pattern

6.6. GROUND MOTION SELECTION

Dynamic analyses are performed at two levels of shaking intensities: maximum considered earthquake (MCE) and the average RotD50. Ground motions are selected using a Matlab routine developed by the Baker Research Group (Jayaram et al. 2011).

Twenty ground motions are selected such that the average spectrum of fault-normal (FN) component spectra of all ground motions approximates the MCE response spectrum defined in section 5.2. From these selected motions, the individual fault-parallel (FP) components are scaled to agree with the RotD50 response spectrum. The selection restrictions are: 1) magnitude of the earthquake is between 6.5 and 8.0; 2) distance to site is within 20 kilometers; and 3) the scale factor is from 0.5 to 5.0. The set of 20 selected ground motions also contains about 10 near-fault pulse-like motions that have distinct velocity pulses due to directivity effects.

Table 6.6.1 lists the individual ground motion information and their scale factors. Their FN- and FP-component pseudo-acceleration spectra are plotted in Figure 6.6.1 and Figure 6.6.2. The average spectrum of FN and FP components are also shown and compared to the target MCE and RotD50 spectra in these plots, respectively.

Table 6.6.1: Selected Ground Motions and Scale Factors

GM No.	Record Sequence Number	Earthquake Name	Year	Station Name	Scale Factor FN	Scale Factor FP
1	6	Imperial Valley-02	1940	El Centro Array #9	3.60	2.20
2	126	Gazli, USSR	1976	Karakyr	1.50	1.30
3	174	Imperial Valley-06	1979	El Centro Array #11	3.50	2.00
4	182	Imperial Valley-06	1979	El Centro Array #7	0.80	1.50
5	184	Imperial Valley-06	1979	El Centro Differential Array	1.50	1.40
6	495	Nahanni, Canada	1985	Site 1	2.30	3.50
7	721	Superstition Hills-02	1987	El Centro Imp. Co. Cent	2.10	3.00
8	725	Superstition Hills-02	1987	Poe Road (temp)	3.60	2.00
9	728	Superstition Hills-02	1987	Westmorland Fire Sta	2.80	2.30
10	779	Loma Prieta	1989	LGPC	0.80	1.20
11	802	Loma Prieta	1989	Saratoga - Aloha Ave	1.80	2.40
12	803	Loma Prieta	1989	Saratoga - W Valley Coll.	1.80	1.60
13	827	Cape Mendocino	1992	Fortuna - Fortuna Blvd	3.20	3.80
14	1045	Northridge-01	1994	Newhall - W Pico Canyon Rd.	1.00	1.70
15	292	Irpinia, Italy-01	1980	Sturno (STN)	1.75	1.50
16	6906	Darfield, New Zealand	2010	GDLC	1.20	0.70
17	8119	Christchurch, New Zealand	2011	Pages Road Pumping Station	0.85	2.50
18	1605	Duzce, Turkey	1999	Duzce	1.40	1.00
19	2655	Chi-Chi, Taiwan-03	1999	TCU122	2.80	5.00
20	2658	Chi-Chi, Taiwan-03	1999	TCU129	3.60	5.00
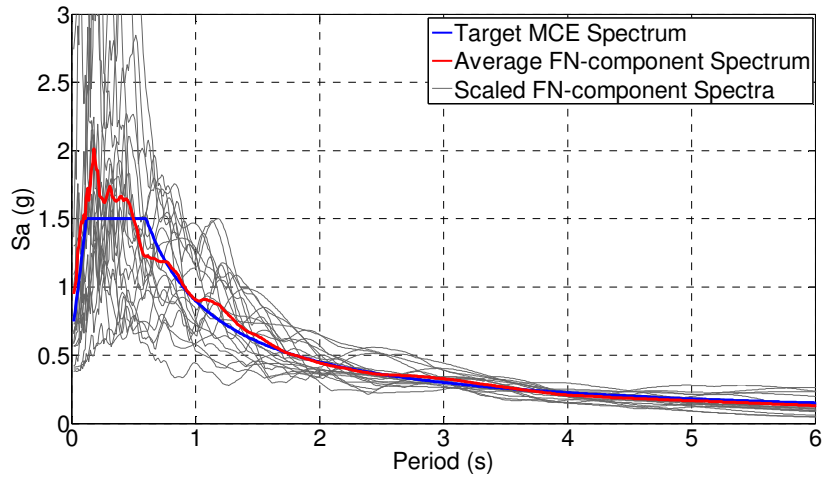
Figure 6.6.1: Pseudo-Acceleration Spectra for FN Components
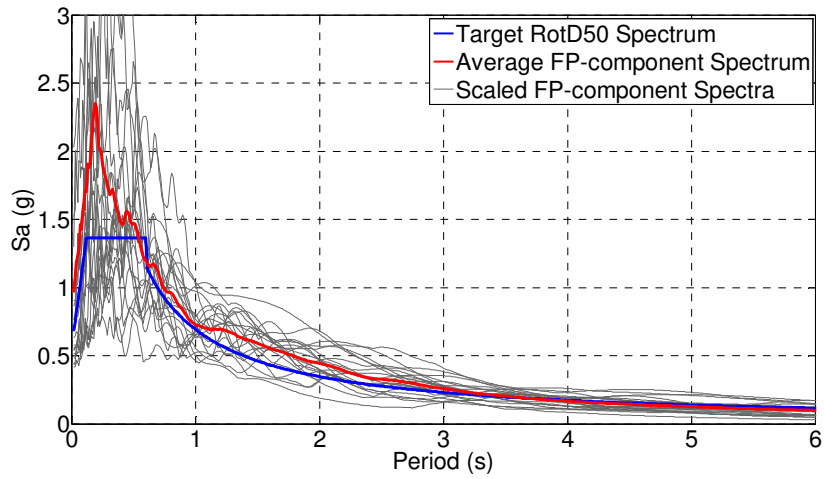
Figure 6.6.2: Pseudo-Acceleration Spectra for FP Components

6.7. RESULTS FROM NONLINEAR RESPONSE HISTORY ANALYSIS

General dynamic response characteristics of archetype buildings are discussed in this section. Figure 6.7.1 shows the history of roof displacement of all four frames subjected to fault-normal (FN) component of the ground motion recorded at station TCU 129 during the Chi-Chi earthquake in Taiwan 2003. Frame SBH60 with conventional Grade 60 A706 reinforcement achieved the least roof displacement of all the studied buildings as expected due to its greater stiffness. Frames SBH100 and SBL100 are both identical in all aspects except the strain-hardening property of the longitudinal reinforcement, resulting in almost the same roof response history. Lastly, frame SBM100 produces the largest roof displacement of all frames. It is also worth pointing out that roof level residual deflection for all three frames with Grade 100 reinforcement is slightly higher than that of the frame with conventional Grade 60 steel.

Zooming in on the history of the roof displacement as shown in Figure 6.7.1, it can be observed that frame SBH60 has a shorter period than the other three frames. Frame SBH60 responds mainly at period about 4.5 seconds while the other frames respond at period of approximately 5.0 seconds.
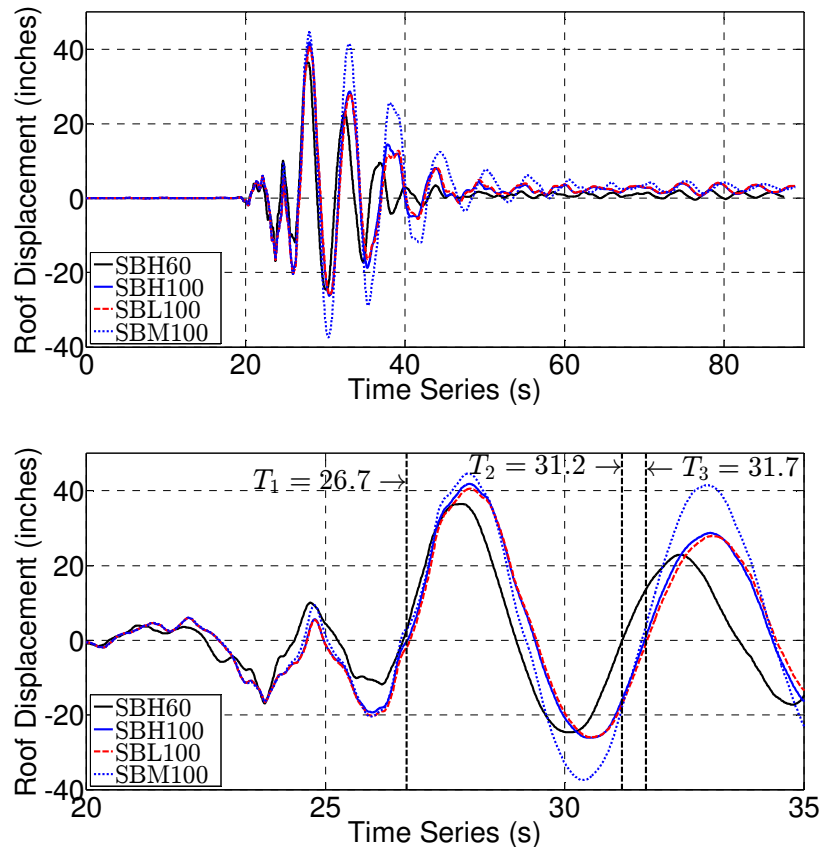
Figure 6.7.1: Roof Displacement Response History of All Frames under Record Number 2658 – Earthquake: Chi-Chi, Taiwan-03 – Station Name: TCU 129 – FN Component

Figure 6.7.2 plots calculated roof displacement histories of the four buildings under the FN component of ground motion recorded at station El Centro Imp. Co. Cent from the Superstition Hills-02 earthquake. Figure 6.7.3 plots calculated stress-strain behavior of a representative beam element for the four buildings. In response under this motion, the beam element in frame SBH60 sustained the least calculated strain demand, mainly because the roof deflection is the least among the four buildings. Grade 100 A1035 steel used in frame SBM100 sustains the largest strain. Frames SBH100 and SBL100 have very similar calculated strains that are between strains calculated for Frames SBH60 and SBM100.
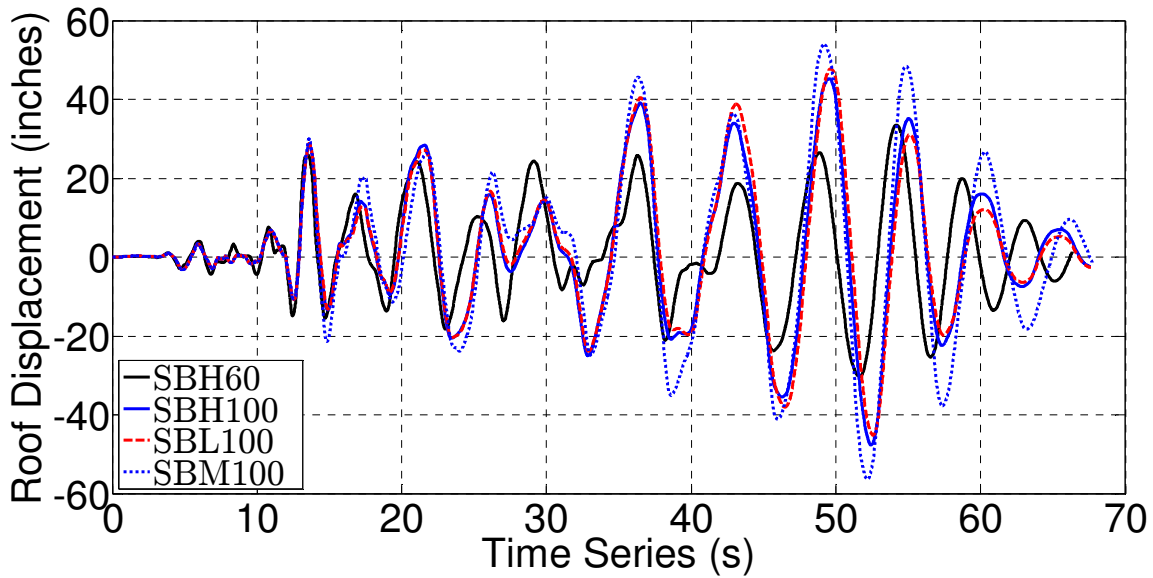
Figure 6.7.2: Roof Displacement Time Series of All Frames Subjected to Record Number 721 – Earthquake: Superstition Hills-02 – Station Name: El Centro Imp. Co. Cent – FN Component
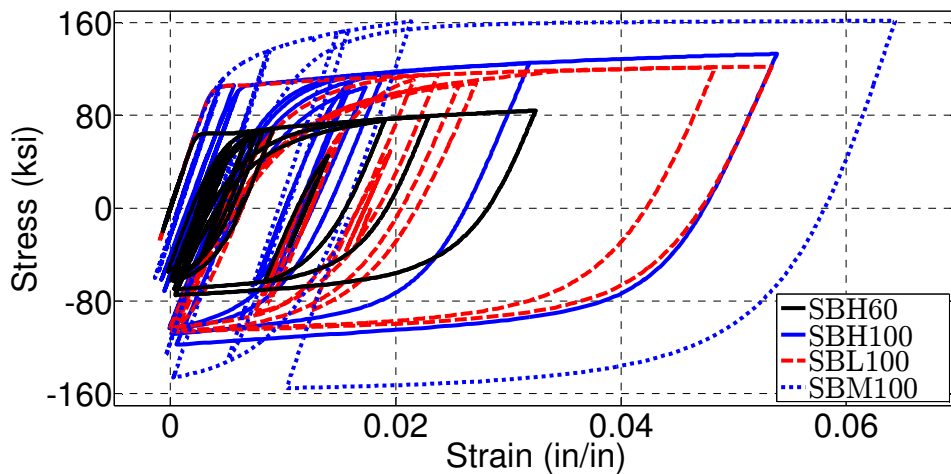
Figure 6.7.3: Stress-Strain Responses of One of the Beams in Frames Subjected to Record Number 721 – Earthquake: Superstition Hills-02 – Station Name: El Centro Imp. Co. Cent – FN Component

To study further into the difference in behavior between frames SBH100 and SBL100, analysis data of these two frames subjected to the ground motion measured at station El Centro Array #9 from the Imperial Valley-02 earthquake is plotted in Figure 6.7.4. Despite the slight discrepancy in roof displacement response in the positive direction, the peak roof deflections are comparable for both frames. Typical beam in frame SBH100 attains lower peak strain than that in SBL100 as shown in Figure 6.7.5, most likely due to higher-strain hardening property of reinforcement. However, this higher-strain hardening increases moment strength in beams in frame SBH100, which in turn results in higher moment demand on the columns. Therefore, stress demand in longitudinal reinforcement in the columns is higher for frame SBH100, resulting in larger strain and rotation in the columns.
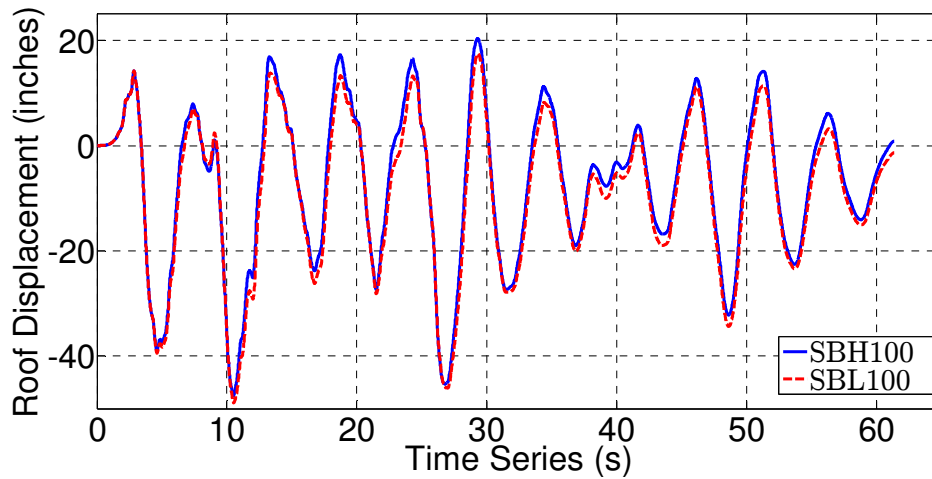
Figure 6.7.4: Roof Displacement Time Series of Frames SBH10 and SBL100 Subjected to Record Number 006 – Earthquake: Imperial Valley-02 – Station Name: El Centro Array #9
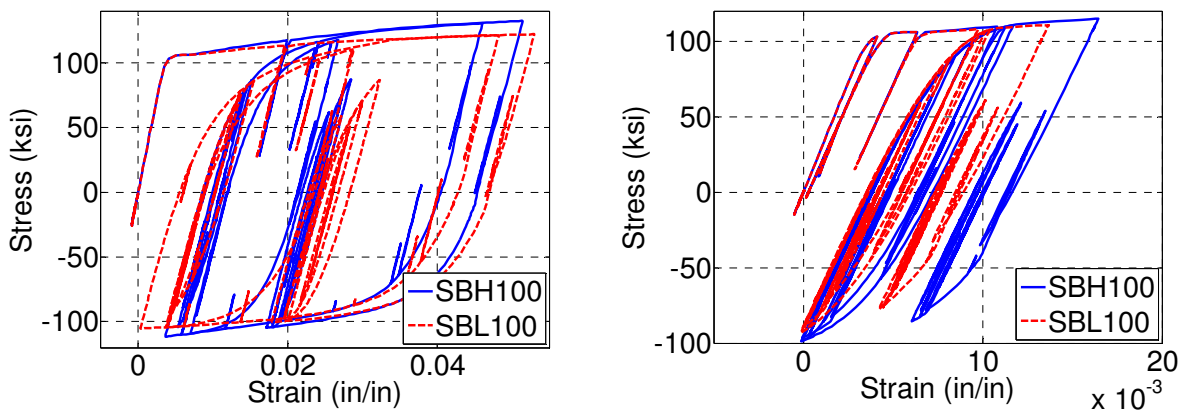
Figure 6.7.5: Stress-Strain Response of Frame Elements in SBH10 and SBL100 Subjected to Record Number 006 – Earthquake: Imperial Valley-02 – Station Name: El Centro Array #9 – Left: One of Beams – Right: Exterior Column at Base

Individual ground motion response quantities can be found in APPENDIX B. Average envelopes of all analyses including FN and FP components are presented in Figure 6.7.6 through Figure 6.7.9.

In Figure 6.7.6, drift along height of buildings is normalized by building height. It is apparent that frame SBH60 with conventional Grade 60 A706 reinforcement achieves the least roof drift of 1.15% while frame SBM100 with Grade 60 A1035 produces the largest roof drift of all frames at about 1.45%. Buildings SBH100 and SBL100 both obtain equivalent roof drift of 1.3%. Similar observation is made for story drift ratios plotted in Figure 6.7.7.
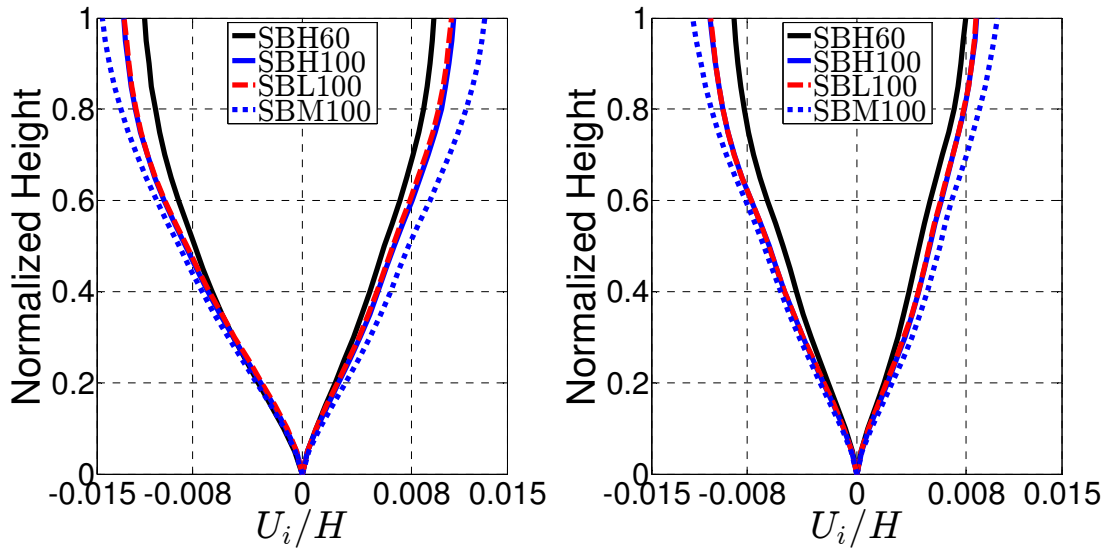
Figure 6.7.6: Average Displacement Envelopes – Left: FN Component – Right: FP Component
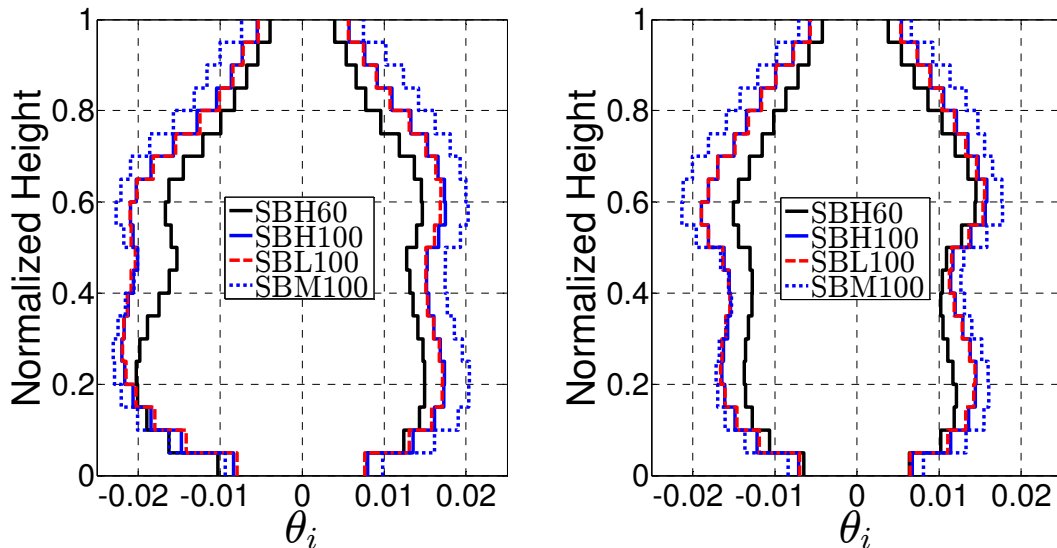
Figure 6.7.7: Average Story Drift Envelopes – Left: FN Component – Right: FP Component

Story shear is shown in Figure 6.7.8. Frame SBL100 attracts the least amount of story shear (approximately 10% of seismic weight) as expected since its longitudinal reinforcement of Grade 100 T/Y = 1.18 is the type of steel with lowest strain-hardening ratio. SBH100 with Grade 100 having slightly higher strain-hardening (T/Y = 1.30) attracts a little more shear force. Frame SBH60 attracts larger story shear force that SBL100 and SBH100. This may be attributable to larger amount of reinforcement and therefore greater stiffness, as well as higher strain-hardening ratio than both Grade 100 steels with distinct yield plateau. Frame SBM100 develops the most story shear of about 11.4% of the seismic weight, an increase of 12.3% compared to SBL100 and SBH100. This result is not unexpected, as Grade 100 A1035 has the highest ultimate stress of all higher-grade reinforcement and SBM100 is the strongest frame by the push-over analysis.
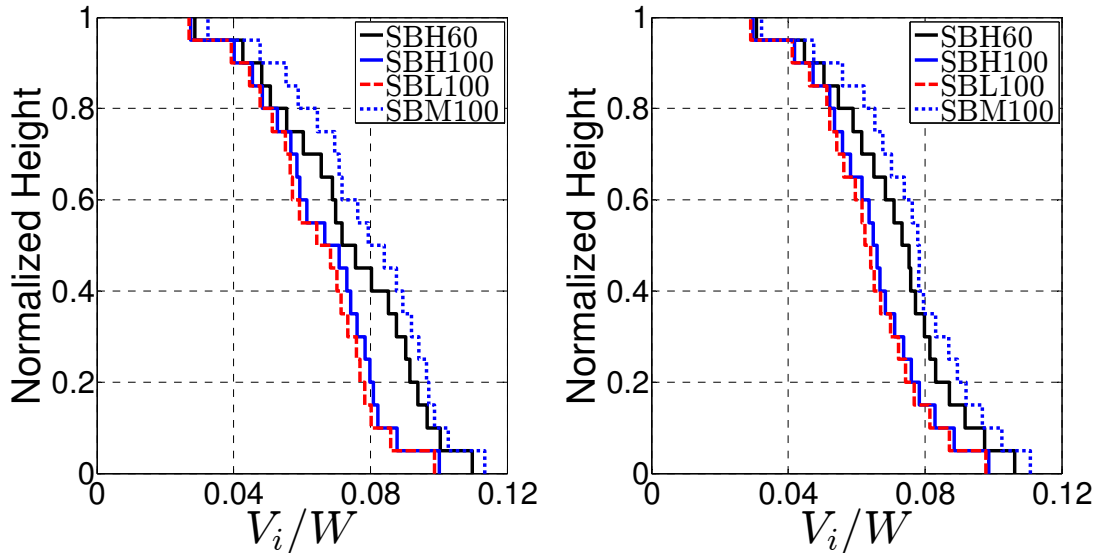
Figure 6.7.8: Average Story Shear Envelopes – Left: FN Component – Right: FP Component
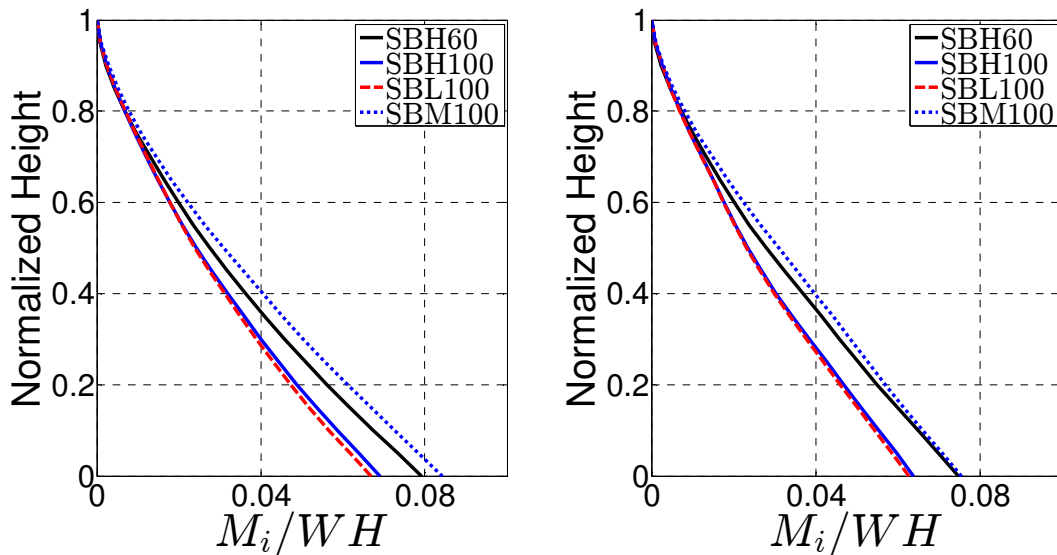
Figure 6.7.9: Average Story Moment Envelopes – Left: FN Component – Right: FP Component

Column Forces

Axial forces: axial forces in exterior columns of special moment frames subjected to earthquake excitation come from shear forces applied by moment frame beams responding at or near probable moment strengths plus column self-weight. Dead loads plus some portion of live loads may also result in additional vertical inertial forces if vertical ground motion component is present. In the present study, the effect of vertical ground motions was not included. Column axial force for design at level *i* can be estimated by:

$$P_{u,i} = P_{g,i} \pm \gamma_P \sum_{j=i}^{N} V_{pr,j} \qquad \text{Eq. (9)}$$

where $P_{u,i}$ = design axial force at level *i*,

$P_{g,i}$ = design axial force at level *i* due to gravity loads (1.0D + 0.25L)

$V_{pr,j}$ = shear due to M_{pr} at both levels of the beam at level *j* under zero gravity

γ_P = reduction factor to recognize that not all beams develop M_{pr} simultaneously, taken as 0.8 in this report as supported by Visnjic et al. (2014).

According to ACI 318-14, M_{pr} is calculated by using nominal (specified) concrete compressive strength $f_c' = 5000\ psi$ and elasto-plastic stress-strain relation for steel with yield stress equal to 1.25 times specified yield stress.

Comparison between external column axial forces calculated by the above equation and the average of those computed from dynamic analyses is presented in Figure 6.7.10 to Figure 6.7.13.

In Figure 6.7.10, it is observed that above equation marginally overestimates axial forces in columns on top stories and underestimates those on lower stories for frame SBH60. The equation slightly overestimates axial loads for columns in all floors of frame SBL100, probably because of the lower hardening ratio of Grade 100 T/Y = 1.18 reinforcement used in frame SBL100.

In Figure 6.7.11, it is apparent that the equation considerably underestimates axial forces in column in frame SBM100. This occurs mainly because the ultimate strength of Grade 100 A1035 is about 1.6 times its specified nominal yield strength of 100 ksi, which is much higher than the factor 1.25 in calculation of M_{pr} in beams.

In tension, the equation consistently overestimates the tensile force in columns in all frames except those columns on the lowest stories in frame SBM100. The abrupt change in normalized axial loads at mid-height of buildings is due to the difference in sizes and concrete strength used in column design.
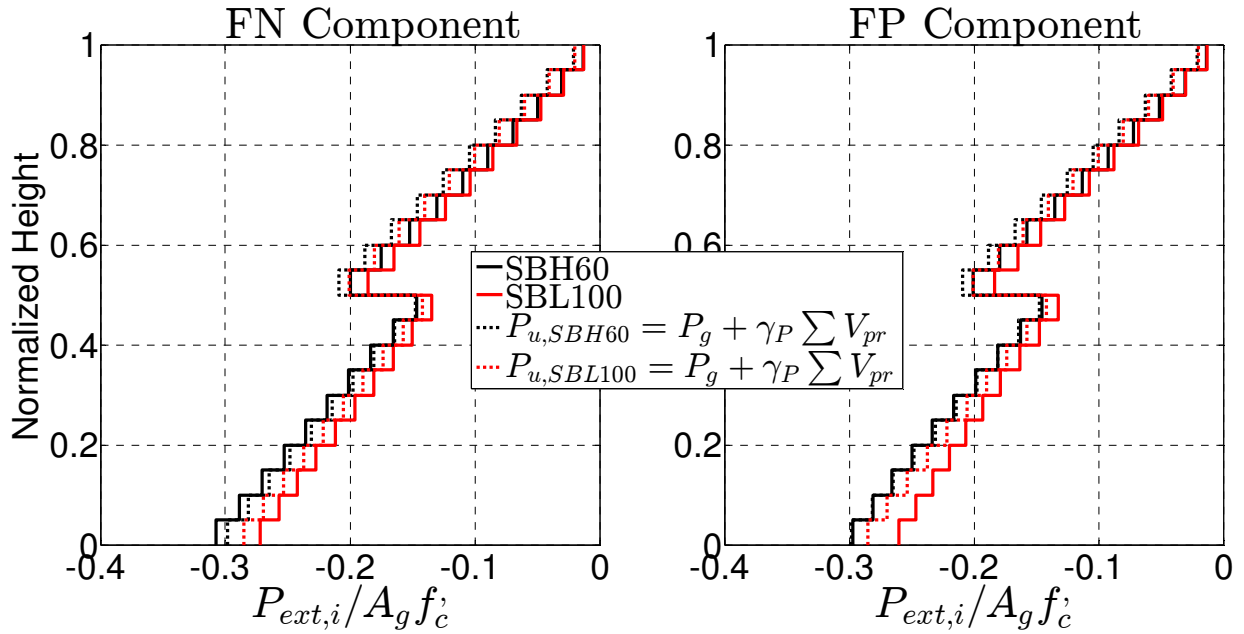
Figure 6.7.10: Exterior Column Compression in Frames SBH60 and SBL100
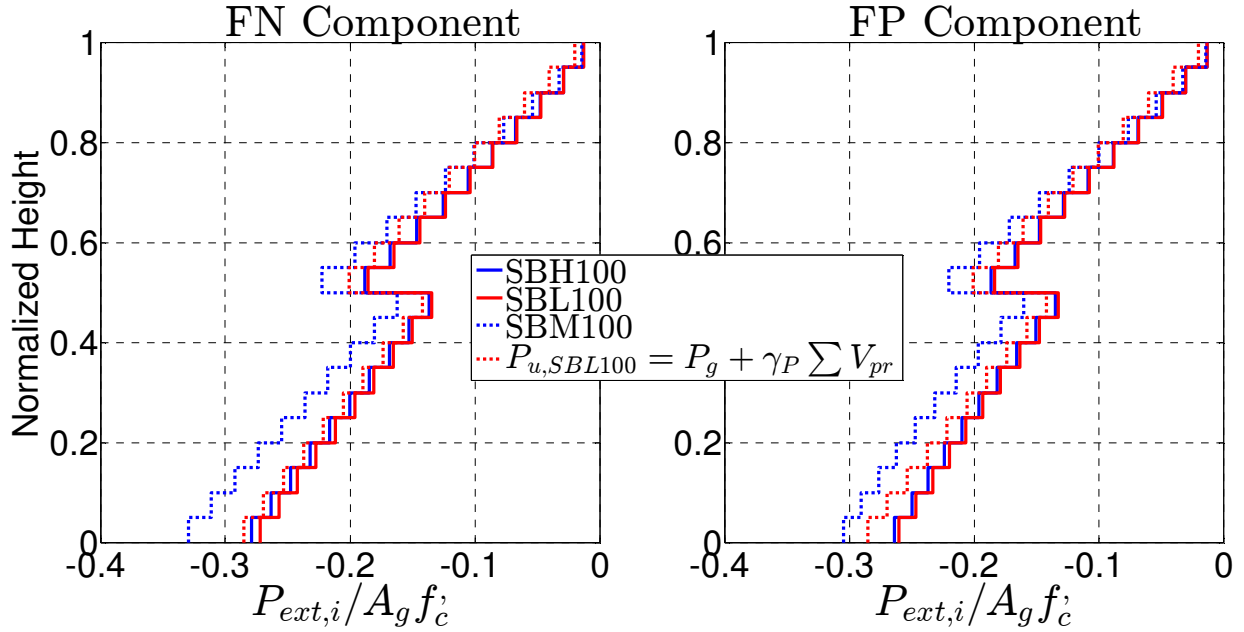
Figure 6.7.11: Exterior Column Compression in Frames SBH100, SBL100, and SBM100
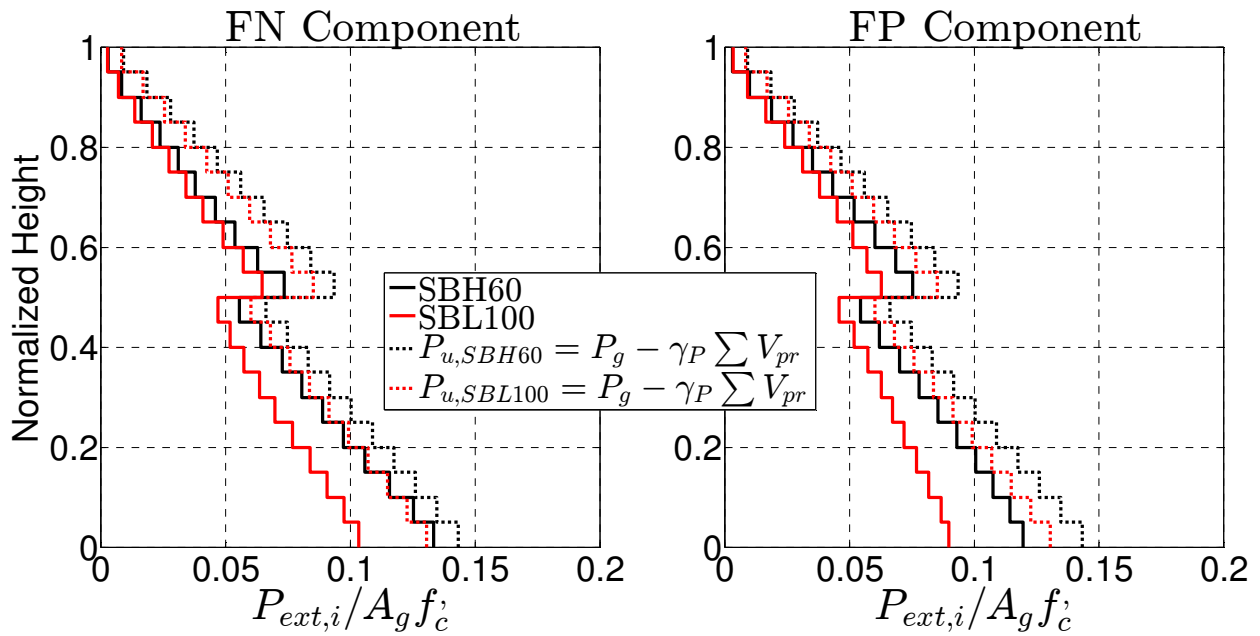
Figure 6.7.12: Exterior Column Tension in Frames SBH60 and SBL100
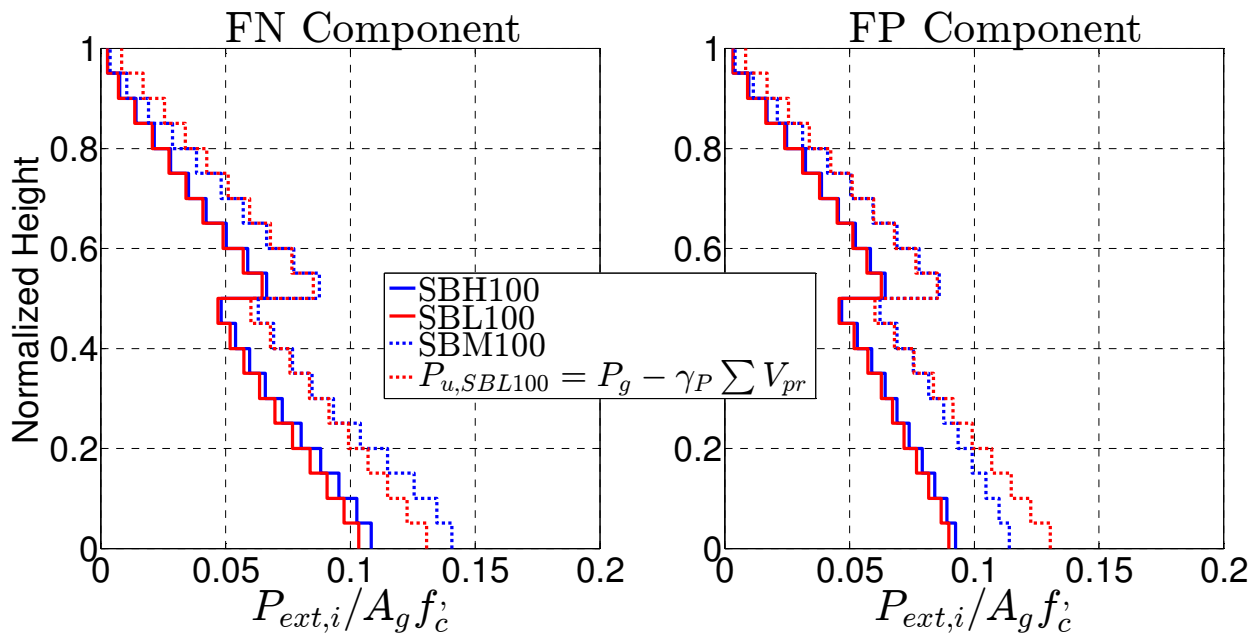
Figure 6.7.13: Exterior Column Tension in Frames SBH100, SBL100, and SBM100

Column shear: Estimation of column shear in design is challenging because the shear is occurring in columns of a frame in which the columns are designed to remain mainly in the linear range of response with primary yielding in the beams. It has been recognized that current methods for approximating design column shear in special moment frames do not always result in conservative estimate of shear forces that columns need to resist (Visnjic et al., 2014; Visnjic, 2014; Moehle, 2014; Moehle and Hooper, 2016). Underestimation of shear demand in columns could lead to column shear failure, which could cascade to more global response deficiencies, possibly including local or global collapse.

According to ACI 318-14, the column design shear force shall be calculated from considering the maximum forces that can be generated at the faces of the joints at each end of the column. These forces shall be calculated using the maximum probable moment strengths, $M_{pr,col}$, at each end of the column associated with the range of factored axial forces, P_u, acting on the column, that is, $V_{u,i} = \sum M_{pr,col,i}/l_{u,i}$. In tall buildings with large columns, this approach is known to result in large overestimation of column shears, and the transverse reinforcement required in some cases might be unfeasible to construct. Recognizing this, 318-14 allows that the column shears need not exceed those calculated from joint strengths based on $M_{pr,beam}$ of the beams framing into the joint. A widespread practice is to assume that the probable moment from the beams is resisted by equal column moments above and below the joint, resulting in column shear $V_{u,i} \approx \sum M_{pr,beam,i}/2l_{u,i}$. In the first story of buildings with fixed-base columns, one of the values in $\sum M_{pr,beam,i}$ is replaced by $M_{pr,col}$ at base of the building. A drawback of determining shears based on the beam moments is that the distribution of column moments above and below any beam-column joint is indeterminate. Studies (e.g., Kelly 1974) show that moment patterns can vary widely during seismic response. As a measure to avoid underestimating column design shear force when it is determined from the beam moments, ACI 318-14 also requires that the column design shear force shall be at least the shear from the controlling load combination determined by (linear) analysis of the structure. This latter provision seldom controls the column design.

Visnjic et al. (2014) and Moehle (2014) proposed that an improved estimate of column design shear can be obtained by amplifying the shear obtained from the linear analysis of the structure. The amplification factors consider system overstrength and dynamic effects. Based on this procedure, design column shears can be computed by:

$$V_u = \omega \Omega_0 V_{MRSA} \qquad \text{Eq. (10)}$$

where V_{MRSA} = column shear obtained from modal response spectrum analysis
$\quad$ ω = 1.3 as a dynamic amplification factor
$\quad$ Ω_0 = overstrength of the structural system, which can be approximated as
$$\Omega_0 = \frac{\sum M_{pr}}{\sum M_{u,MRSA}} \qquad \text{Eq. (11)}$$

$\sum M_{pr}$ = sum of probable moment strengths of all beam and column plastic hinges in a beam-yielding mechanism

$\sum M_{u,MRSA}$ = sum of the moments calculated from modal response spectrum analysis at all beam and column plastic hinge locations of the same beam-yielding mechanism in absence of gravity loads.

Column shear forces computed by these various approaches are plotted and compared against the average of the column shears from nonlinear dynamic analyses in Figure 6.7.14 and Figure 6.7.15. As expected, $V_{u,i} = \sum M_{pr,col,i}/l_{u,i}$ results in large overestimation of column shears in all cases. $V_{u,i} = \sum M_{pr,beam,i}/2l_{u,i}$ provides a reasonable central approximation of the shears, but underestimation or overestimation in individual stories appear to unacceptably large. The shear obtained from the controlling load combination determined by linear analysis of the structure V_{MRSA} is well below the shear obtained from nonlinear dynamic analysis, as is typically the case. The last approach of amplifying V_{MRSA} in accordance with Equation 11 produces the best overall estimate of shear in all exterior, interior, and middle columns. However, it is worth noting that shear in exterior columns of the first story is underestimated by this method as it does not account for the effects of beam elongation, which pushes the first-story columns outward, thereby increasing the first-story shear (Moehle 2014).

It can also be observed that the last method slightly overestimates shear in exterior columns for frames SBH100 and SBL100 as these frames are reinforced with higher-grade steel that has lower strain-hardening ratio than that of conventional Grade 60 A706. Hence, the overstrength factor of the structural system is overestimated for these two frames. Nevertheless, the method provides better agreement in shear forces in columns for frame SBM100.
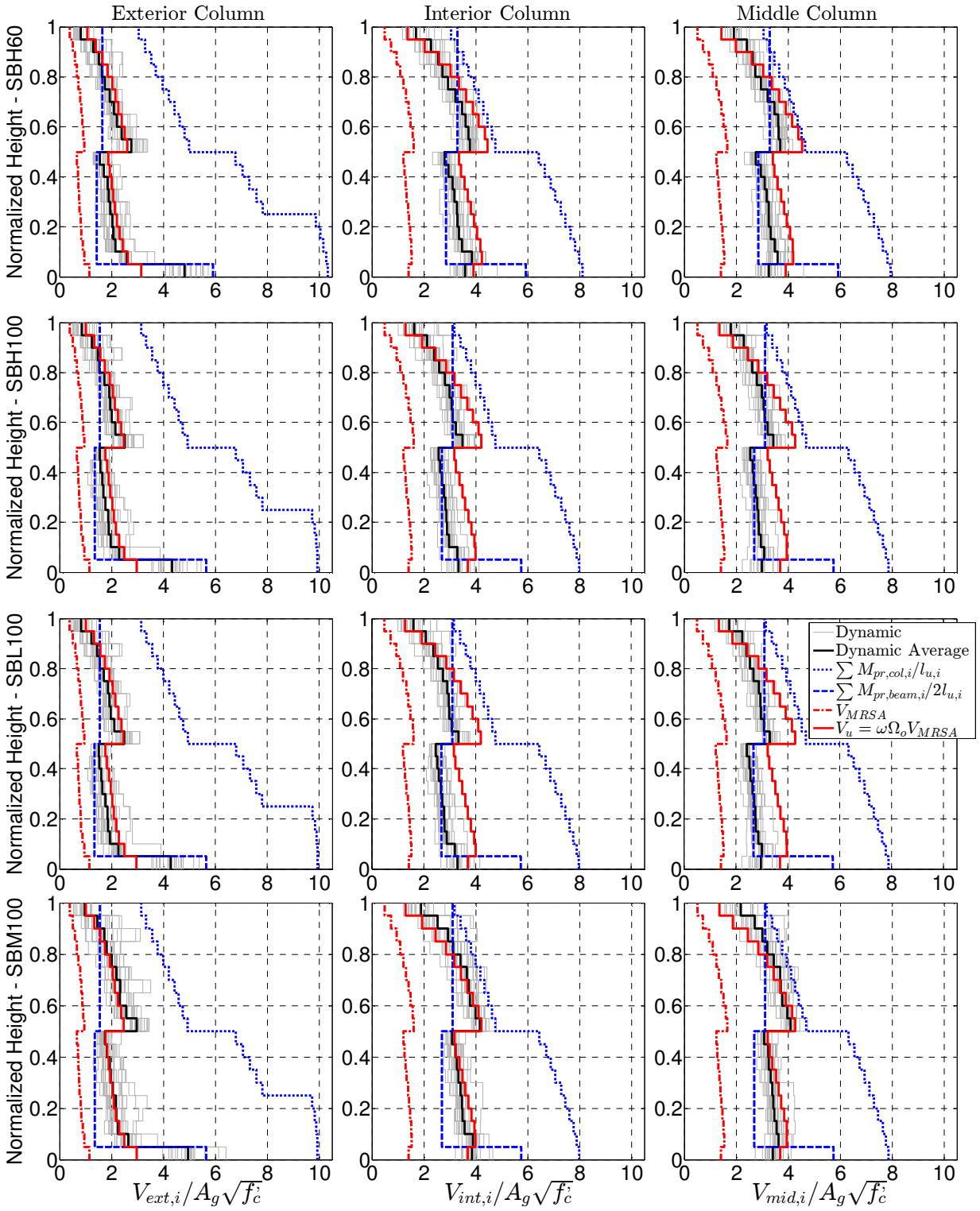
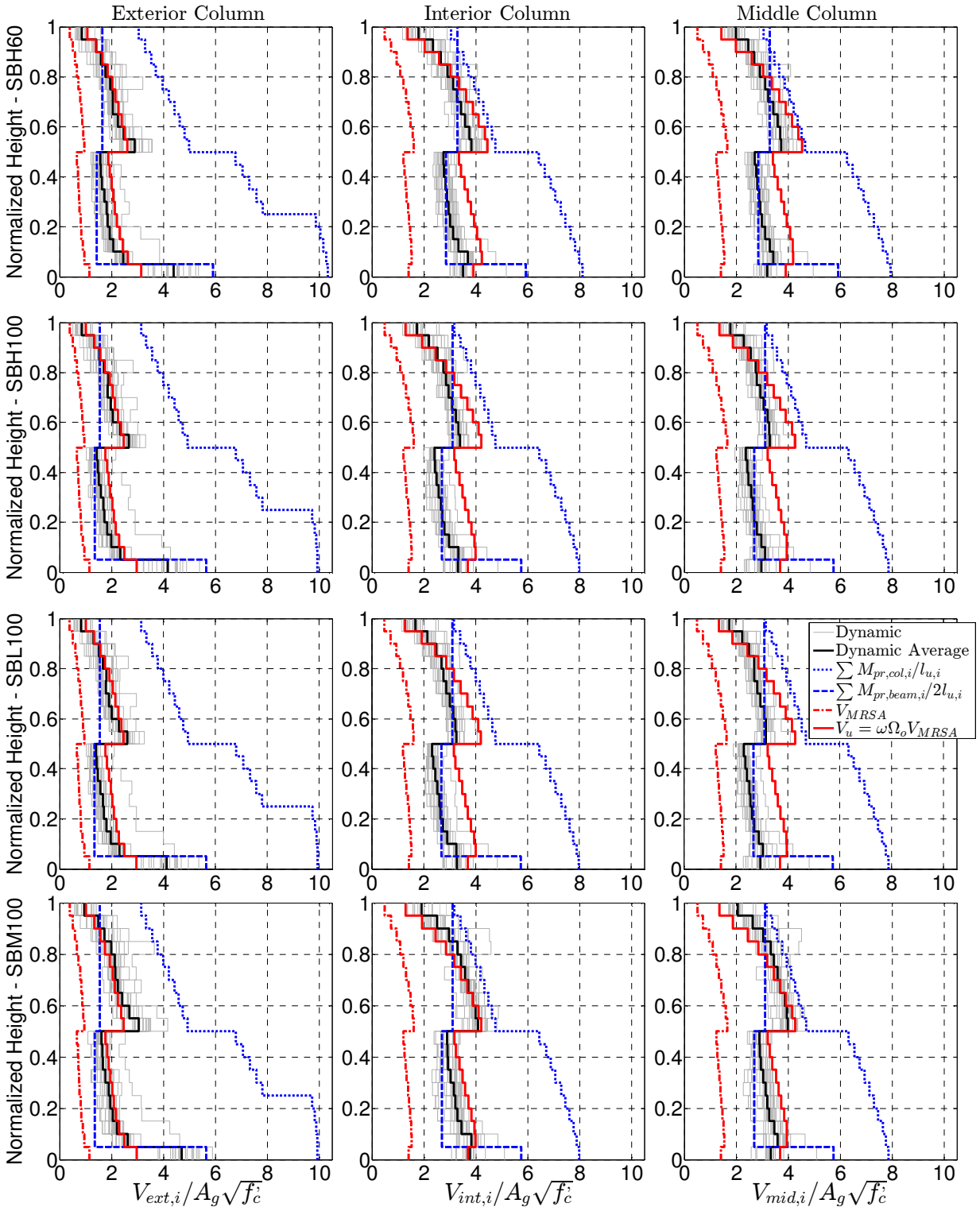Figure 6.7.14: Column Shear in All Frames – FN Component

Figure 6.7.15: Column Shear in All Frames – FP Component

7. SUMMARY AND CONCLUSION

The use of higher grade reinforcing steel has the potential benefit of reducing material quantities, thereby leading to reduced reinforcement congestion and reduced construction costs in reinforced concrete construction. Several steel mills in the United States can produce reinforcing steel of grade 100 (nominal yield strength of 100 ksi) and higher. However, at the time of this writing, none of these higher grades can match the benchmark mechanical properties of Grade 60 A706 steel. This raises questions about the performance characteristics of reinforced concrete construction that uses the higher-grade reinforcement.

A research program has been conducted at UC Berkeley in which four concrete beams were tested in a laboratory. Each beam was reinforced with a different type of reinforcement, including conventional Grade 60 A706, Grade 100 with T/Y = 1.18, Grade 100 with T/Y = 1.30, and Grade 100 A1035. The study investigated stiffness and strength, local bond stress-slip relationship of bars anchored in adjacent concrete sections, spread of plasticity, inelastic rotation capacity, and ultimate failure characteristics.

An analytical study using nonlinear dynamic analysis has also been carried out to investigate the seismic performance of tall reinforced concrete special moment resisting frames with high-strength reinforcement. Four 20-story concrete moment frames, three reinforced with Grade 100 steel and one with conventional Grade 60 steel, were designed in accordance with ASCE 7-16 and ACI 318-14 at a hypothetical site in San Francisco, California. All four frames had the same dimensions and concrete properties, resulting in identical design drifts. Frames with Grade 100 reinforcement were designed to have reduced amount of reinforcement providing equivalent nominal strength as the frame with Grade 60 reinforcement. Tests carried out as part of this study demonstrate that frames with higher-grade reinforcement had greater strain penetration, resulting in greater slip of reinforcement from connections. As a result of this, along with reduced reinforcement ratios, the frames with Grade 100 reinforcement were more flexible than the frame with Grade 60 reinforcement. In addition, many currently available types of Grade 100 reinforcement have lower tensile-to-yield strength ratio and lower uniform elongation compared with Grade 60. Less strain-hardening with higher-strength reinforcement increases strain localization and P-Delta effects. Seismic response of these frame buildings with Grade 100 reinforcement is studied and compared against that of buildings with Grade 60 reinforcement.

KEY FINDINGS:

Experimental Investigation:

1. All beams reinforced with Grade 100 steel achieved rotation capacity equivalent to that of a beam with conventional Grade 60 A706.

2. Laterally supporting all longitudinal bars at spacing of five (5) times the longitudinal bar diameter provided adequate resistance against bar buckling between hoop sets.

3. Beams SBL100 with Grade 100 T/Y = 1.18 and SBM100 with Grade 100 A1035 both failed by fracture of longitudinal reinforcement. Strain of longitudinal bars in SBL100 was most localized and concentrated at base of the beam, resulting in the highest strain under the same drift among all four specimens.

4. Beams SBH60 and SBH100 both failed by twisting of beam about longitudinal axis. This is also known as global instability. Strain in longitudinal bars did not reach the uniform elongation strain capacity.

5. Beams with Grade 100 reinforcement apparently sustained more slip of longitudinal bars out of the anchorage, resulting in more fixed-end rotation, and increasing total deformation capacity.

6. To maintain equivalent beam moment strength for all of the beams, the beams with Grade 100 reinforcement in this study had reduced longitudinal reinforcement ratio. This effect, combined with increased slip from the anchorage zone, reduced the effective stiffness of the beams with Grade 100 reinforcement compared with the beam with Grade 60 reinforcement.

7. Beam probable moment is affected by the amount of reinforcement material strain-hardening. Beams with lower T/Y had probable moment strength less than that calculated in accordance with ACI 318 procedures, while beams with higher T/Y ratio, especially the beam with ASTM A1035 reinforcement, had probable moment strength higher than that calculated in accordance with ACI 318 procedures.

Nonlinear Dynamic Analysis Study

1. Building frames SBH100, SBL100, and SBM100 with Grade 100 were less stiff than building frame SBH60 with conventional Grade 60 A706. This is because of reduced longitudinal reinforcement area and increased reinforcement slip from anchorages. In relation to this observation, it should be noted that the beam and column gross dimensions were selected to be identical regardless of the selected reinforcement. A widespread practice is to design moment frames such that gross dimensions are controlled by the building code drift limits. By that design practice, gross dimensions cannot be further reduced by using higher grade reinforcement.

2. Frames with higher-grade reinforcement sustained modestly greater drift than that of the frame with Grade 60 steel. SBM100 with Grade 100 A1035 that had round-shaped stress-strain relationship had the largest drift. SBH100 and SBL100 had similar drift despite the difference in reinforcement strain-hardening properties.

3. Story shear envelopes varied for the different frames that were studied. The frames with ASTM A706 Grade 60 reinforcement and ASTM A1035 reinforcement attracted somewhat higher shear, perhaps because of higher material strain-hardening, which increased the member moment strengths.

4. ACI 318-14 procedures for determining column design shear forces produced inconsistent results that, in some cases, were unconservative. An alternative procedure that produces improved estimates is proposed.

REFERENCE

ACI 318 (2014). *Building Code Requirements for Structural Concrete (ACI 318-14) and Commentary*, American Concrete Institute, Farmington Hills, MI.

ASCE 7 (2016). *Minimum Design Loads for Buildings and Other Structures*, American Society of Civil Engineers, Reston, VA.

Arteta, C.A. (2015). *Seismic Response Assessment of Thin Boundary Elements of Special Concrete Shear Walls*, Doctoral Dissertation, University of California, Berkeley, CA.

ASCE 41 (2013). *Seismic Rehabilitation of Existing Buildings, ASCE/SEI Standard 41-13*, American Society of Civil Engineers, Reston, VA

ASTM A1035 (2016). *Standard Specification of Deformed and Plain, Low-Carbon, Chromium, Steel Bars for Concrete Reinforcement*, ASTM International, 8 pp.

ASTM A370 (2014). *Standard Test Methods and Definitions for Mechanical Testing of Steel Products*, ASTM International, 50 pp.

ASTM C39 (2012). *Standard Test Method for Compressive Strength of Cylindrical Concrete Specimens*, ASTM International, 8 pp.

ASTM C469 (2010). *Standard Test Method for Static Modulus of Elasticity and Poisson's Ratio of Concrete in Compression*, ASTM International, 5 pp.

ASTM E8 (2016). *Standard Test Methods for Tension Testing of Metallic Materials,* ASTM International, 30 pp.

ATC 98 (2014). *Use of High-Strength Reinforcement in Earthquake-Resistant Concrete Structures*, ATC-98 Report, Applied Technology Council, Redwood City, California, 231 pp.

Berry, M.P., D.E. Lehman, and L.N. Lowes (2008). "Lumped-Plasticity Models for Performance Simulation of Bridge Columns," *ACI Structural Journal*, Vol. 105, No. 3, pp. 270-279.

Birely, A. C., Lowes, L. N., and Lehman, D. E. (2012). "Linear Analysis of Concrete Frames Considering Joint Flexibility," *ACI Structural Journal*, v. 109, no. 3, pp. 381-391.

Bournonville, M., J. Dahnke, and D. Darwin (2004). *Statistical Analysis of the Mechanical Properties and Weight of Reinforcing Bars*, SL Report 04-1, Structural Engineering and Material Laboratory, The University of Kansas, Lawrence, KS, 198 pp.

Chang, G. and Mander, J. (1994). *Seismic Energy Based Fatigue Damage Analysis of Bridge Columns: Part I – Evaluation of Seismic Capacity*, NCEER Technical Report 94-006.

Chopra A.K., and McKenna F., (2016). "Modeling Viscous Damping in Nonlinear Response History Analysis of Buildings for Earthquake Excitation," *Earthquake Engineering and Structural Dynamics*, 45:193-211.

Chu, T.C., W.F. Ranson, M.A. Sutton, and W.H. Peters (1985). "Applications of Digital-Image-Correlation Techniques to Experimental Mechanics," *Experimental Mechanics*, 25(3), 232-244.

Elwood, K.J., and M.O. Eberhard (2009). "Effective Stiffness of Reinforced Concrete Columns," *ACI Structural Journal*, Vol. 106, No. 4, pp. 476-484.

FEMA 461 (2007). *Interim Testing Protocols for Determining the Seismic Performance Characteristics of Structural and Nonstructural Components*, Federal Emergency Management Agency, Washington, D.C., 138 pp.

Filippou, F.C., Popov, E.P., Bertero, V.V. (1983). *Effects of Bond Deterioration on Hysteretic Behavior of Reinforced Concrete Joints*, Report EERC 83-10, Earthquake Engineering Research Center, University of California, Berkeley.

Ghannoum, W. (2007). *Experimental and Analytical Dynamic Collapse Study of a Reinfroced Concrete Frame with Light Transverse Reinforcement*, Doctoral Dissertation, University of California, Berkeley, CA.

Haselton, C.B., Goulet, C.A., Mitrani-Reiser, J., Beck, J.L., Deierlein, G.G., Porter, K.A., Stewart, J.P., and Taciroglu, E. (2008). *An Assessment to Benchmark the Seismic Performance of a Code-Conforming Reinforced Concrete Moment-Frame Buildings*, Technical Report Peer 2007/2012, Pacific Earthquake Engineering Research Center, Berkeley, CA.

Hognestad, E. (1951*). A Study of Combined Bending and Axial Load in Reinforced Concrete Members*, Bulletin 399, University of Illinois Engineering Experiment Station, Urbana, Ill., 128 pp.

Ibarra L.F., Medina R.A., and Krawinkler H. (2005). "Hysteretic Models That Incorporate Strength and Stiffness Deterioration," *Earthquake Engineering and Structural Dynamics*, 34(12), 1489-1511.

Jayaram, N., Lin, T., and Baker, J. W. (2011). "A computationally efficient ground-motion selection algorithm for matching a target response spectrum mean and variance." *Earthquake Spectra*, 27(3), 797-815.

Kelly, T. (1974). *Some Seismic Design Aspects of Multistorey Concrete Frames*, Master of Engineering Report, University of Canterbury, Christchurch, New Zealand, 163 pp.

Kunnath, S., Heo, Y., and Mohle, L. (2009). "Nonlinear Uniaxial Material Model for Reinforcing Steel Bars," *Journal of Structural Engineering*, 135(4): 335-343

LATBSDC (2014). *An Alternative Procedure for Seismic Analysis and Design of Tall Buildings Located in the Los Angeles Region*, Los Angeles Tall Building Structural Design Council, Los Angeles, Ca.

Lehman, D.E., and Moehle, J.P. (2000). *Seismic Performance of Well-Confined Concrete Columns*, UCB/PEER 1998/01, Pacific Earthquake Engineering Research Center, Berkeley, California.

Ma, S-Y.M., V.V. Bertero, and E.P. Popov (1976). *Experimental and Analytical Studies on Hysteretic Behavior of Reinforced Concrete Rectangular and T-Beams*, Report No. UCB/EERC 76/2, University of California, Berkeley, CA, 241 pp.

Mander, J.B., M.J.N. Priestley, and R. Park (1984). *Seismic Design of Bridge Piers*, Report 84-02, Department of Civil Engineering, University of Canterbury, Christchurch, New Zealand.

Mander, J.B., Priestley, M.J.N., and Park, R. (1988a). "Theoretical Stress-Strain Model for Confined Concrete," *Journal of Structural Engineering*, Vol. 114, No. 8, pp. 1804-1826

Mander, J.B., Priestley, M.J.N., and Park, R. (1988b). "Observed Stress-Strain Behavior of Confined Concrete," *Journal of Structural Engineering*, Vol. 114, No. 8, pp. 1827-1849

McKenna, F., Fenves, G.L., Scott, M.H., and Jeremic, B., 2000. Open System for Earthquake Engineering Simulation (OpenSees) [software]. Pacific Earthquake Engineering Research Center, University of California, Berkeley, CA. http://opensees.berkeley.edu

Moehle, J.P., and J.D. Hooper (2016). *Seismic Design of Reinforced Concrete Special Moment Frames: A Guide for Practicing Engineers, Second Edition*, NEHRP Seismic Design Technical Brief No. 1, NIST GCR 16-917-40, National Institute of Standards and Technology, Gaithersburg, MD.

Moehle, J. P. (2014). Seismic Design of Reinforced Concrete Buildings, Mc Graw-Hill Education, New York, 760 pp.

Neuenhofer, A., and Filippou, F.C. (1997). "Evaluation of Nonlinear Frame Finite-Element Models." *Journal of Structural Engineering*, 123(7), 958-966

Open System for Earthquake Engineering Simulation (OpenSees) 2012-2014. http://opensees.berkeley.edu/.

PEER 2014, Ground Motion Database. http://peer.berkeley.edu/ngawest2/databases/

Priestley, M.J.N., and R. Park (1987). "Strength and Ductility of Concrete Bridge Columns under Seismic Loading," *ACI Structural Journal*, Vol. 84, No. 1, pp. 61-76.

Ramberg, W., and W.R. Osgood (1943). *Description of Stress-Strain Curves by Three Parameter*, Technical Note No. 902, National Advisory Committee for Aeronautics, Washington DC.

Rautenberg, J.M., S. Pujol, H. Tavallali, and A. Lepage (2013). "Drift Capacity of Concrete Columns Reinforced with High-Strength Steel," *ACI Structural Journal*, Vol. 110, No. 2, pp. 307-317.

Razvi, S., and M. Saatcioglu (1999). "Confinement Model for High-Strength Concrete," *Journal of Structural Engineering*, Vol. 125, No. 3, pp. 281-289.

Scott, M.H., and Fenves G. 2006. "Plastic Hinge Integration Methods for Force-Based Beam-Column Elements," *Journal of Structural Engineering*, 132(2): 244-252

Sokoli, D., A. Limantono, and W. M. Ghannoum (2017). *Defining Structurally Acceptable Properties of High-Strength Steel Bars through Material and Column Testing - Part II: Column Testing Report*, Research Grant Agreement #05-14, Charles Pankow Foundation, Vancouver, WA, 219 pp.

TBI (2016). *Seimic Design Guidelines for Tall Buildings*, Report No. 2016/09, Pacific Earthquake Engineering Research Center, University of California, Berkeley, CA, 140 pp.

Visnjic, T. (2014). *Design Considerations for Earthquake-Resistant Reinforced Concrete Special Moment Frames*, Doctoral Dissertation, University of California, Berkeley, CA.

Visnjic, T., M. Panagiotou, and J.P. Moehle (2014). "Seismic Response of 20-Story Tall Reinforced Concrete Special Moment Resisting Frames Designed with Current Code Provisions," *Earthquake Spectra*, doi: http://dx.doi.org/10.1193/082112EQS267M.

XTRACT (2009). XTRACT, version 3.0.8. TRC/Imbsen Software Systems, http://www.imbsen.com/xtract.htm.

Zhao, J., and S. Sritharan (2007). "Modeling of Strain penetration Effects in Fiber-Based Analysis of Reinforced Concrete Structures," *ACI Structural Journal*, 104(2), pp. 133-141.

APPENDIX A. DESCRIPTION OF LABORATORY TESTS

CONSTRUCTION OF TEST SPECIMENS

All specimen formworks were laid down horizontally on the lab floor during construction (Figure A-2). Reinforcement cages were fabricated on the side and placed onto the form by crane. Concrete was cast into forms using a pump truck. Cast specimens were then covered by wet burlaps and plastic sheets. Concrete cylinders were also made from the same concrete at the same time that specimen casting was done. These concrete cylinders were covered with plastic sheet and later tested for representative concrete strength of test specimens.

Actual dimensions of test specimens are described and summarized in Figure A-3 and Table A-1, respectively. Actual material properties including concrete and reinforcing steel are presented in Material section.
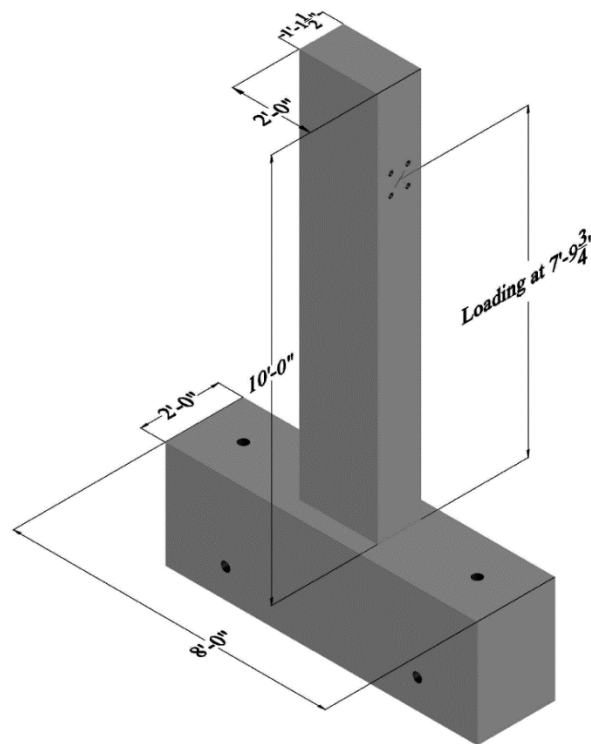
Figure A-1: Geometry and Dimensions of Test Beam Designs
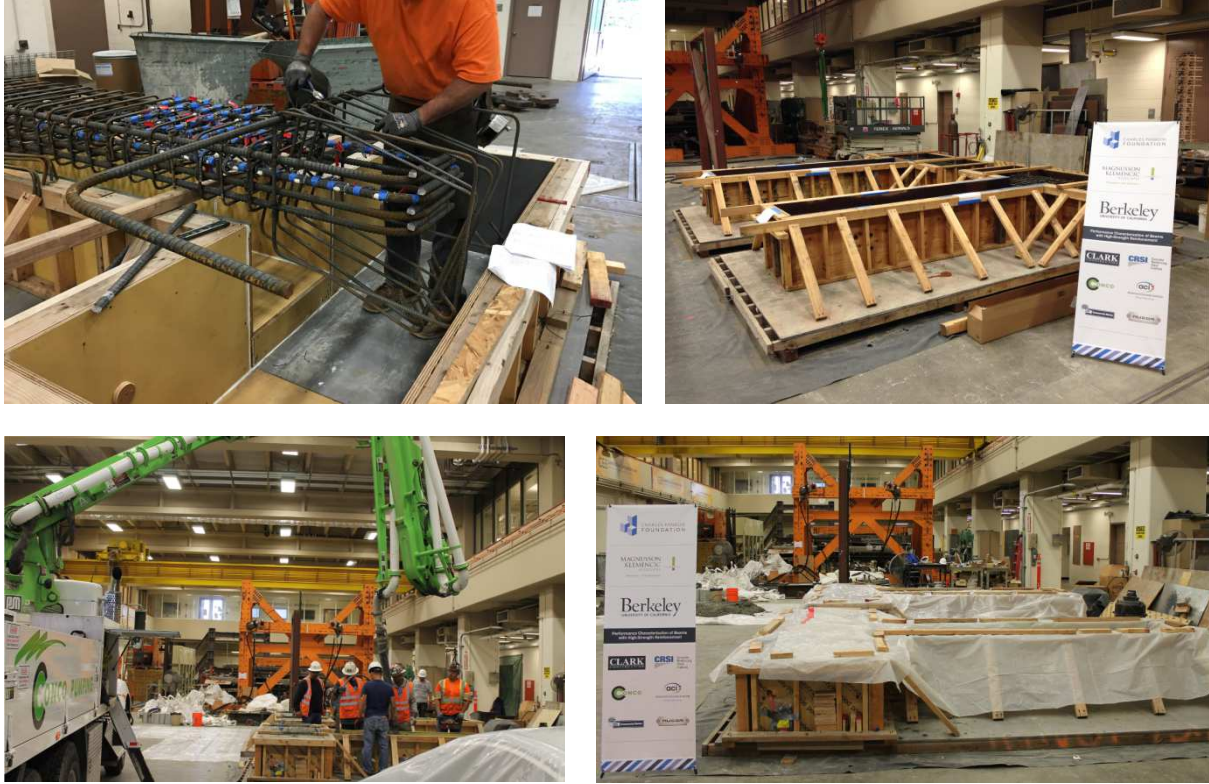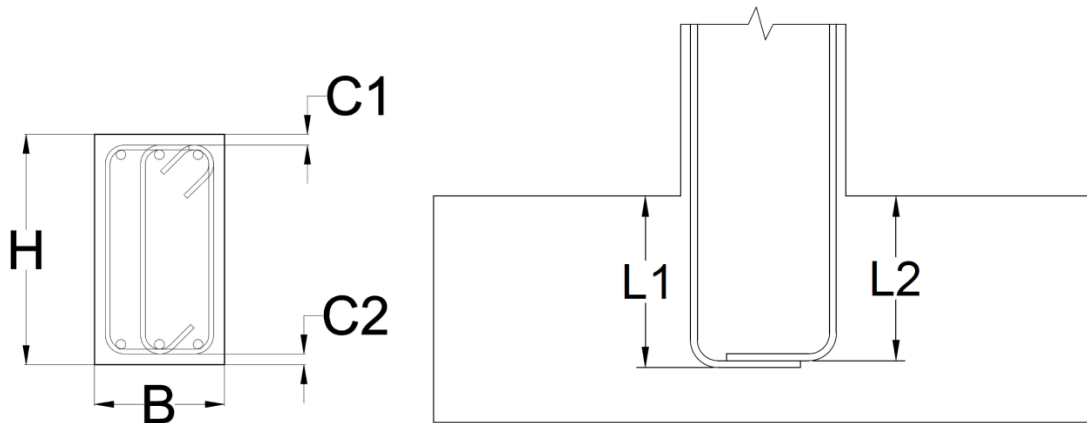
Figure A-2: Construction of Test Specimens

Figure A-3: Typical Dimensions of Test Specimens

Table A-1: Actual Measured Dimensions of Test Specimens

	SBL100	SBH100	SBM100	SBH60
H (in)	24	24.125	24.25	24
B (in)	13.5	13.5	13.5	13.5
C1 (in)	1.5	1.375	1.25	1.0
C2 (in)	1.5	1.375	1.25	1.5
L1 (in)	24	24.75	25	24
L2 (in)	23.5	23.75	24	23

MATERIALS

Concrete

Normal-weight concrete with specified compressive strength of 5 ksi and six-inch slump was used for all beam specimens and their foundation blocks. Materials used in mix design are presented in Table A-2.

Table A-2: Concrete Mix Design Materials

Material	Description	Design Quantity	Actual Quantity*
Cement	ASTM C150	547 lbs/yd^3	548 lbs/yd^3
Coarse Aggregate	ASTM C33 #67	1675 lbs/yd^3	1662 lbs/yd^3
Fine Aggregate	ASTM C33	1424 lbs/yd^3	1393 lbs/yd^3
Fly Ash	ASTM C618 Class F	97 lbs/yd^3	98 lbs/yd^3
Water	ASTM C1602	34 gals/yd^3	31 gals/yd^3

*: Actual quantities were taken from concrete batch cast for specimens in 2nd phase. These quantities varied slightly for specimens in 1st phase.

Plastic cylinders with six-inch diameter and twelve-inch height were used to prepare concrete cylinders during casting. These cylinders were covered by plastic sheets to keep the same curing conditions as concrete in beam specimens. They were then tested for compressive strength at 7, 14, 21, 28 days, and day of beam testing.

All concrete cylinders were removed from plastic molds and capped at both ends with sulfur-capping compound prior to compression test to minimize stress concentration, and ensure uniform loading. The loading procedure had two phases. In the first phase, which was intended to determine modulus of elasticity of concrete following ASTM C469/C469M-10 standards, cylinders were compressed to approximately 40% of the crushing load, which was estimated by testing one sacrificial sample to failure. The loading rate was about 25 kips per minute for this phase. The cylinders were then unloaded close to zero, and reloaded in compression again until a slight drop or plateau of load resistance was observed, indicating initiation of crushing of concrete cylinders. The second phase of testing to determine compressive strength was performed per ASTM C39/C39M-12 standards, and the loading rate was approximately 60 kips per minute. Figure A-4 displays typical concrete stress-strain curves. A summary of concrete strength and moduli is presented in Table A-3.
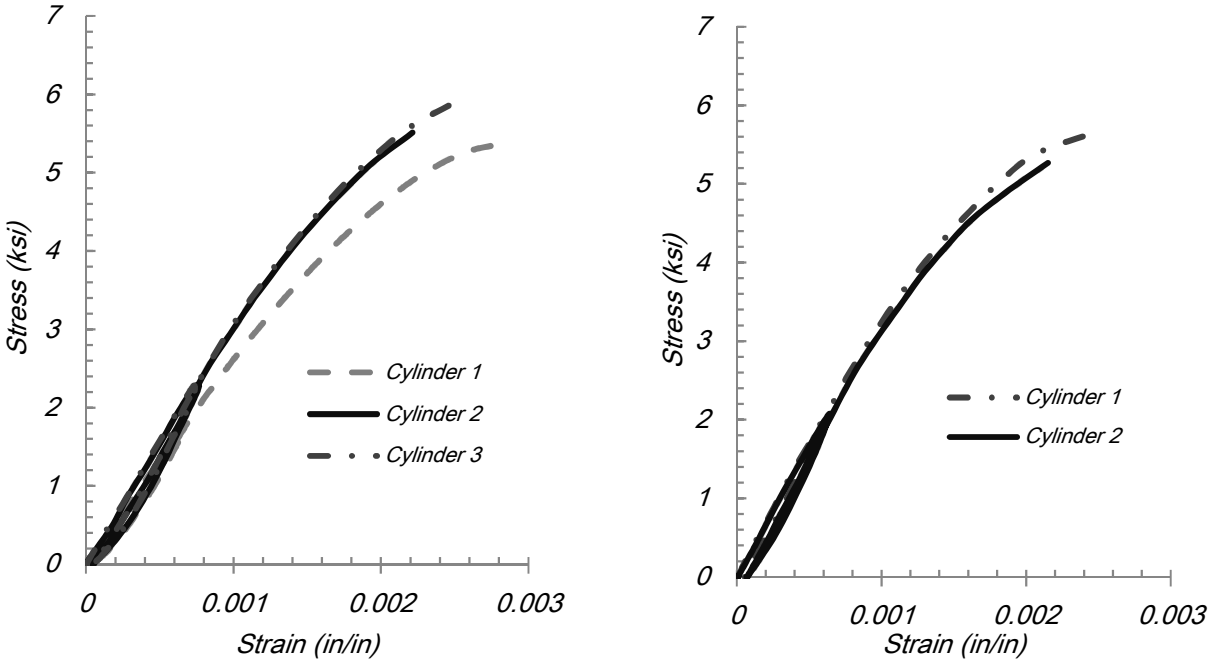
Figure A-4: Compressive Stress-Strain Relationships of Concrete Cylinders: Left – Test Day of SBH60 Beam; and Right – Test Day of SHM100 Beam

Table A-3: Summary of Compressive Strength of Concrete Cylinders

		Cylinder 1	**Cylinder 2**	**Cylinder 3**	**Average**	**Modulus**
SBL100	7 days	2.74	2.74	2.71	2.73	
	14 days	3.33	3.44	3.32	3.36	
	21 days	3.60	3.49	3.58	3.56	
	28 days	3.61	3.65	3.92	3.73	
	Day of test	5.06	5.09	5.16	5.10	NA
SBH100	7 days	2.74	2.74	2.71	2.73	
	14 days	3.33	3.44	3.32	3.36	
	21 days	3.60	3.49	3.58	3.56	
	28 days	3.61	3.65	3.92	3.73	
	Day of test	4.91	5.00	5.10	5.00	NA
SBM100	7 days	3.87	4.04	3.96	3.96	
	14 days	4.79	5.05	4.90	4.91	
	21 days	5.22	5.01	5.01	5.08	
	28 days	5.23	5.11	5.34	5.24	
	Day of test	5.31	5.51	5.60	5.47	3500
SBH60	7 days	4.13	4.10	4.12	4.12	
	14 days	5.08	4.89	4.94	4.77	
	21 days	5.46	5.26	5.30	5.34	
	28 days	5.26	5.36	5.63	5.41	
	Day of test	5.87	5.69	5.42	5.66	3200

Note: All units are in ksi.

99

Reinforcing Steel

Four test beams in research program were reinforced with four different types of steel reinforcement (Figure A-5). Steel bars used in Beam SBL100 were Grade 100 produced by quenching and tempering, while those in Beam SBH100 were also of the same grade and manufactured mainly through micro-alloying. Reinforcement in Beam SBM100 was classified as Grade 100 as well with properties satisfying ASTM A1035 specifications. This type of steel was a low-carbon steel and produced under controlled-rolling process. The last beam specimen was reinforced with conventional Grade 60 ASTM A706 steel.

Coupon specimens were taken from the same batch of longitudinal reinforcement used in each test beam and tested under monotonic loading in tension to determine mechanical properties. These monotonic tension tests were conducted following ASTM A370 standards. Important mechanical properties of reinforcing steel were determined by methods specified in ASTM E8/E8M.

Figure A-6 shows a typical stress-strain relation of one No. 8 Grade 100 used in Beam SBH100 obtained from monotonic test with 8-inch gauge length. Yield stress was obtained by the 0.2% offset method (Figure A-7). This method was also applied to find yield stress of Grade 100 steel bars used in Beam SBM100 that had no distinct yield plateau in stress-strain relation. Onset and slope of strain-hardening were determined graphically on stress-strain curve (Figure A-7). By observation, x-coordinate of the blue line defined strain at onset of strain-hardening. Meanwhile, slope of the red line was calibrated such that it represented the slope of strain-hardening. Uniform elongation was determined by taking the average of strains, at which stress was 0.5% of the magnitude of the peak stress value (Figure A-8).

Figure A-9 displays typical stress-strain relations of all longitudinal reinforcement used in all beam specimens. And Table A-4 presents their important mechanical properties.

Figure A-5: Longitudinal Steel Used in Test Specimens - Left to Right: SBL100, SBH100, SBM100, SBH60
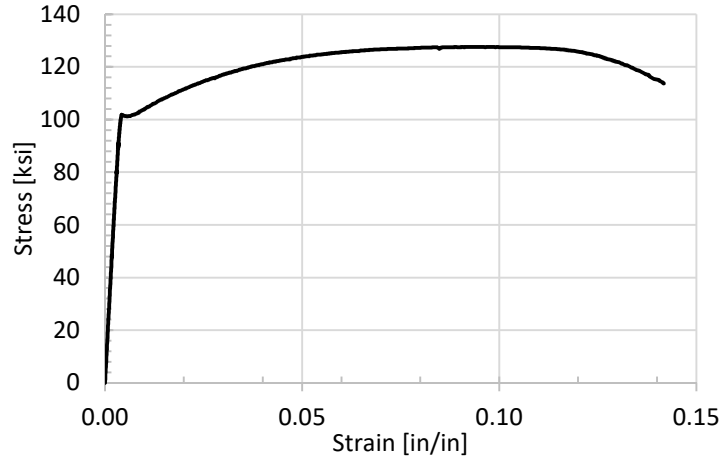
Figure A-6: Typical Stress-Strain Relationship of No. 8 Grade 100 in Beam SBH10
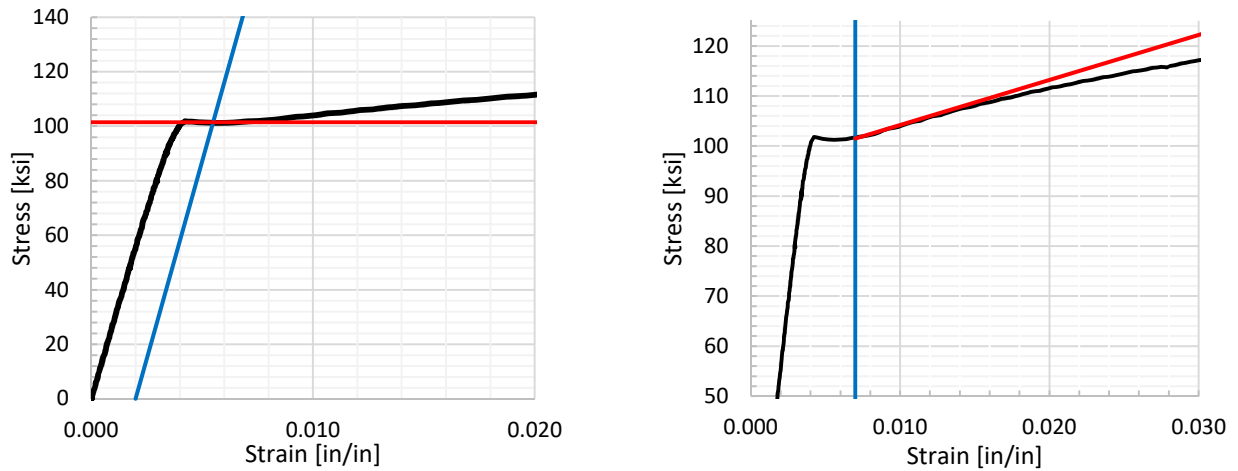
Figure A-7: Left: Yield Strength Determination by 0.2%-Offset Method; Right: Onset and Slope of Strain-Hardening
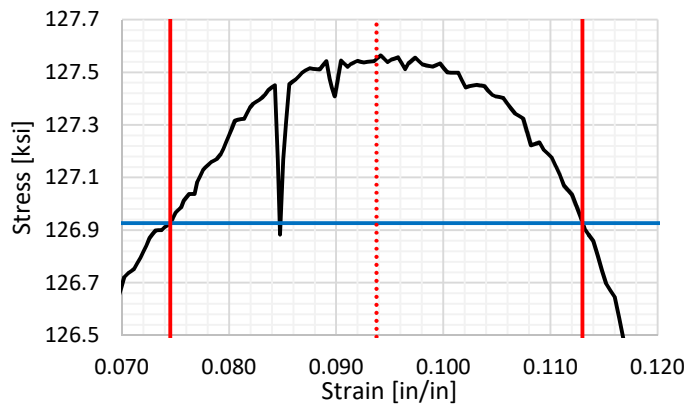
Figure A-8: Determination of Uniform Elongation by Plateau within 0.5% of Magnitude of Peak Force
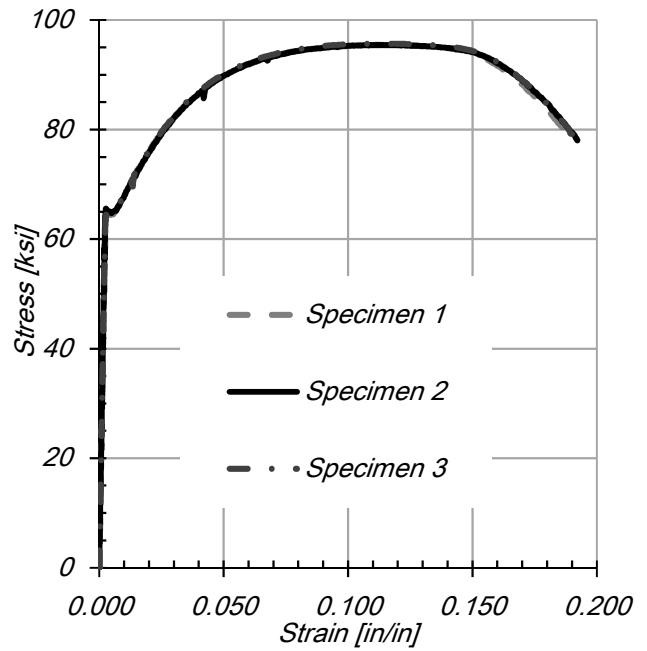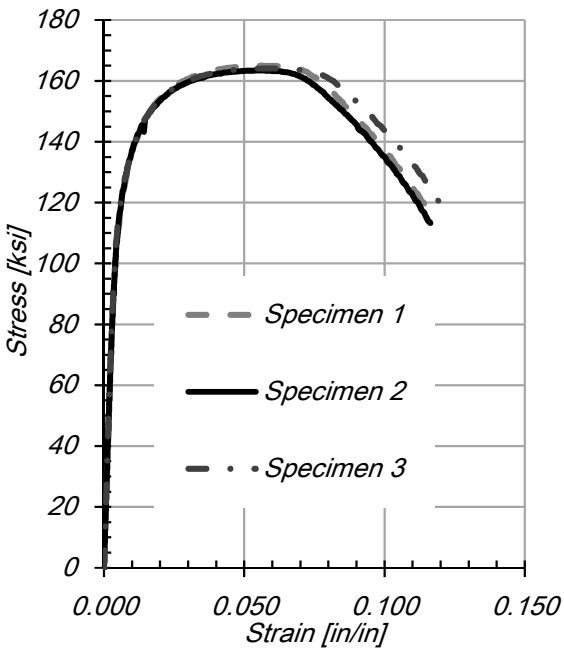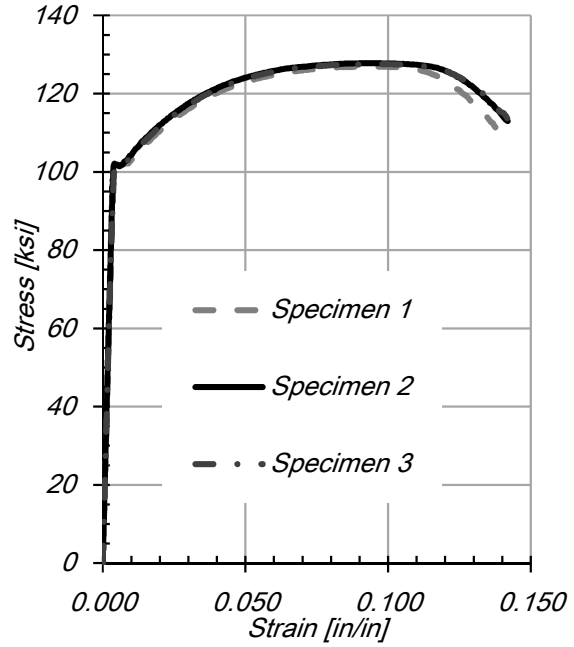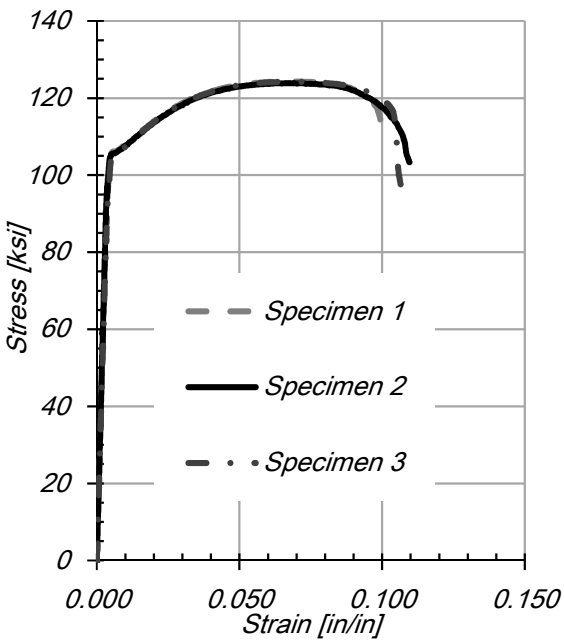
Figure A-9: Tension Stress-Strain relationship of Steel Coupon Tests: Top Left: No. 8 Bars Used in Beam SBL100; Top Right: No. 8 Bars Used in Beam SBH100; Bottom Left: No. 8 Bars Used in Beam SBM100; Bottom Right: No. 9 Bars Used in Beam SBH60

Table A-4: Mechanical Properties of Longitudinal Reinforcement

Specimen	Yield Strength (ksi)	Tensile Strength (ksi)	Tensile-to-Yield Strength Ratio (T/Y)	Strain at Onset of Strain-Hardening (%)	Slope of Strain-Hardening (ksi)	Uniform Elongation (%)
SBL100	106.0	123.9	1.17	0.7	600	6.8
SBH100	101.5	127.6	1.26	0.7	900	9.4
SBM100	120.0	165.0	1.38	0.6	4500	5.6
SBH60	64.5	95.5	1.48	0.6	950	11.4

TEST INSTRUMENTATION AND DATA ACQUISITION SYSTEMS

Interior (Strain gauges)

Strain gauges were installed onto reinforcing bars as interior instrumentation. Typical locations of these strain gauges are shown in Figure A-10. These strain gauges were installed to measure strain primarily along middle longitudinal bars on both sides of beam, hoops and crossties, and along anchorage length of middle longitudinal bars.

Strain gauges used were Tokyo Measuring Instruments Laboratory Co., Ltd. Model YLFA-5-5LT. These gauges are designed for measurements of large strains up to 15-20%. All gauges were 0.2-in. long and 0.08-in. wide. Detailed information can be found on manufacturer's website (www.tml.jp). To attach the strain gauges to the rebar, the rebar was smoothed, prepped with an acid, base, and alcohol, and then the gauges were glued to the bar with CN-Y adhesive. After the glue had cured, gauges were coated with wax, SB tape, and epoxy to protect them during casting. Care was taken to ensure these layered materials took up as little area as possible at each location on the surface of the bar. SB tape and CN-Y adhesive are manufactured by Tokyo Measuring Instruments Laboratory Co., Ltd.

Exterior (Displacement transducers)

Exterior instrumentation included displacement transducers set up to measure global deflection and local deformations along test specimen length (Figure A-12).

String potentiometers used to measure global displacements were Celesco Model PT 101-0015-111-110 (Figure A-11). Detailed information can be found website (www.stringpots.ca). In all cases, sensors with a 15-in. stroke length were used. In cases where sensors had to be placed more than 15 in. from the point on the specimen they measured, thin braided-steel wires were used to extend from the point of placement to the point of measurement. This was done because accuracy is related to stroke length, so it was undesirable to use instruments with greater extension capacity.

Linearly Varying Displacement Transducers (LVDTs) were attached onto the specimen at various locations to measure local deformations (flexural, shear, and dilation deformations), longitudinal bar buckling, slip, beam base sliding relative to concrete foundation, and beam elongation. Linear transducers used to measure both local and global displacements were Novotechnik Models TRS-0025, TRS-0050, and TRS-0100 (Figure A-11). Detailed information can be found on http://www.novotechnik.com. In the case of local displacements, instruments were affixed near the surface of each beam using eyelets on threaded rods that allowed them to rotate without distorting their line of measurement. Where the instrument bore on a concrete surface, a thin sheet of metal was epoxied to the concrete to prevent distortion due to the uneven surface.
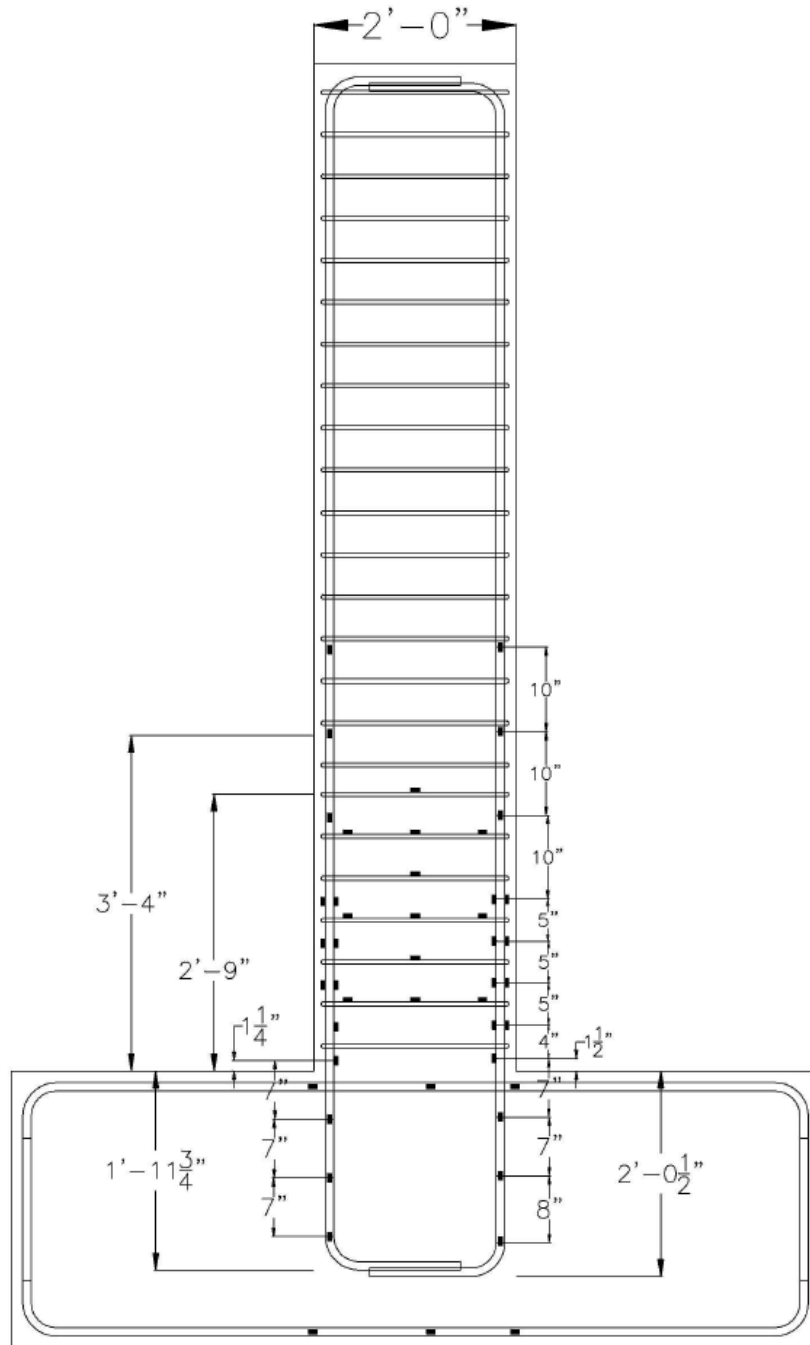
Figure A-10: Interior Instrumentation – Strain Gauges

Figure A-11: Typical Displacement Transducers Used in Tests. Left: String Potentiometer for Global Deflection Measurement; Right: Novotechnik Used to Measure Local Deformations
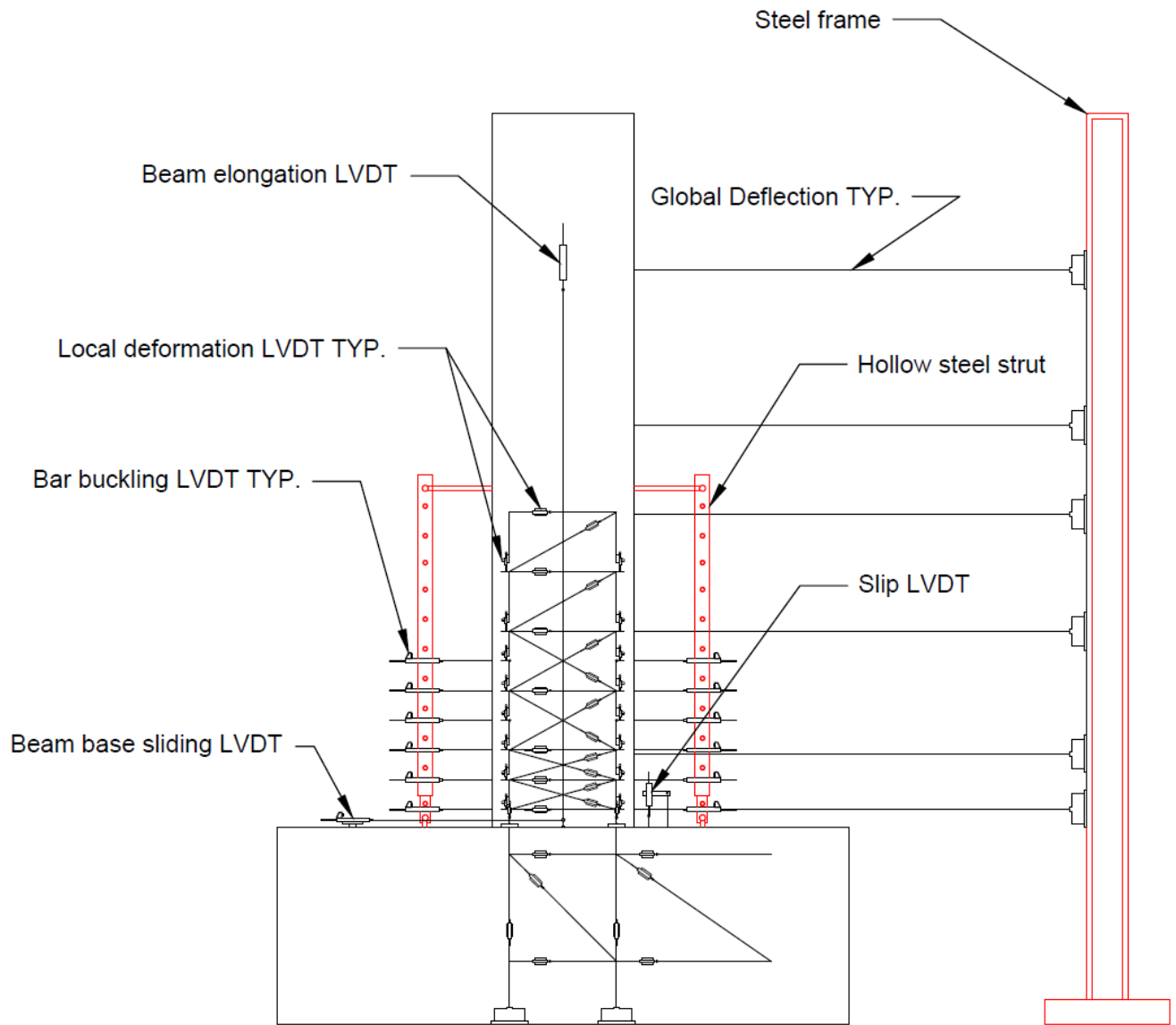

Figure A-12: Schematic Drawing of Exterior Instrumentations

Instrumentation for measuring slip of reinforcement:

As shown in Figure A-12, Figure A-20, & Figure A-21, slip of longitudinal reinforcement out of anchorage is measured by two LVDTs that are connected to two threaded rods attached to reinforcement at base of beams. These two threaded steel rods are brass-brazed onto the reinforcement. The brass-brazing procedure is described as followings:

1. At the location of interest (base of beam), the longitudinal reinforcement is surface cleaned by steel-wire brush (Figure A-13).
2. Heating chemical is applied on the cleaned surface of reinforcement and threaded rod (Figure A-15).
3. Both cleaned surface of reinforcement and threaded rod are heated up to approximately 900-degree Fahrenheit using a torch (Figure A-16). At the same time, a thin rod of brass material is also heated under the same torch and melted.
4. Threaded rod is brought into contact with reinforcement and melted brass material is applied in between to bond the threaded rod onto reinforcement.
5. Heat is removed and a strong connection between threaded rod and reinforcement is formed as melted brass material cools off (Figure A-17).
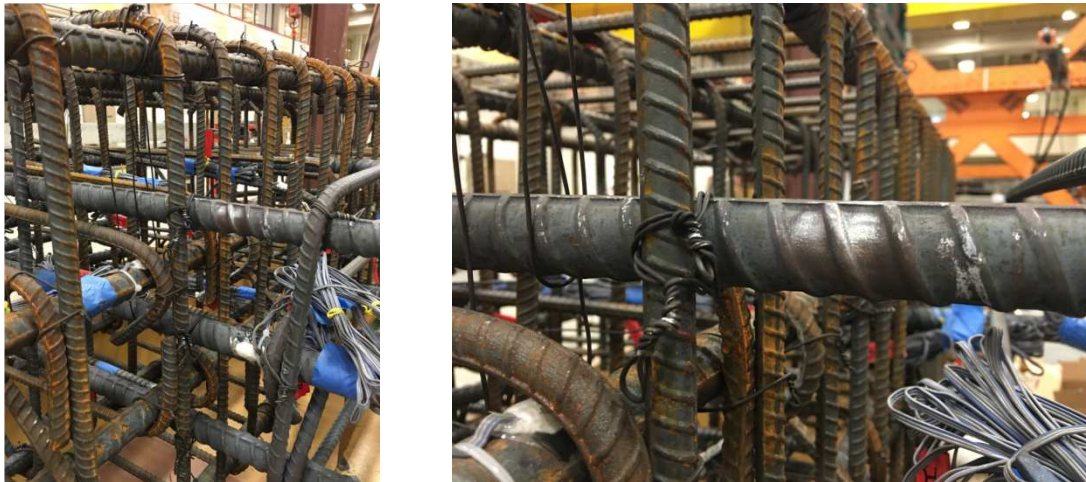
Figure A-13: Brass-Brazing Procedure - Step 1: Surface Clean
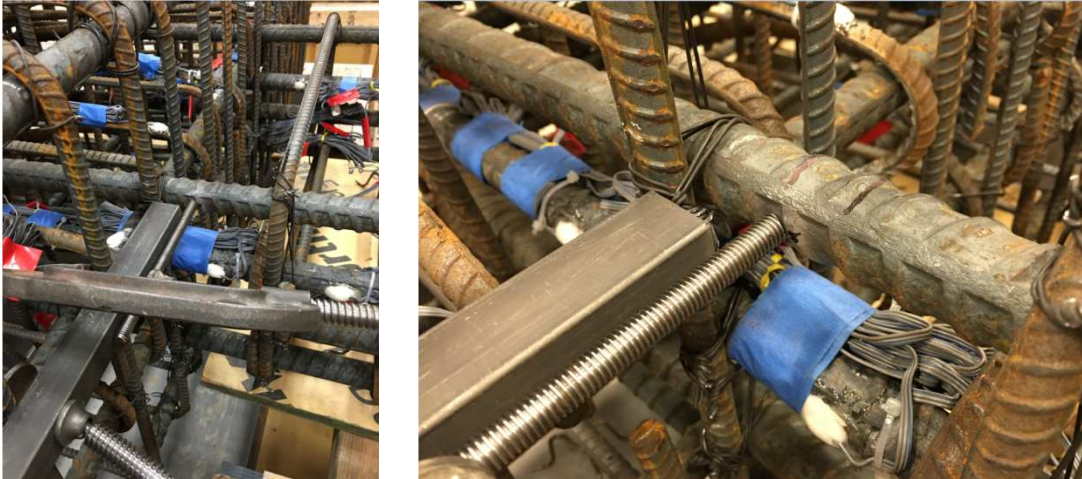
Figure A-14: Brass-Brazing Procedure - Placement of Threaded Rod

Figure A-15: Brass-Brazing Procedure - Step 2: Application of Heating Chemical
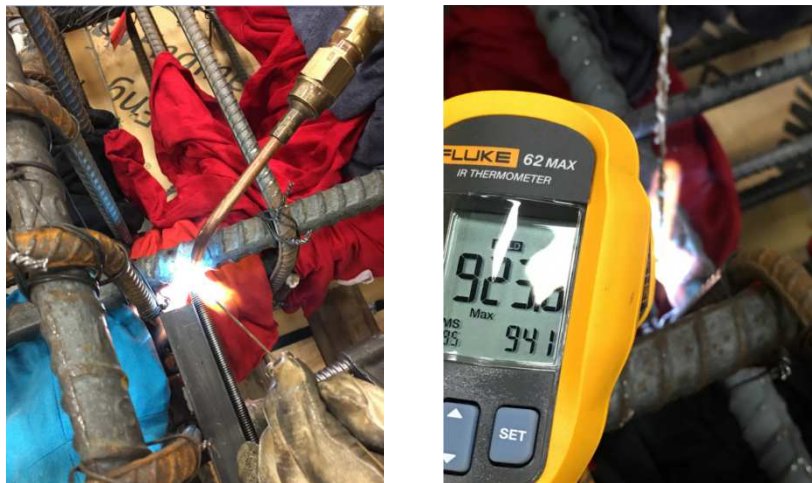
Figure A-16: Brass-Brazing Procedure - Step 3: Heating by Torch

Figure A-17: Brass-Brazing Procedure - Step 5: Removal of Heat and Formation of Bond

This brass-brazing technique is used to attach the threaded rods onto reinforcement for measuring slip of steel bars out of anchorage in specimens SBH60, SBH100, and SBL100 with conventional Grade 60 A706, Grade 100 T/Y = 1.18, and Grade 100 T/Y = 1.30, respectively. This technique has been tested in the laboratory and shown that it does not alter the mechanical properties of these steel types.

Steel specimens are taken from the same batch of reinforcement used in construction of beams SBH60, SBH100, SBL100, and SBM100. A threaded rod is attached on each specimen by brass-brazing technique. All steel coupons are then tested under cyclic loading in tension for ten cycles in Universal Testing Machine. Figure A-18 displays the setup of one of these tests. Another set of four steel specimens from the same batches are also tested under similar loading conditions. These coupons are plain with no procedure performed on. The force-strain relations of steel specimens that is Grade 100 T/Y = 1.30 used in beam SBH100 are shown in Figure A-19. Both plain specimen and the one with threaded rod attached on using brass-brazing technique have similar mechanical properties including low-cycle fatigue. The other Grade 100 T/Y = 1.18 and conventional Grade 60 A706 specimens with brass-brazing procedure performed on also behave similarly with same mechanical properties as corresponding plain ones.

Brass-brazing procedure, however, causes premature fracture of Grade 100 A1035 reinforcement. Therefore, Digital Image Correlation (DIC) technique (Chu et al., 1985) is used instead to measure slip of longitudinal bars in test of beam SBM100. More details on DIC techniques can be found in Arteta (2015).

In the test of specimen SBM100, two small notches are created in concrete at base of test beam to expose the surface of longitudinal reinforcement (Figure A-22). The exposed surface is cleaned, painted white, and black dots are printed on with random patterns. The region is shined with LED flash light and high-resolution cameras are used to take pictures of the region every

ten seconds during test. The first pictures taken prior to test serve as initial state of measurement. Subsequent pictures are taken and analyzed using computer software Optecal to obtain displacement field of subsets of speckle, which is also the slip of reinforcement out of anchorage (Figure A-23 & Figure A-24).
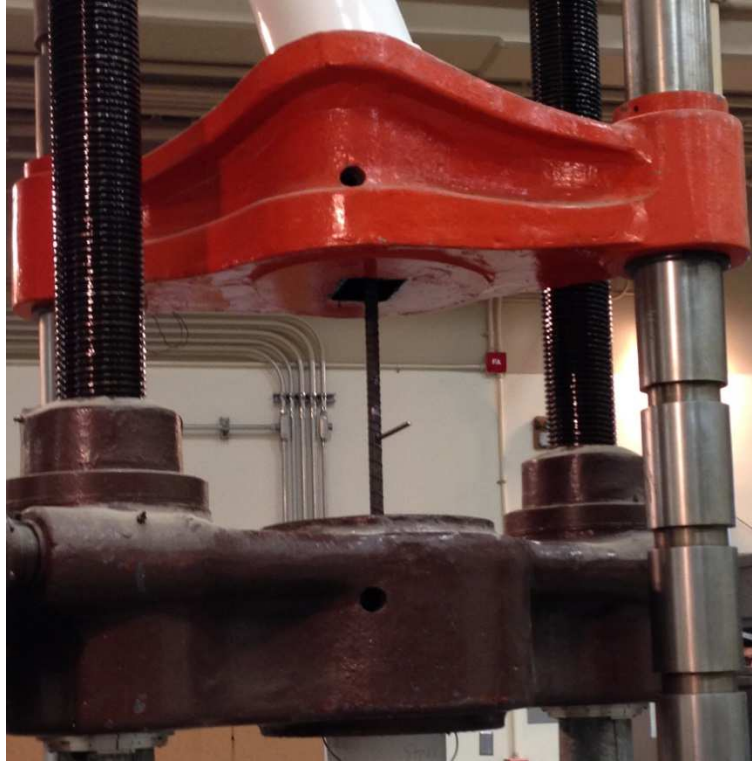
Figure A-18: Test Setup of Steel Specimen with Brass-Brazing - Grade 100 T/Y = 1.30
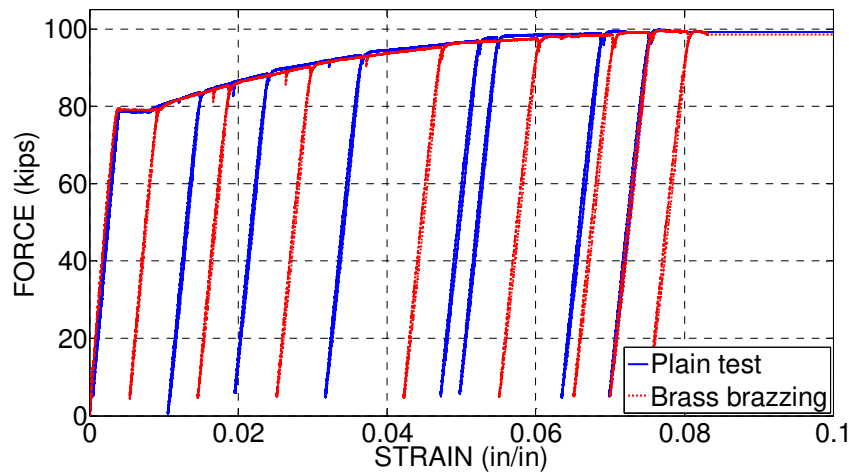
Figure A-19: Stress-Strain Relations of Steel Specimen - Grade 100 T/Y = 1.30
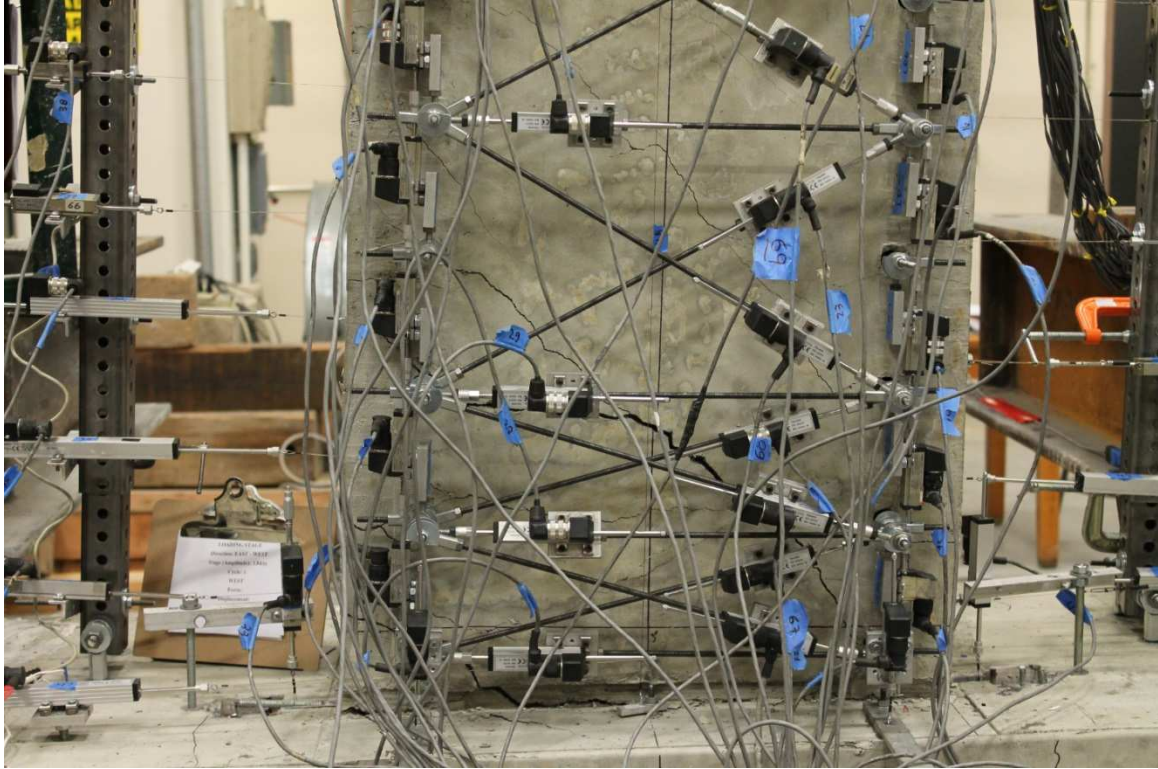
Figure A-20: General Instrumentation for Measuring Slip by Brass-Brazed Threaded Rods
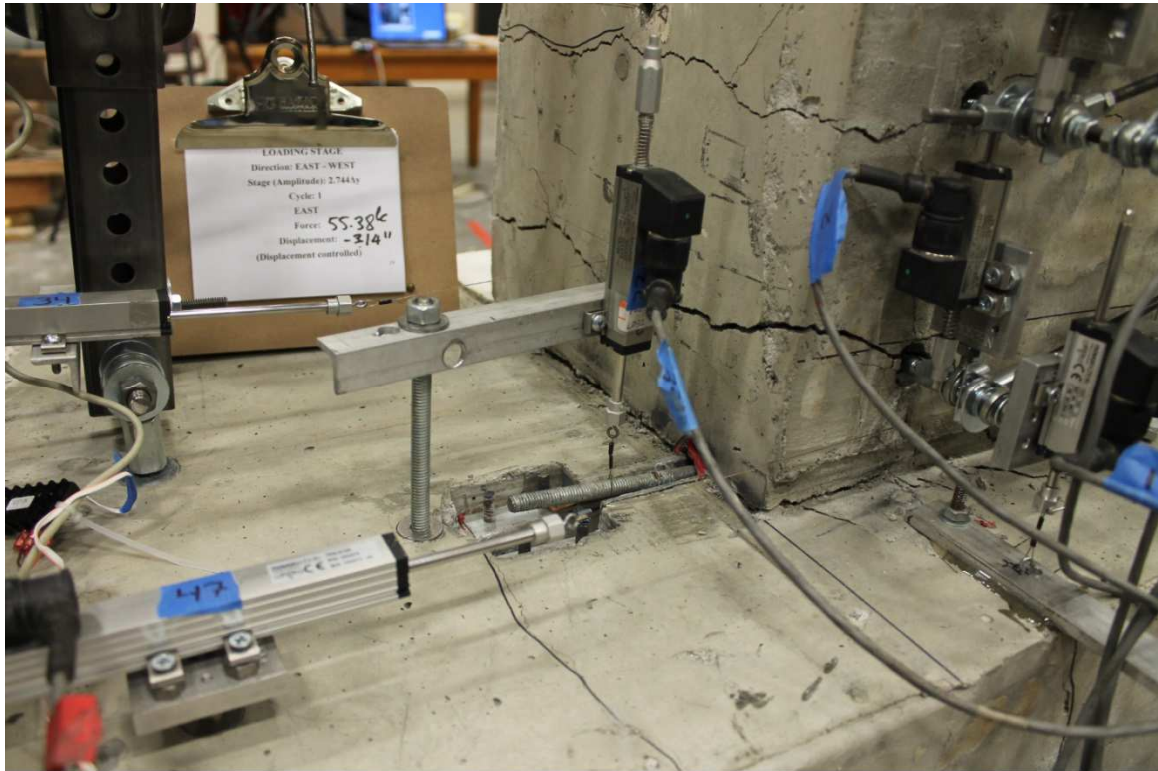
Figure A-21: General Instrumentation for Measuring Slip by Brass-Brazed Threaded Rods
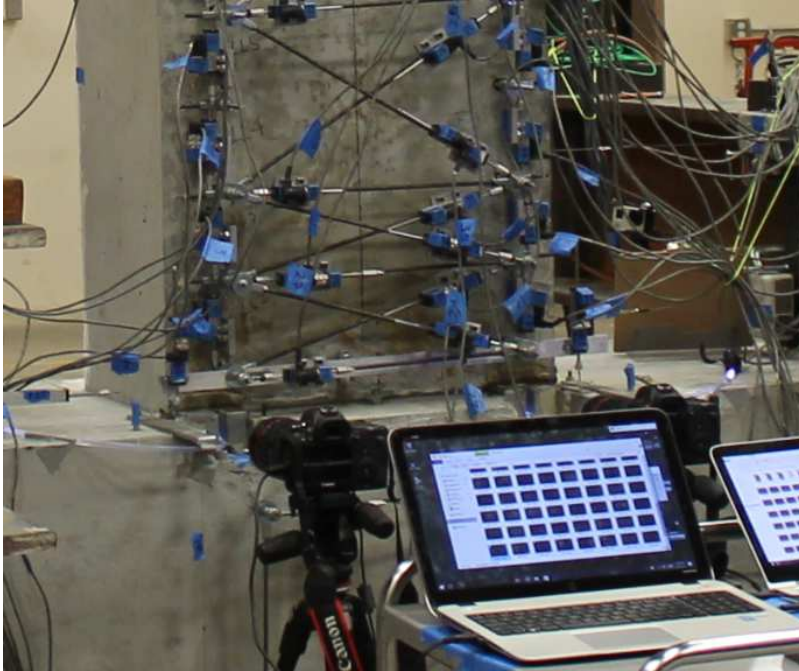
Figure A-22: General Instrumentation for Measuring Slip by Digital Image Correlation (DIC)
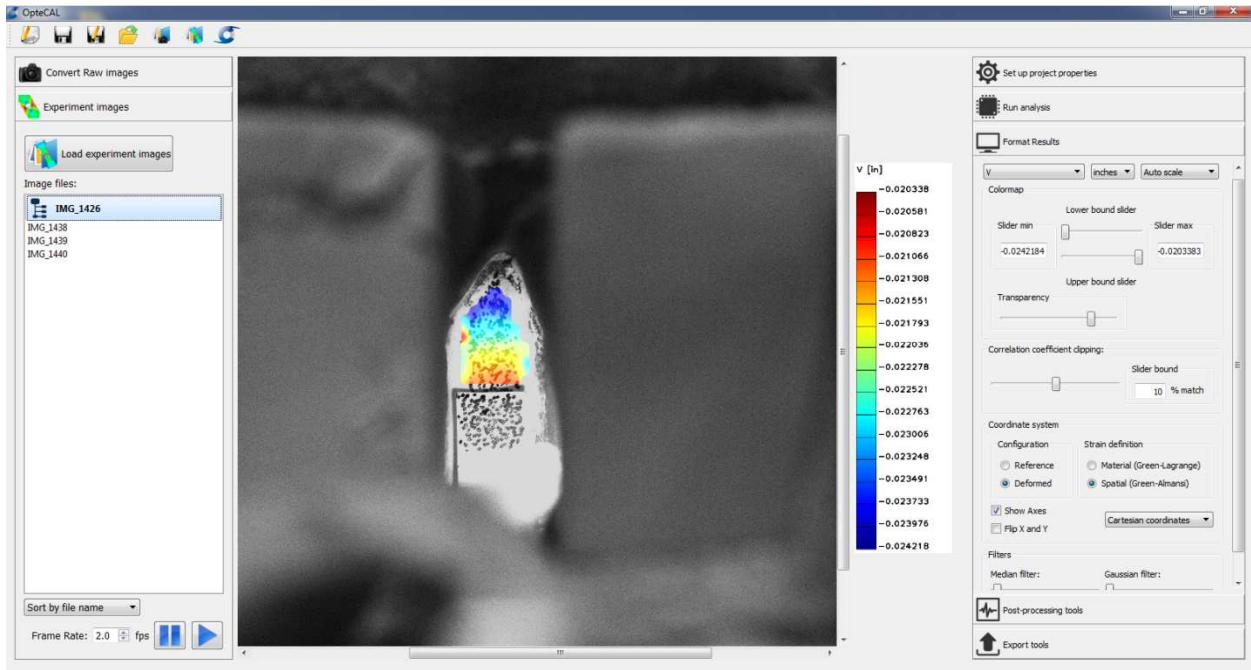
Figure A-23: Data Reduction of DIC
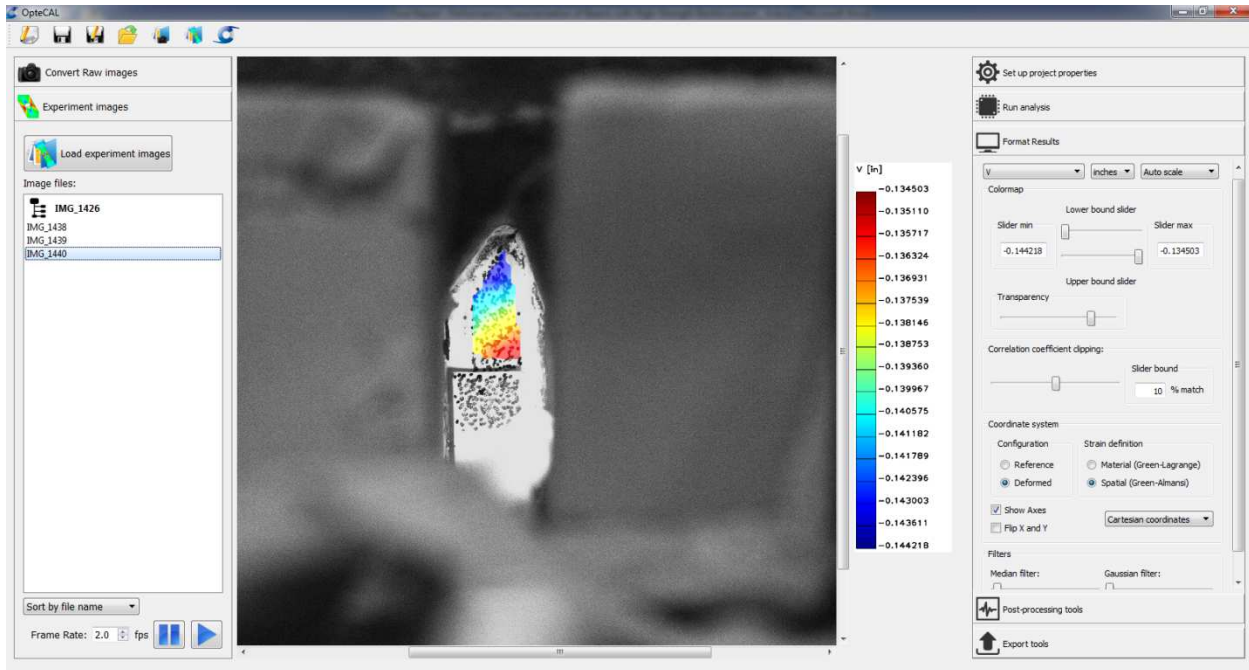
Figure A-24: Data Reduction of DIC

Data Acquisition System

The data acquisition control system enclosure was Pacific Instruments Model 6000 (Figure A-25). Detailed information can be found on http://www.pacificinstruments.com. The data acquisition system control system input/output modules were Pacific Instruments Model 6035, 8-Channel Strain/Bridge Transducer Amplifier-Filter-Digitizer. These modules are particularly suited to strain gauges.

Figure A-25: Left: Data Acquisition System; Right: Analog I/O Modules

TEST PROCEDURES

The loading history to impose on test specimens was developed based on recommendations of FEMA 461 (FEMA, 2007). It consists of two major loading types: load controlled, and displacement controlled. The details are described as below.

Load-controlled cycles:

Lateral load was applied to the specimens using two actuators that were controlled by magnitude of applied load from the beginning of test up to yielding point, which was defined as the amount of force needed to apply on top of the specimen to cause the first longitudinal reinforcement to yield. Load-controlled was chosen for these loading cycles because the magnitudes of load to result in cracking, yielding, and intermediate stages between cracking and yielding on the specimens could be estimated relatively accurately. The corresponding tip displacements resulted from these pre-determined magnitudes of lateral force were measured during test. Accordingly, tip displacement at yield point was measured and used to compute following magnitudes of displacement to be applied to specimens in later displacement-controlled loading cycles. For each magnitude of force, three cycles of loading were applied.

Displacement-controlled cycles:

From measured yield displacement, magnitudes of displacement to be applied onto the top of specimens in displacement-controlled loading cycles were computed by multiplying the displacement of previous cycle by a factor of 1.4 as suggested by FEMA 461. For the pre-determined displacement amplitudes that result in top drift ratio less than 2%, three cycles of loading were applied, while for those resulting in top drift ratio larger than 2%, only two cycles were imposed.

Table A-5 shows the loading sequence of the tests on Beams SBL100, SBH100, and SBM100 while Table A-6 displays that on Beam SBH60. Figure A-26 illustrates the time history of top drift ratio measured or applied onto the beam.

For each loading amplitude of either force- or displacement-controlled, the test beams were loaded from initial position to the peak in East direction first, followed by another peak in the West direction, and one cycle was completed by loading the beam back to initial position. The test was stopped for marking cracks when the specimen was loaded to the peak on the East, and West direction of the first cycle, and the end of loading cycles (either second or third) when the pre-determined applied load or displacement became zero.

Table A-5: Loading Protocol for Beams with Grade 100 Reinforcement

Loading Stage	Number of Cycles	Loading Type
Cracking Force	3	Force-Controlled
0.60Fy	3	Force-Controlled
0.84Fy	3	Force-Controlled
1.00Fy	3	Force-Controlled
1.40Δy	3	Displacement-Controlled
1.96Δy	2	Displacement-Controlled
2.74Δy	2	Displacement-Controlled
3.84Δy	2	Displacement-Controlled
5.38Δy	2	Displacement-Controlled

Table A-6: Loading protocol for Beam with Grade 60 A706 Reinforcement

Loading Stage	Number of Cycles	Loading Type
Cracking Force	3	Force-Controlled
0.60Fy	3	Force-Controlled
0.84Fy	3	Force-Controlled
1.00Fy	3	Force-Controlled
1.40Δy	3	Displacement-Controlled
1.96Δy	3	Displacement-Controlled
2.74Δy	3	Displacement-Controlled
3.84Δy	2	Displacement-Controlled
5.38Δy	2	Displacement-Controlled
7.53Δy	2	Displacement-Controlled
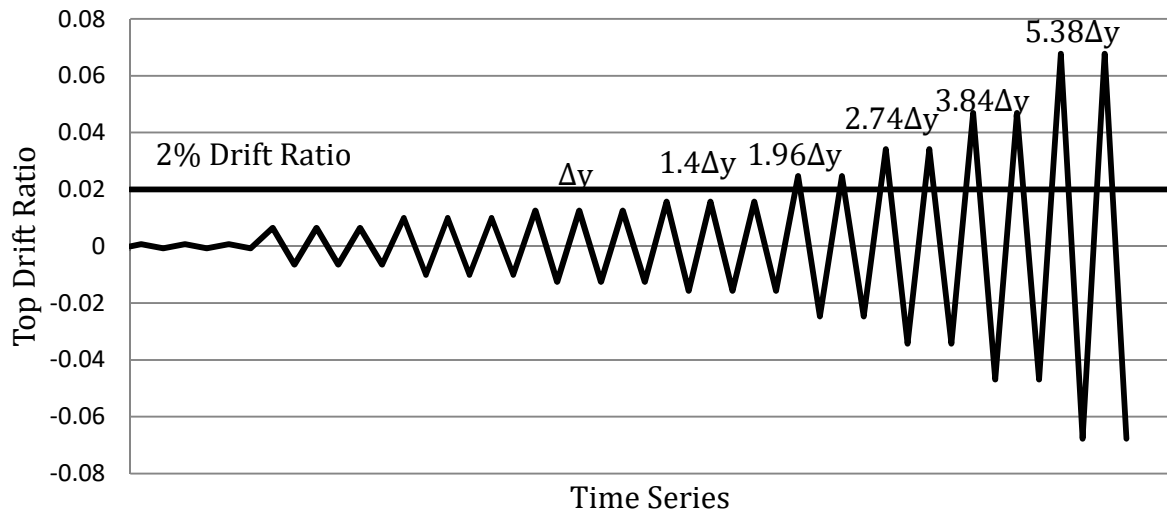
Figure A-26: Loading History

DATA REDUCTION

Global deflection was measured by wire potentiometer (Figure A-27). Lateral force was measured by load cells attached on two actuators that were used to apply force on test specimens. The total force was the sum of the force measured by two load cells projected on direction of loading.

Local deformation was measured by LVDTs. From a truss system of LVDTs as shown in Figure A-27, total deformation was computed from measurement of local deformation based on principle of virtual force:

$$F_v \Delta_r = \sum_{i=1}^{n} f_{i,v} \Delta L_{i,r} \qquad \text{Eq. (12)}$$

where: F_v = virtual force applied horizontally at 52.5 inches above base of beam

Δ_r = real horizontal deflection of interest at 52.5 inches above base of beam

$f_{i,v}$ = virtual internal force in each truss member caused by virtual force F_v

$\Delta L_{i,r}$ = real deformation in each truss member or the change in length of each LVDT in truss system
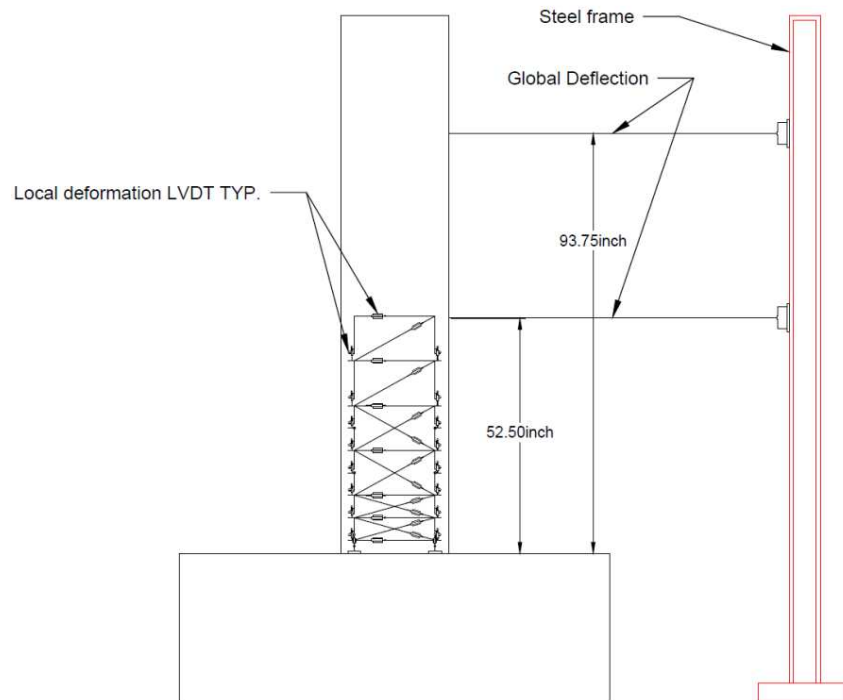
Figure A-27: Instrumentation Scheme for Measuring of Global Deflection and Local Deformation.

Flexural deformation is then defined by contribution of longitudinal truss members (or LVDTs) and shear deformation is that of diagonal and transverse members. The bottom two

longitudinal LVDTs measure both flexural deformation and slip of longitudinal reinforcement out of anchorage. Therefore, another set of LVDTs was used to measure slip of reinforcement separately (Figure A-28) and decoupled from bottom two LVDTs in truss system to obtain flexural deformation.
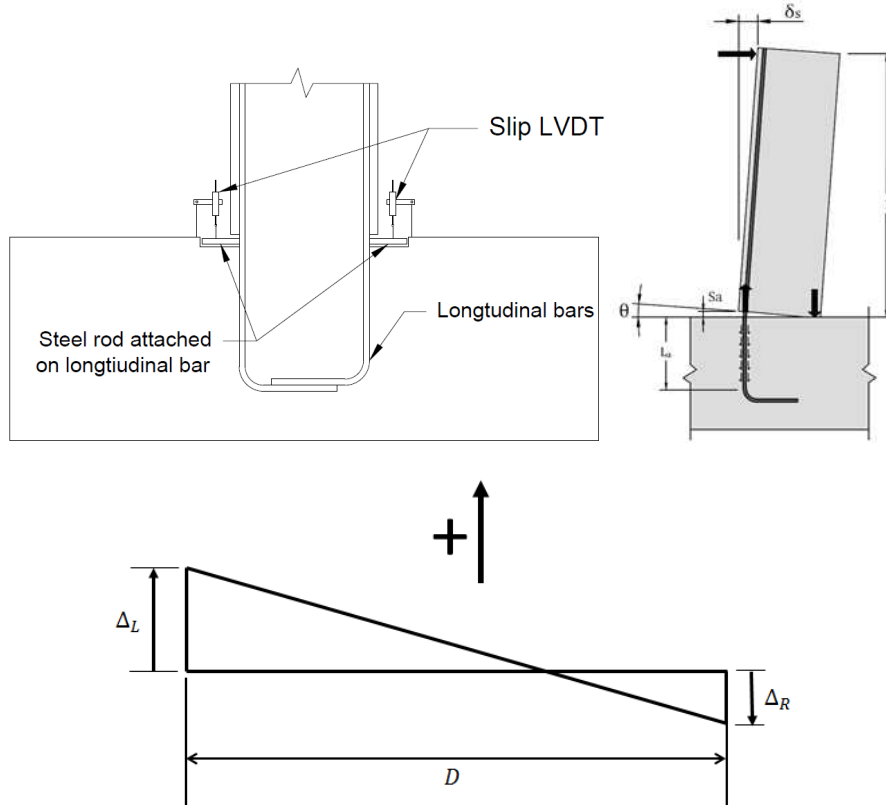
Figure A-28: Instrumentation of Slip Measurement and Computation of Slip Deformation.

Deformation due to slip was then computed by:

$$\delta_s = L\frac{\Delta_L - \Delta_R}{D} \qquad \text{Eq. (13)}$$

where: L = length of test beam from base to loading point

D = distance between two slip LVDTs

Δ_L = change in length of LVDT on the left of beam

Δ_R = change in length of LVDT on the right of beam

All flexural, shear, and slip deformations were calculated from measurement of LVDTs truss system up to location of 52.5 inches above base of beam. Deformation of the remaining section of beam up to tip was computed based on elastic theory of mechanics.
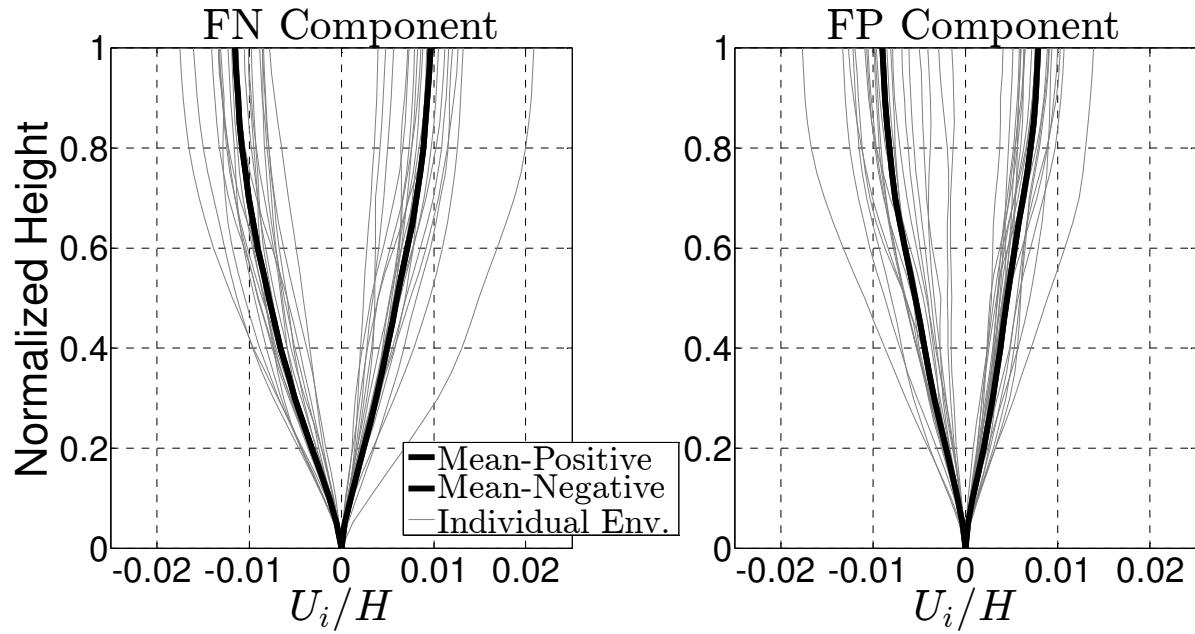
Figure B-1: Drift Envelopes for Frame SBH60
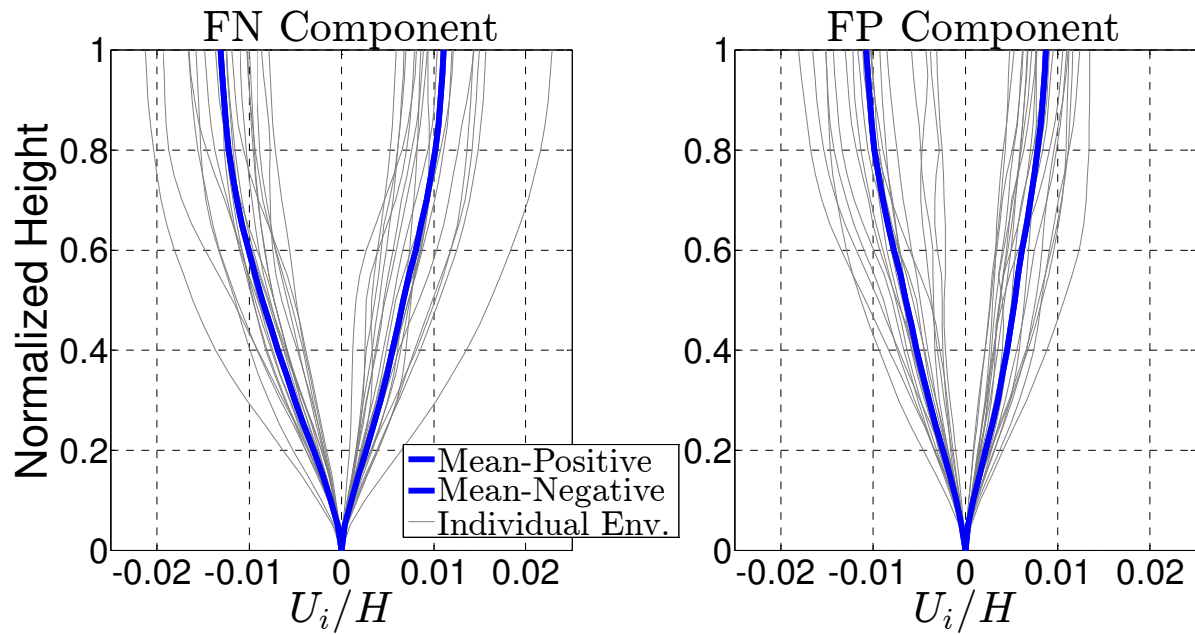
Figure B-2: Drift Envelopes for Frame SBH100 – Left: FN Component – Right: FP Component
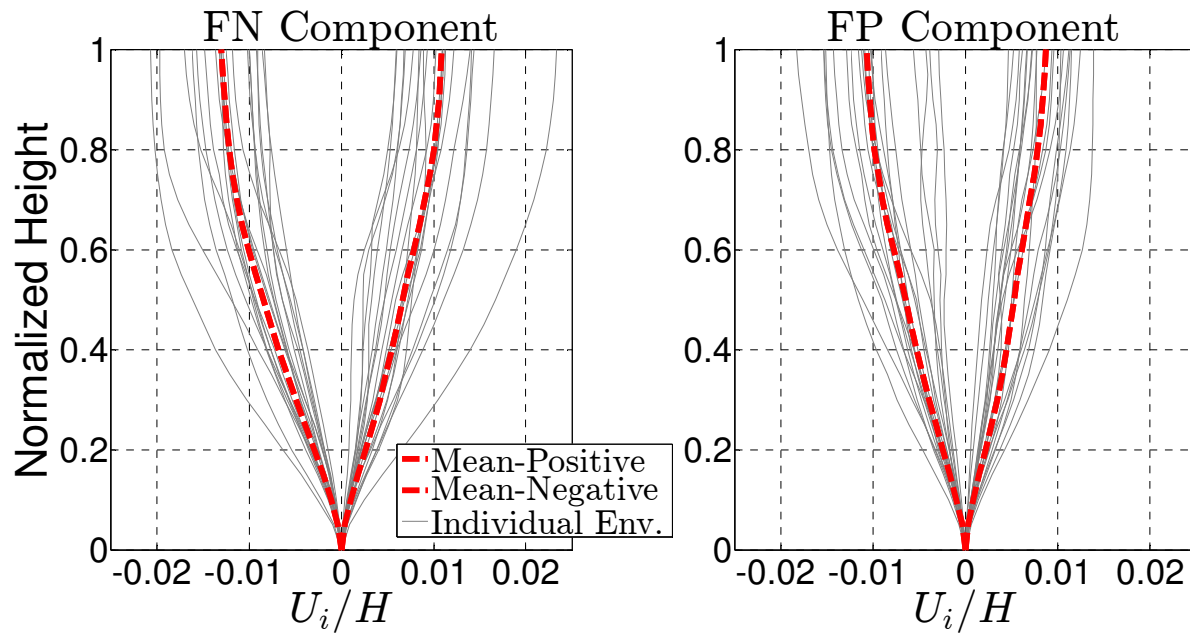
Figure B-3: Drift Envelopes for Frame SBL100 – Left: FN Component – Right: FP Component
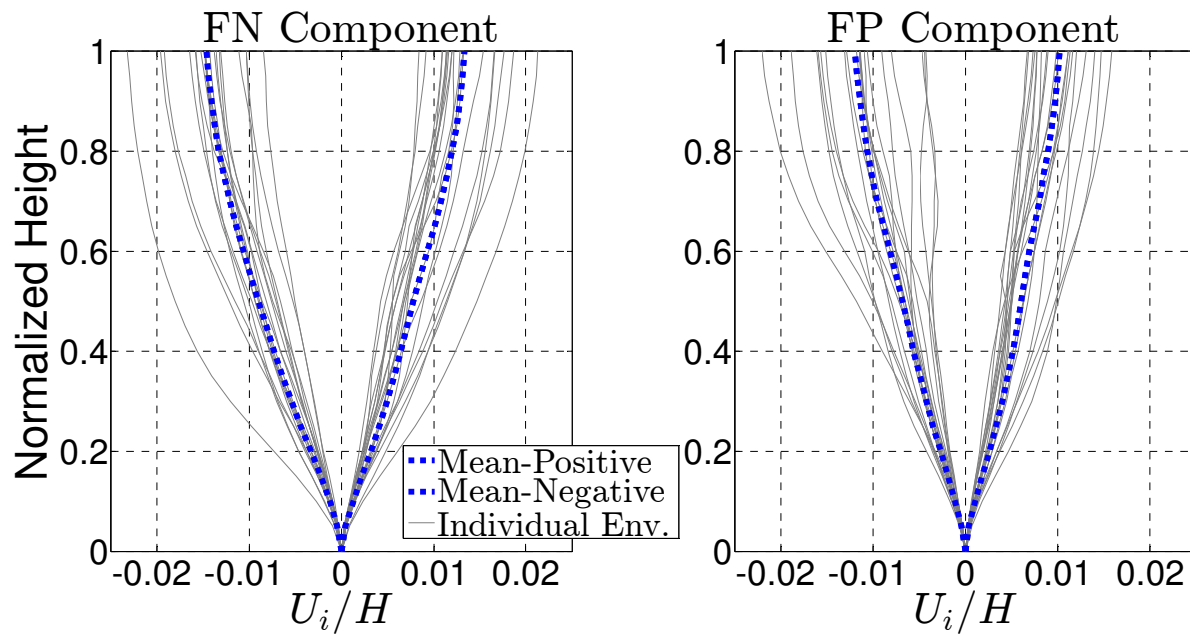
Figure B-4: Drift Envelopes for Frame SBM100 – Left: FN Component – Right: FP Component
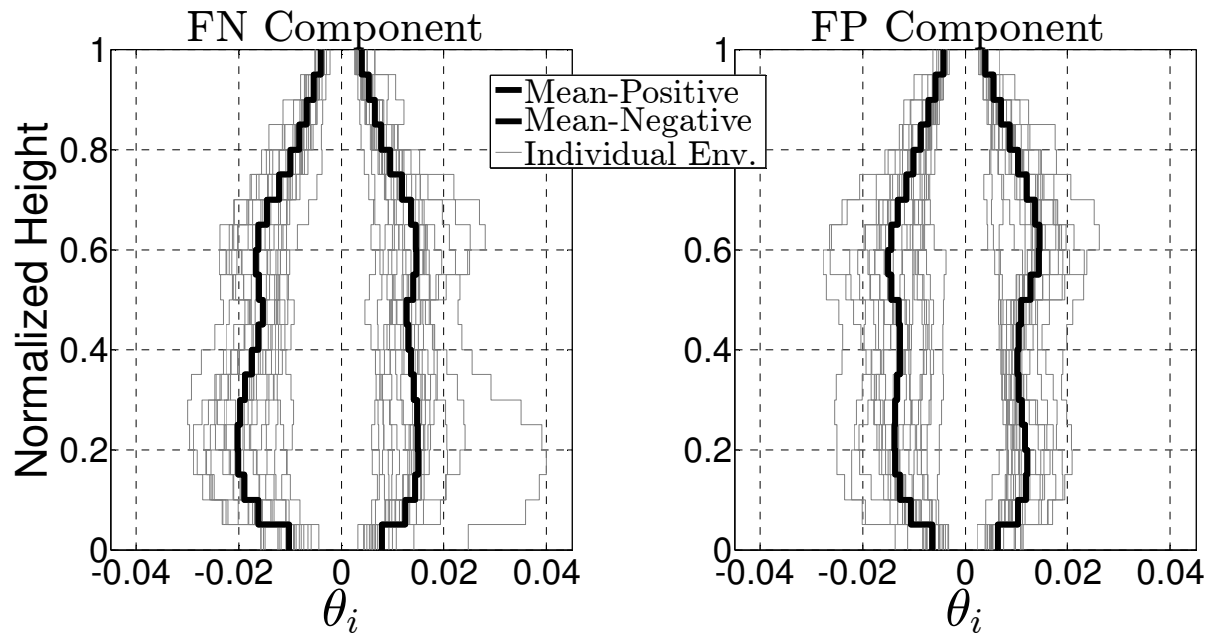
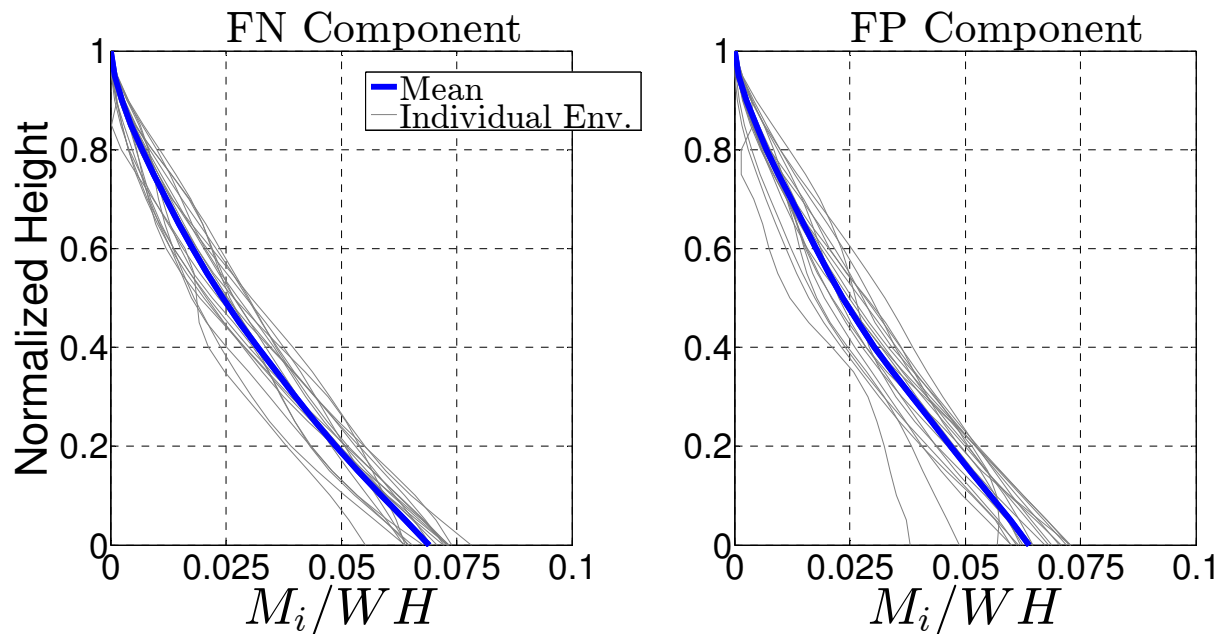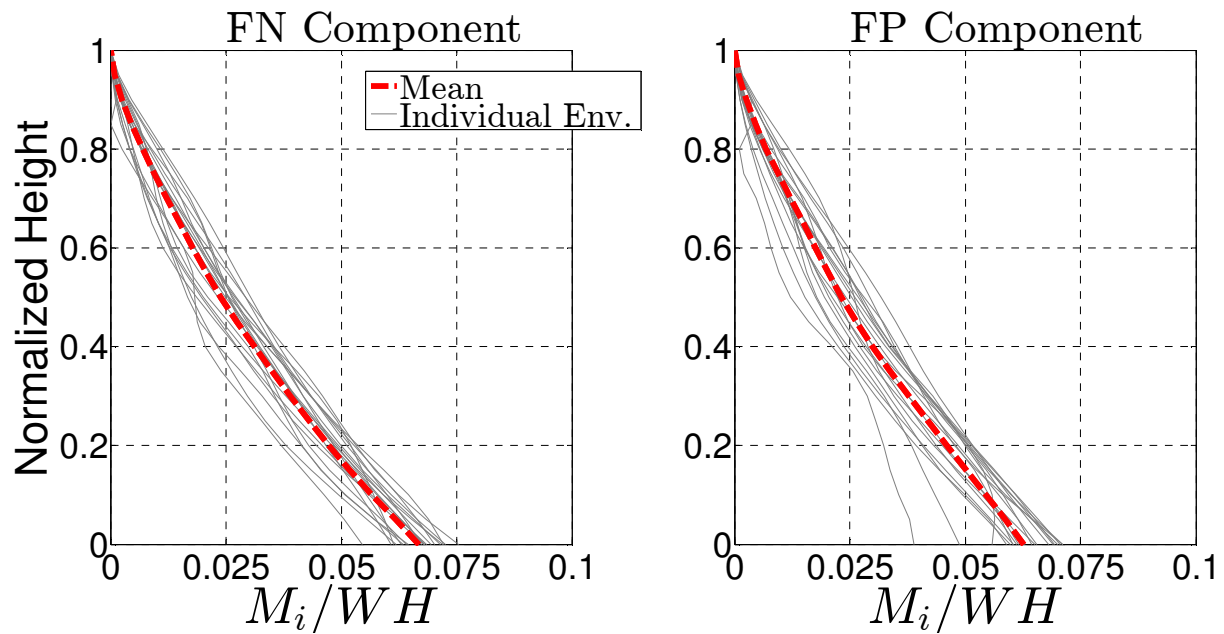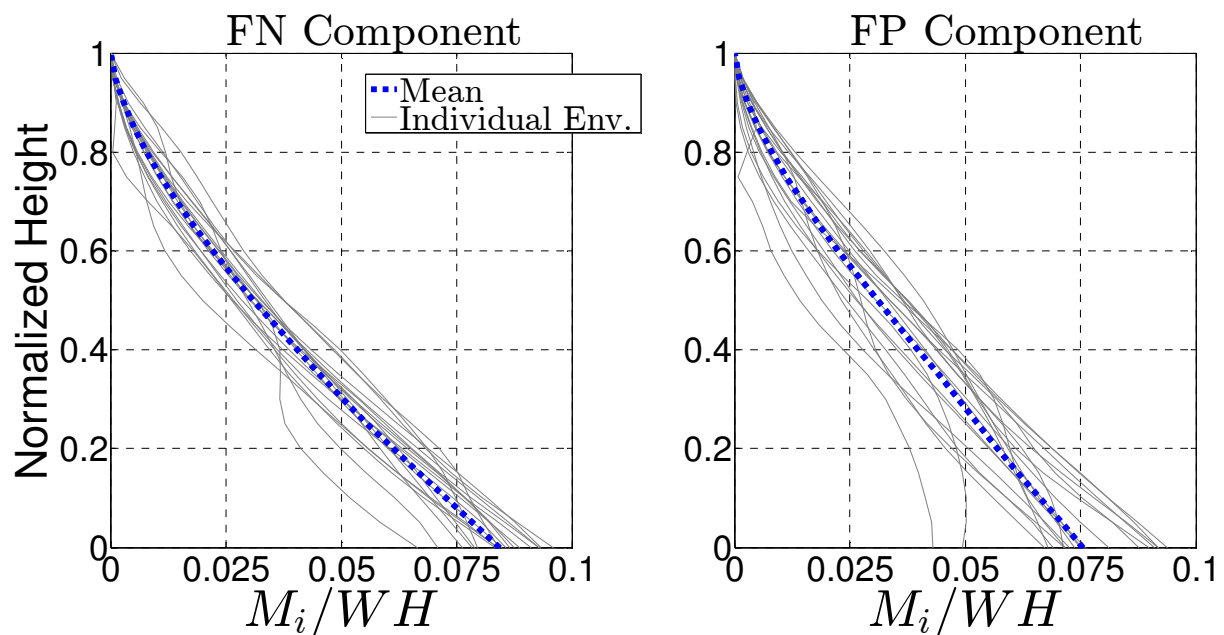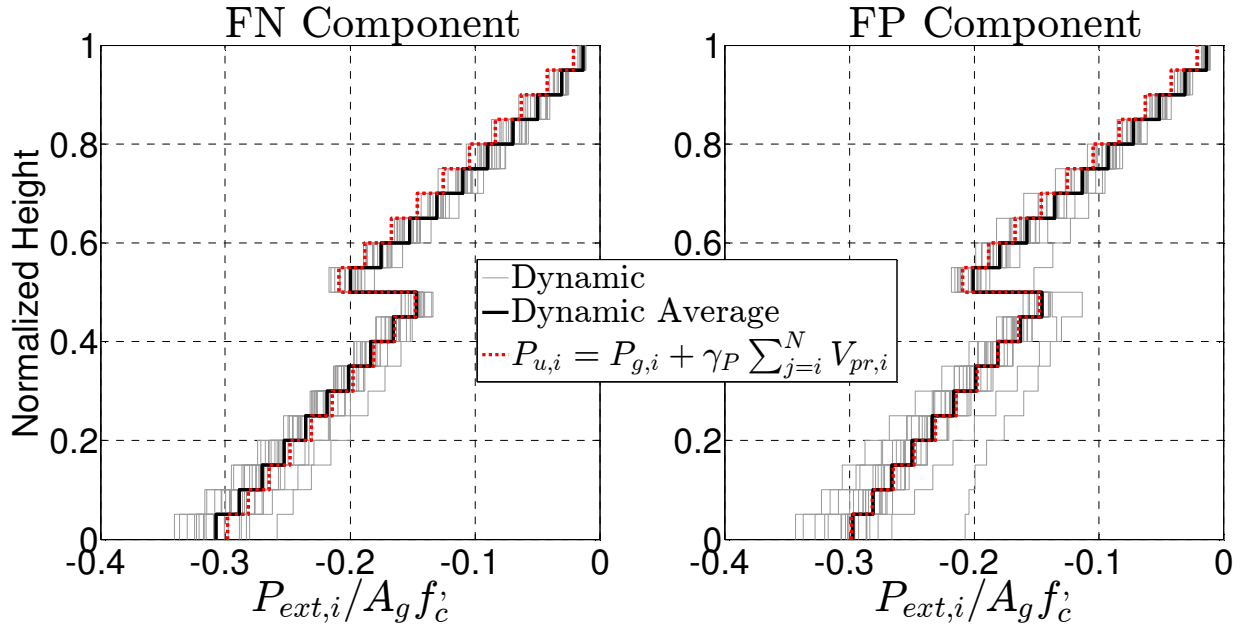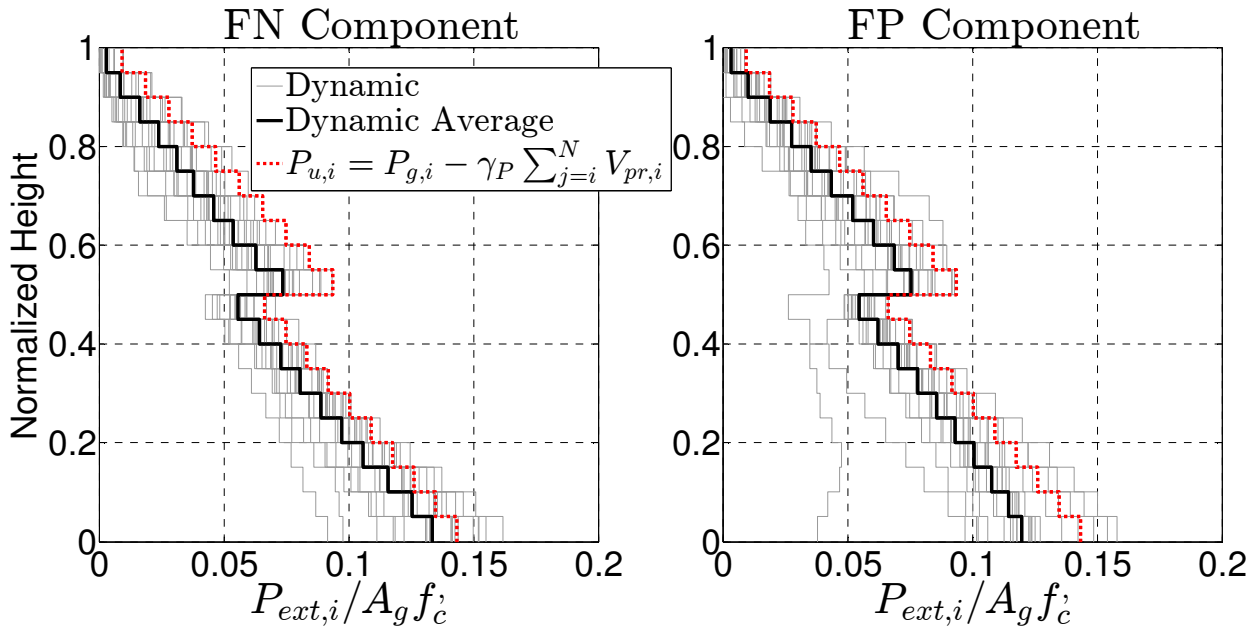Figure B-5: Story Drift Envelopes for Frame SBH60 – Left: FN Component – Right: FP Component
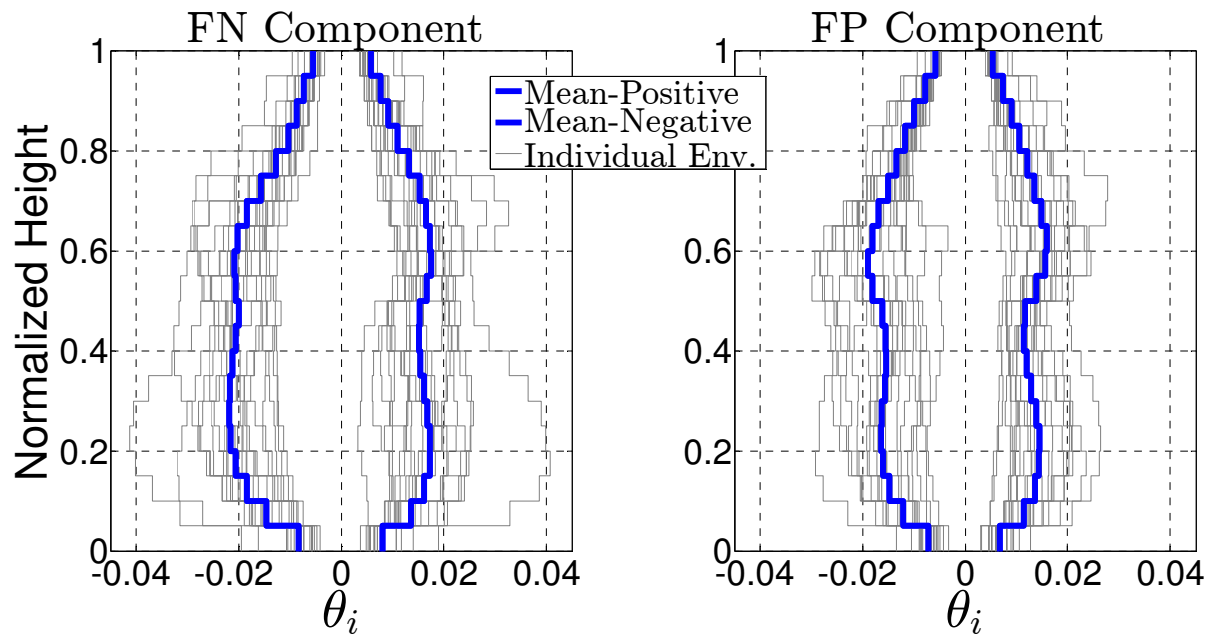
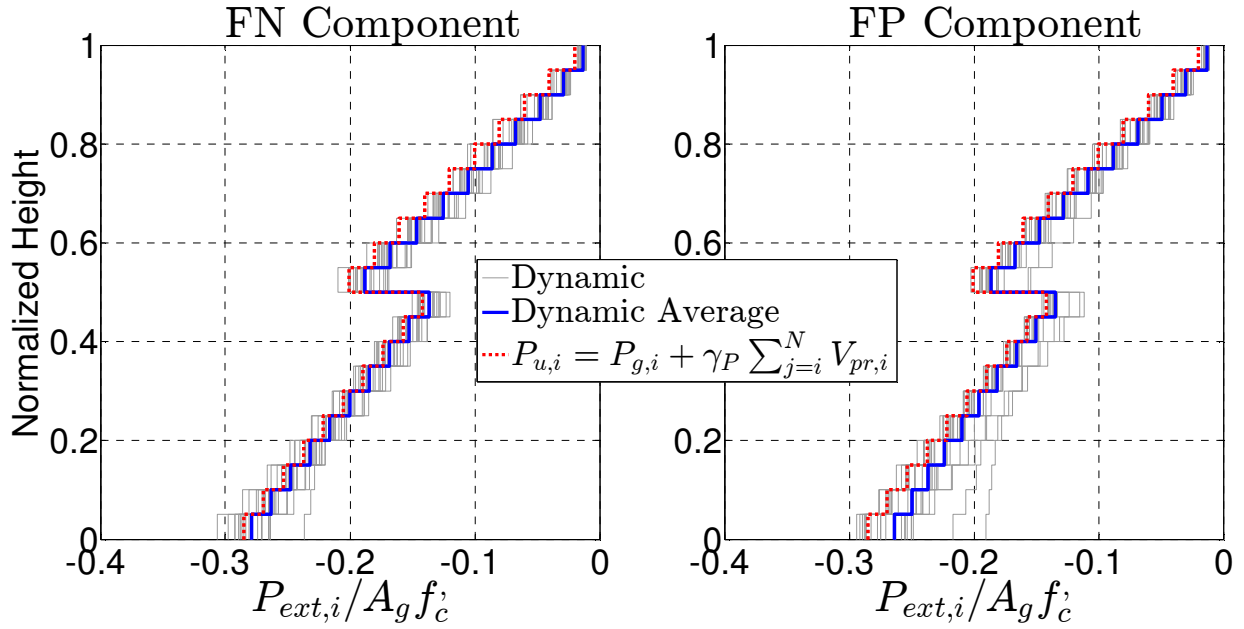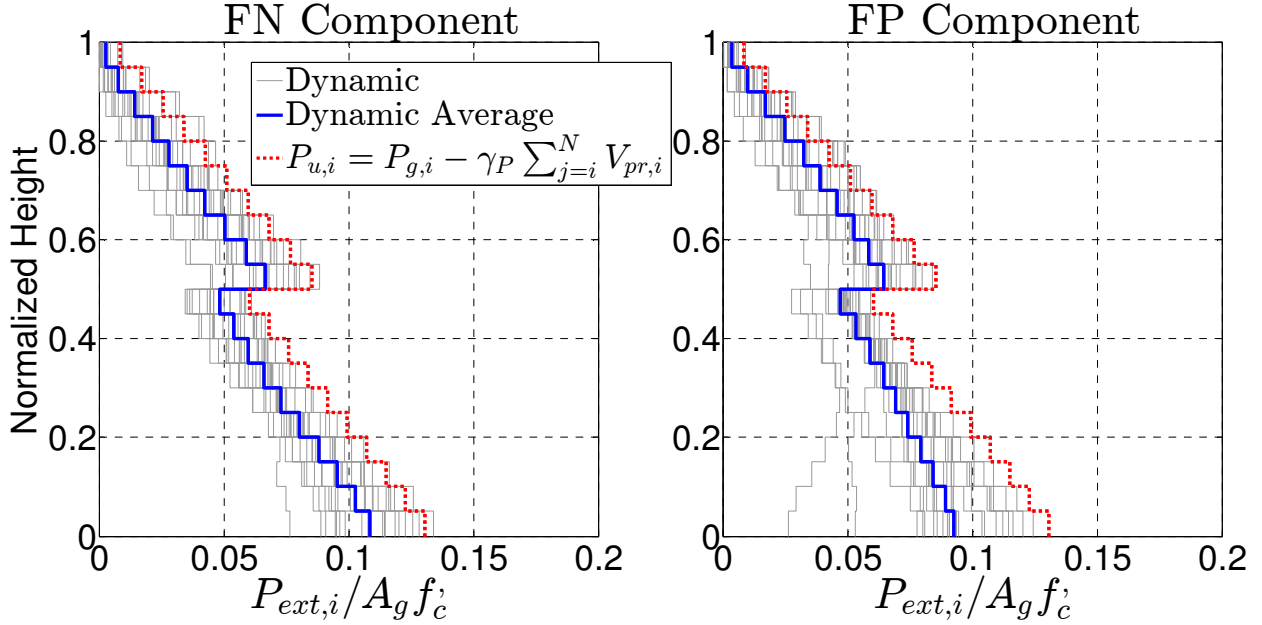Figure B-6: Story Drift Envelopes for Frame SBH100 – Left: FN Component – Right: FP Component
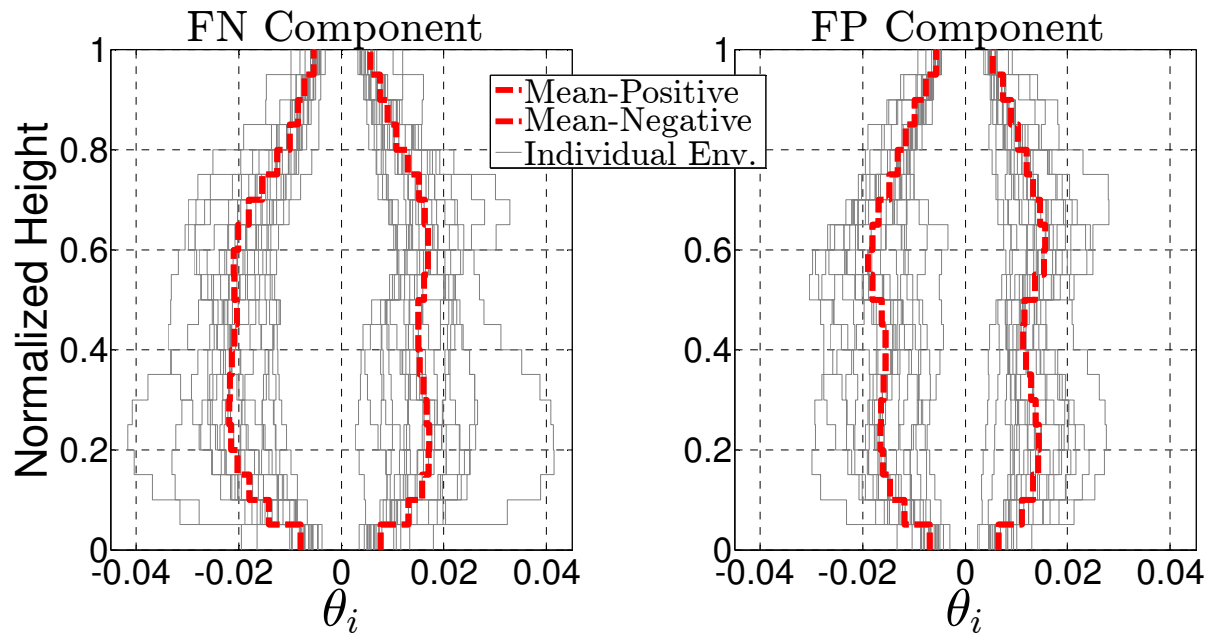
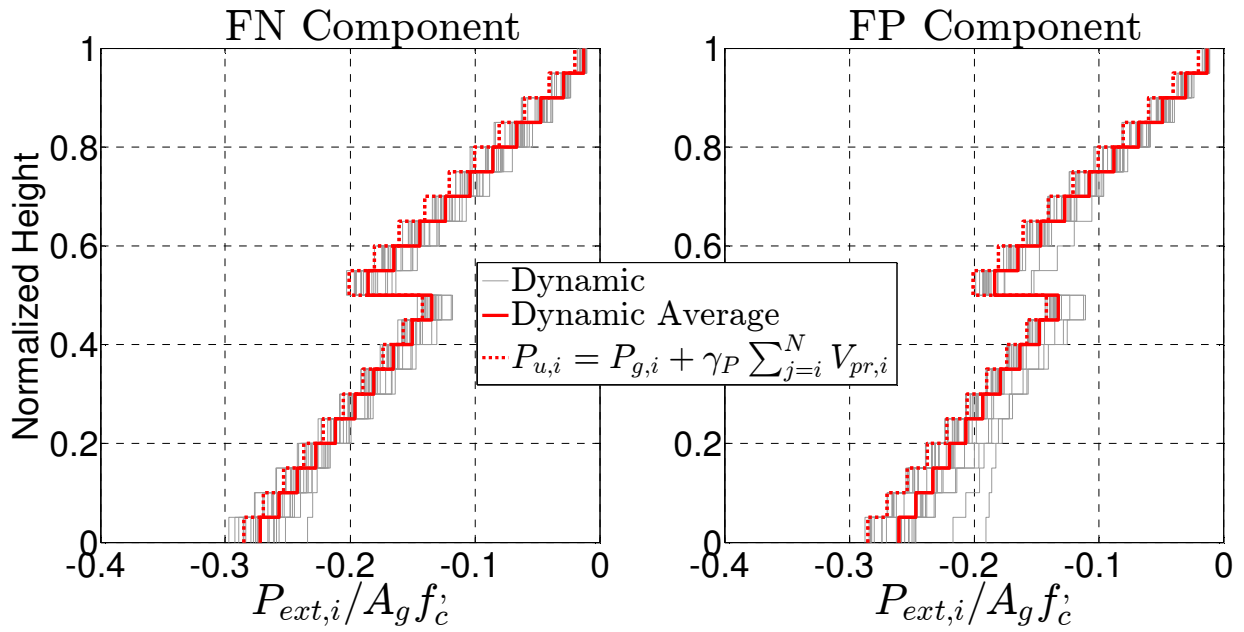Figure B-7: Story Drift Envelopes for Frame SBL100 – Left: FN Component – Right: FP Component
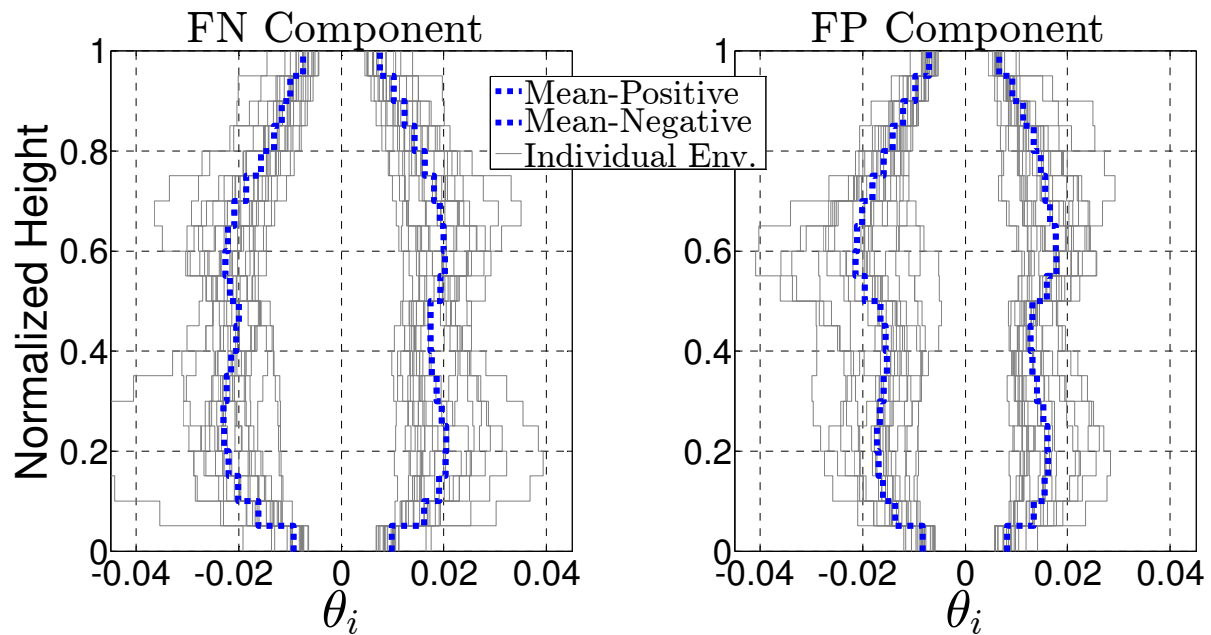
Figure B-8: Story Drift Envelopes for Frame SBM100 – Left: FN Component – Right: FP Component
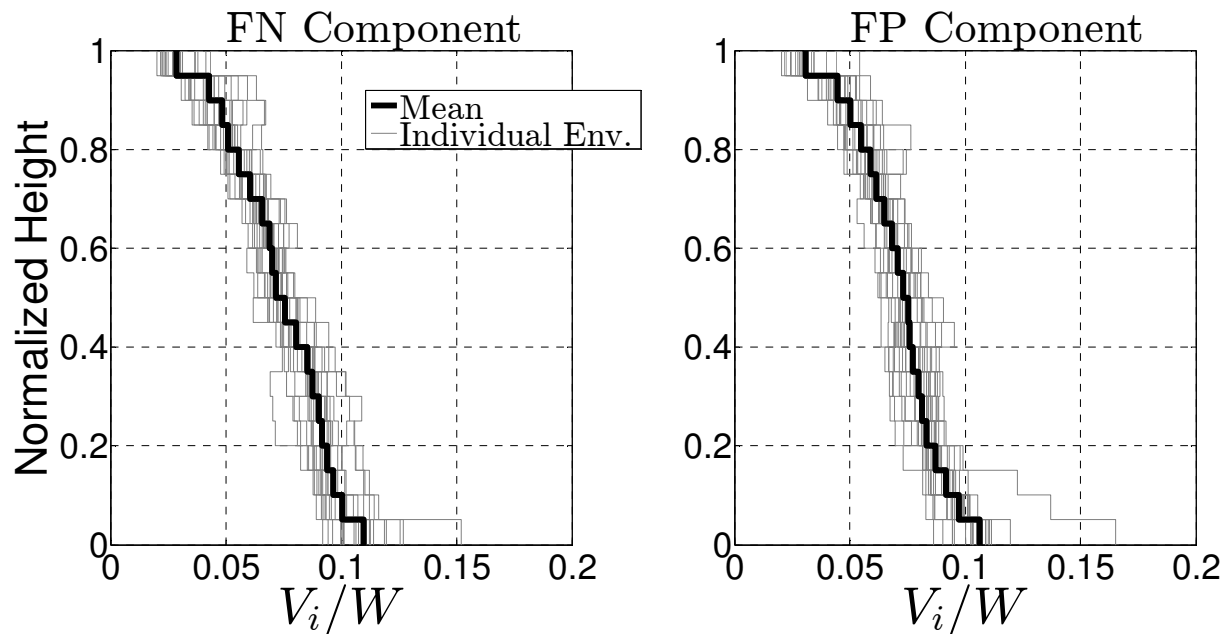
Figure B-9: Story Shear Envelopes for Frame SBH60 – Left: FN Component – Right: FP Component
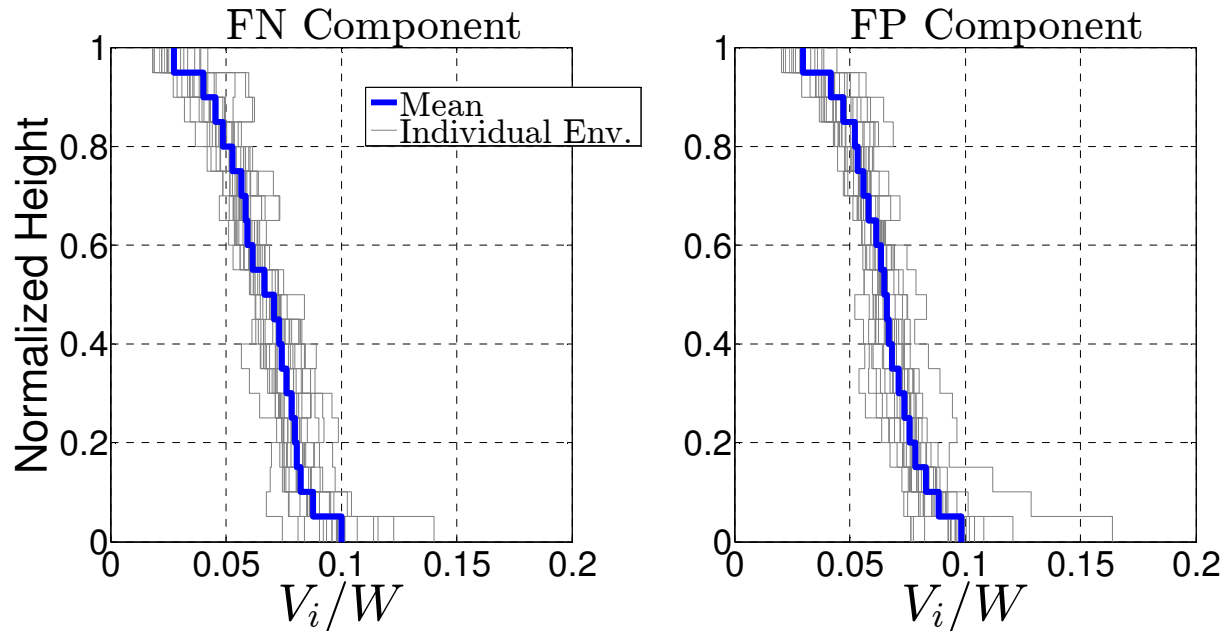
Figure B-10: Story Shear Envelopes for Frame SBH100 – Left: FN Component – Right: FP Component
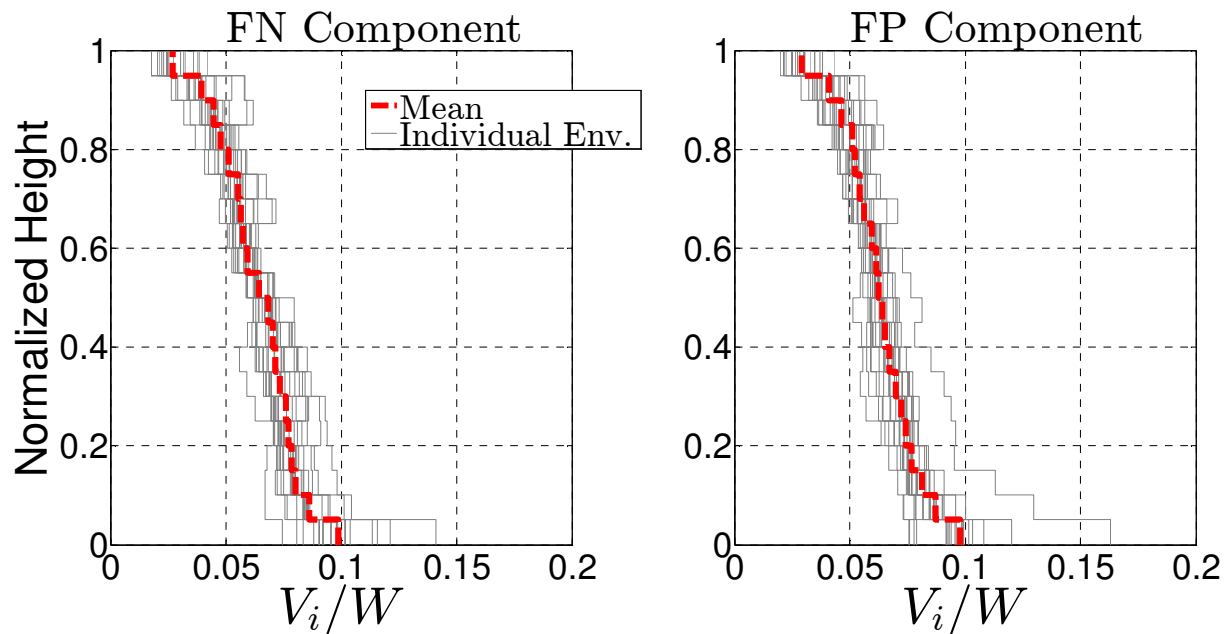
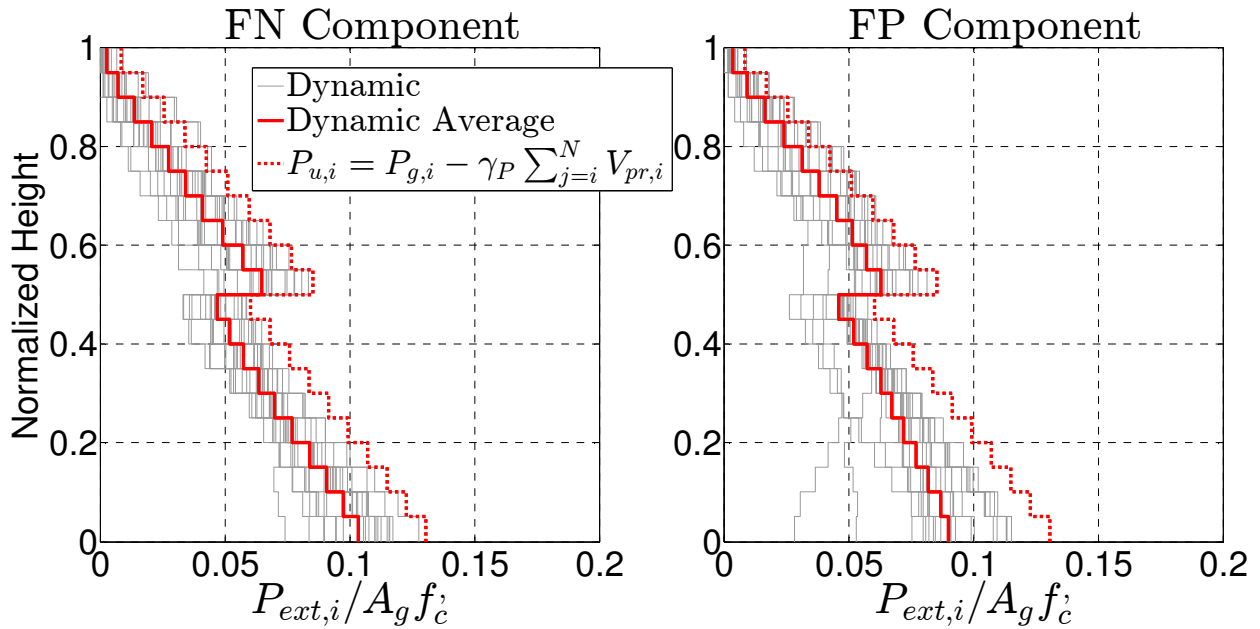Figure B-11: Story Shear Envelopes for Frame SBL100 – Left: FN Component – Right: FP Component
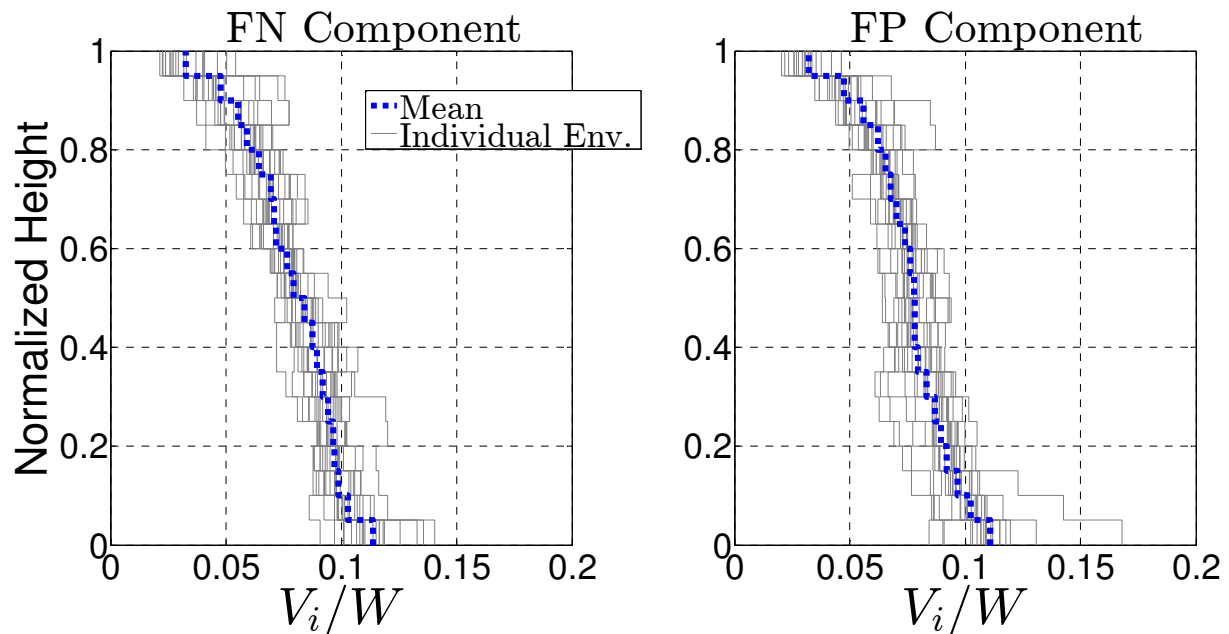
Figure B-12: Story Shear Envelopes for Frame SBM100 – Left: FN Component – Right: FP Component

FN Component
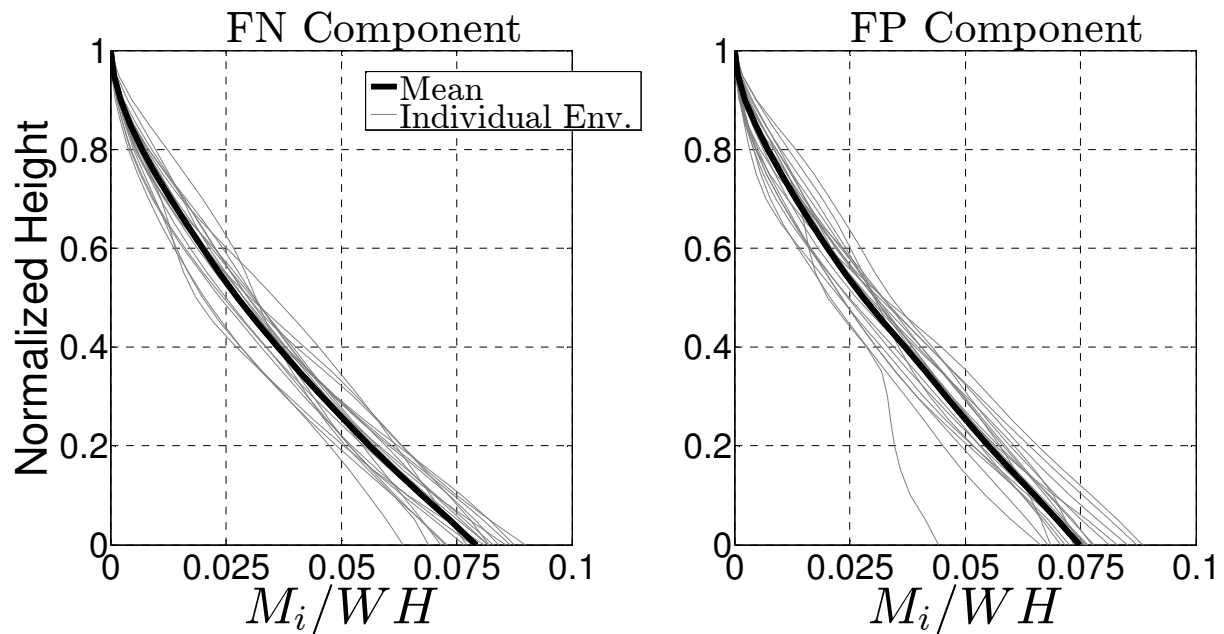
FP Component

Figure B-13: Story Moment Envelopes for Frame SBH60 – Left: FN Component – Right: FP Component

FN Component

FP Component

Figure B-14: Story Moment Envelopes for Frame SBH100 – Left: FN Component – Right: FP Component

Figure B-15: Story Moment Envelopes for Frame SBL100 – Left: FN Component – Right: FP Component

Figure B-16: Story Moment Envelopes for Frame SBM100 – Left: FN Component – Right: FP Component

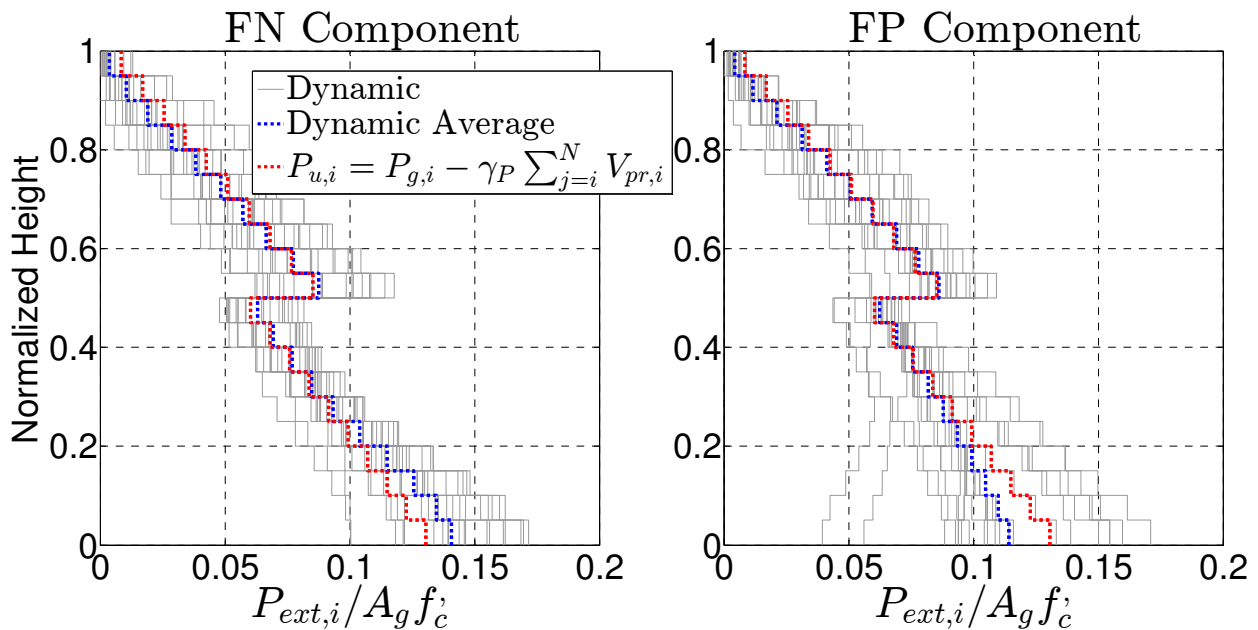Figure B-17: Exterior Column Compression in Frame SBH60 – Left: FN Component – Right: FP Component

Figure B-18: Exterior Column Tension in Frame SBH60 – Left: FN Component – Right: FP Component

Figure B-19: Exterior Column Compression in Frame SBH100 – Left: FN Component – Right: FP Component

Figure B-20: Exterior Column Tension in Frame SBH100 – Left: FN Component – Right: FP Component

Figure B-21: Exterior Column Compression in Frame SBL100 – Left: FN Component – Right: FP Component

Figure B-22: Exterior Column Tension in Frame SBL100 – Left: FN Component – Right: FP Component
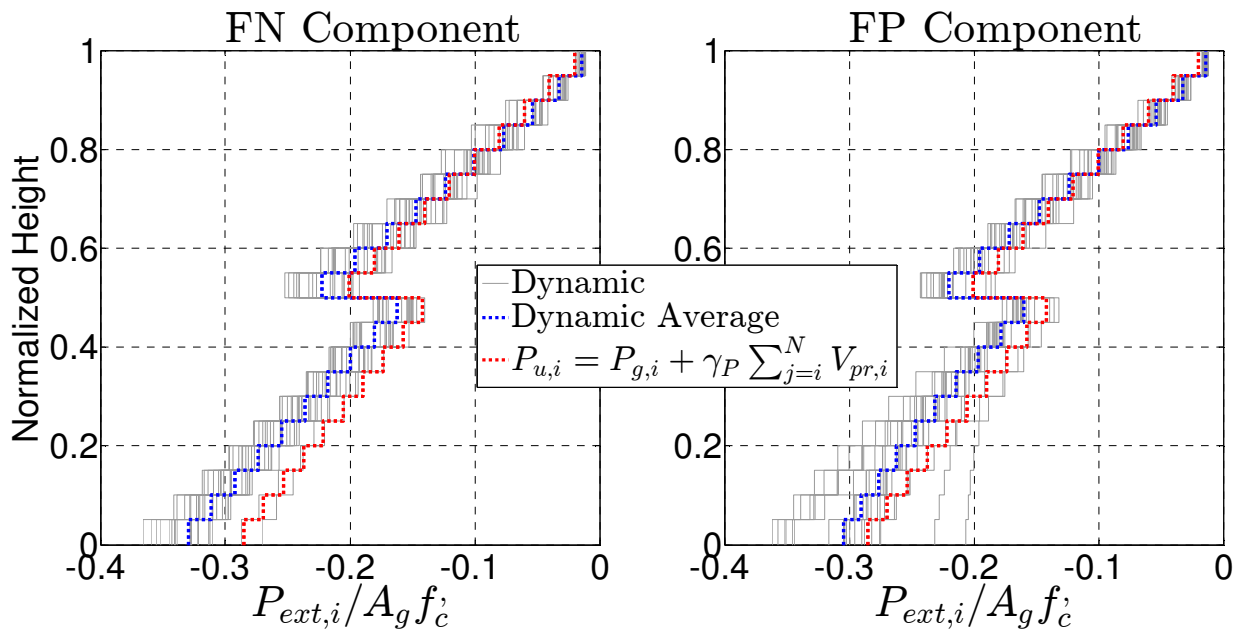
Figure B-23: Exterior Column Compression in Frame SBM100 – Left: FN Component – Right: FP Component

Figure B-24: Exterior Column Tension in Frame SBM100 – Left: FN Component – Right: FP Component

APPENDIX C.   TEST RESULTS

MEASURED CRACK WIDTHS

Crack widths were measured during pauses in each loading amplitude as described in Test Procedures section and presented in details here. In each figure, the left, middle, and right pictures display measured cracked widths when the test specimens were loaded to the West, East directions, and at the end of loading cycle (original position), respectively.

Specimen SBH60
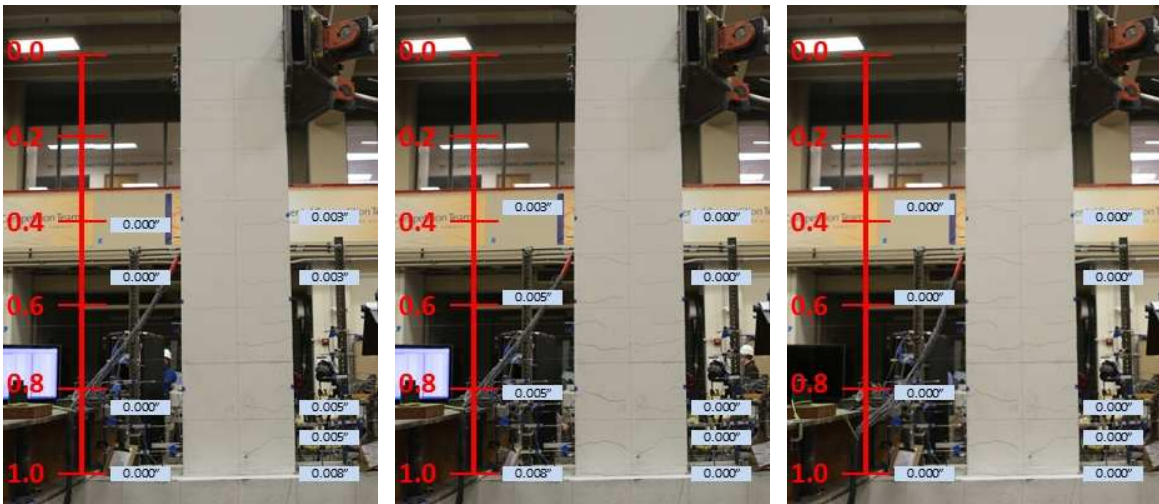
Figure C-1: Measured Crack Widths at Drift Ratio of 0.35% – Specimen SBH60

Figure C-2: Measured Crack Widths at Drift Ratio of 0.5% – Specimen SBH60

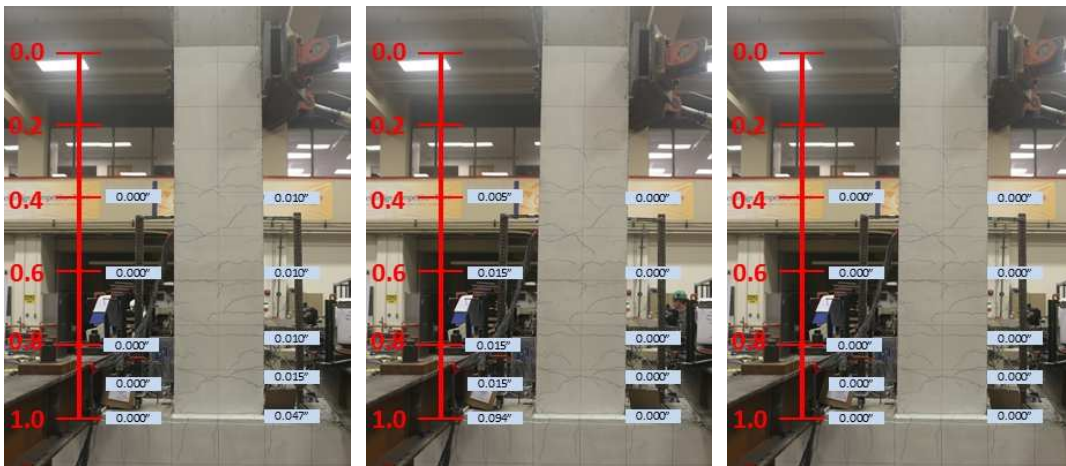Figure C-3: Measured Crack Widths at Drift Ratio of 0.6% – Specimen SBH60

Figure C-4: Measured Crack Widths at Drift Ratio of 0.9% – Specimen SBH60
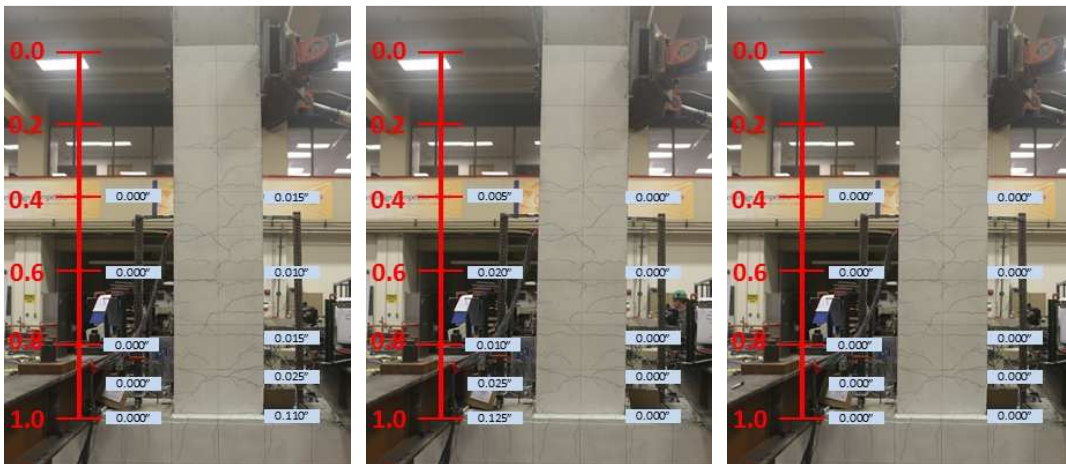

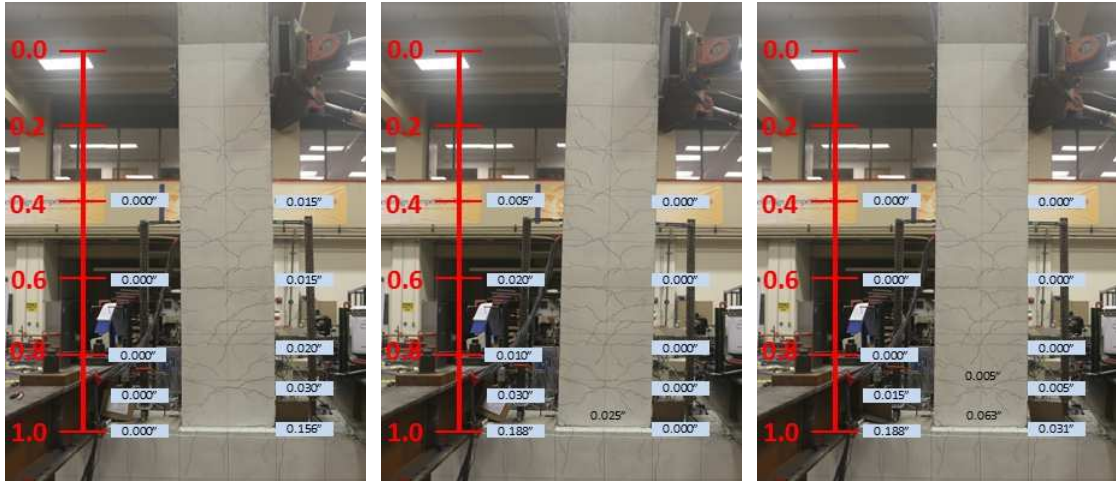Figure C-5: Measured Crack Widths at Drift Ratio of 1.25% – Specimen SBH60

Figure C-6: Measured Crack Widths at Drift Ratio of 1.75% – Specimen SBH60

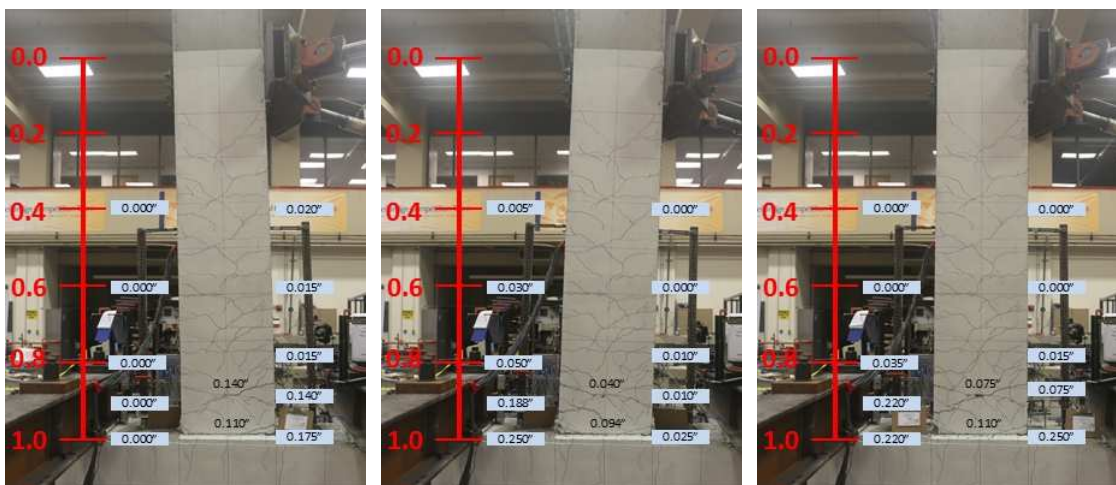Figure C-7: Measured Crack Widths at Drift Ratio of 2.45% – Specimen SBH60

Figure C-8: Measured Crack Widths at Drift Ratio of 3.45% – Specimen SBH60

Specimen SBH100
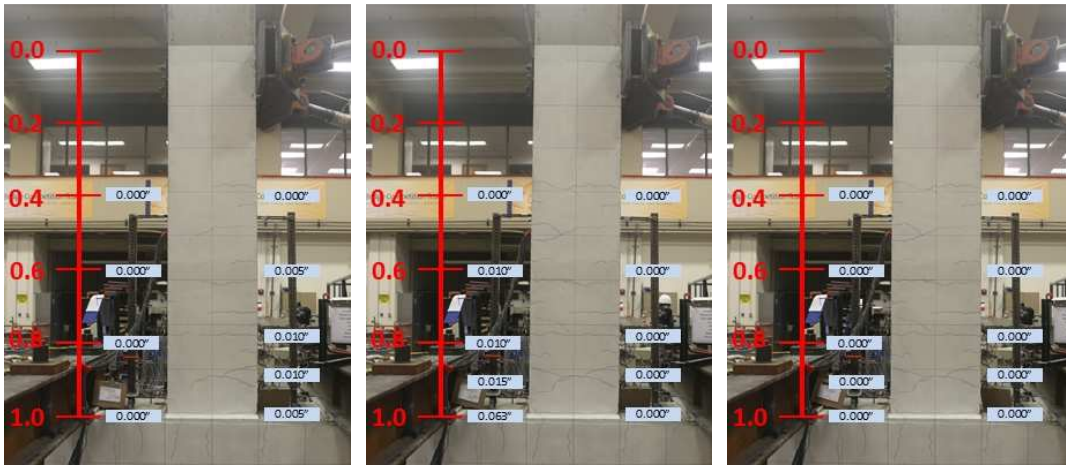
Figure C-9: Measured Crack Widths at Drift Ratio of 0.6% – Specimen SBH100

Figure C-10: Measured Crack Widths at Drift Ratio of 0.9% – Specimen SBH100

Figure C-11: Measured Crack Widths at Drift Ratio of 1.25% – Specimen SBH100

Figure C-12: Measured Crack Widths at Drift Ratio of 1.75% – Specimen SBH100

Figure C-13: Measured Crack Widths at Drift Ratio of 2.45% – Specimen SBH100

Figure C-14: Measured Crack Widths at Drift Ratio of 3.45% – Specimen SBH100
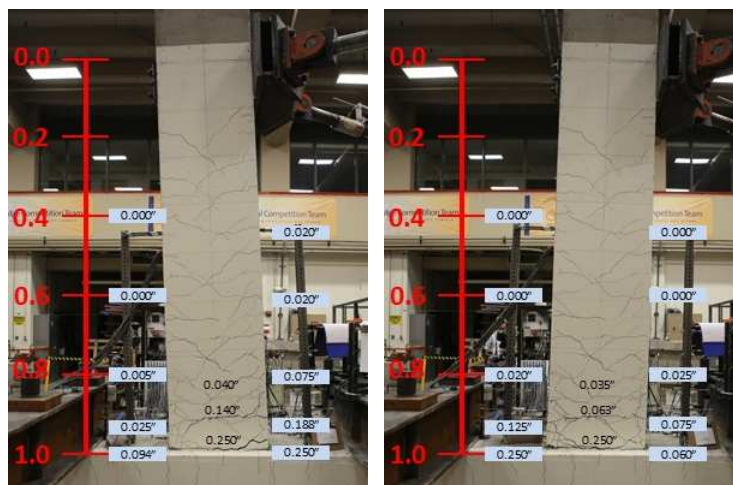
Figure C-15: Measured Crack Widths at Drift Ratio of 4.85% – Specimen SBH100
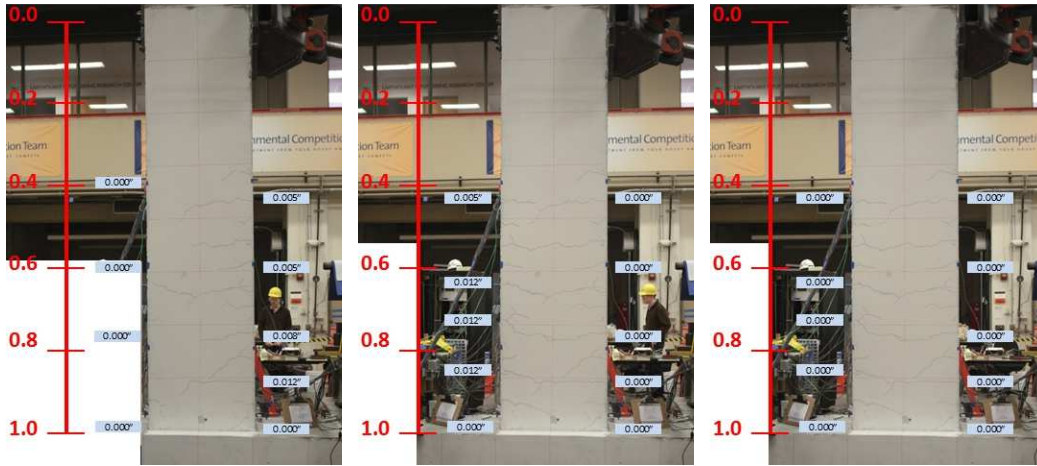
Specimen SBL100

Figure C-16: Measured Crack Widths at Drift Ratio of 0.6% – Specimen SBL100
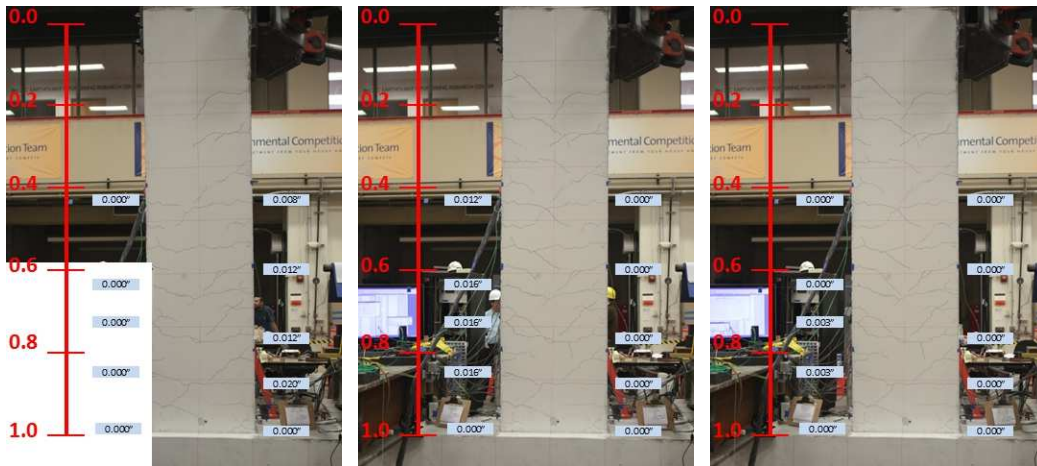
Figure C-17: Measured Crack Widths at Drift Ratio of 0.9% – Specimen SBL100

Figure C-18: Measured Crack Widths at Drift Ratio of 1.25% – Specimen SBL100

Figure C-19: Measured Crack Widths at Drift Ratio of 1.75% – Specimen SBL100

Figure C-20: Measured Crack Widths at Drift Ratio of 2.45% – Specimen SBL100

Figure C-21: Measured Crack Widths at Drift Ratio of 3.45% – Specimen SBL100

Figure C-22: Measured Crack Widths at Drift Ratio of 4.85% – Specimen SBL100

Specimen SBM100

Figure C-23: Measured Crack Widths at Drift Ratio of 0.6% – Specimen SBM100

Figure C-24: Measured Crack Widths at Drift Ratio of 0.9% – Specimen SBM100
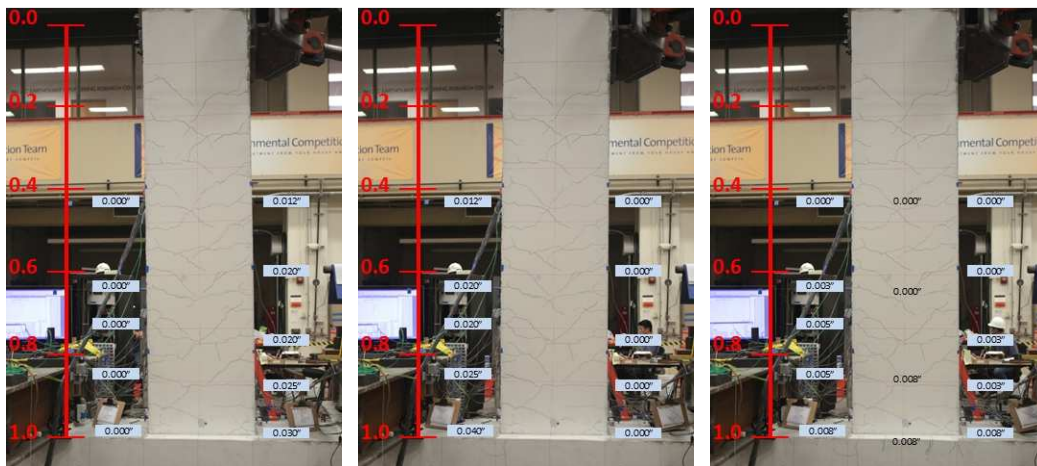

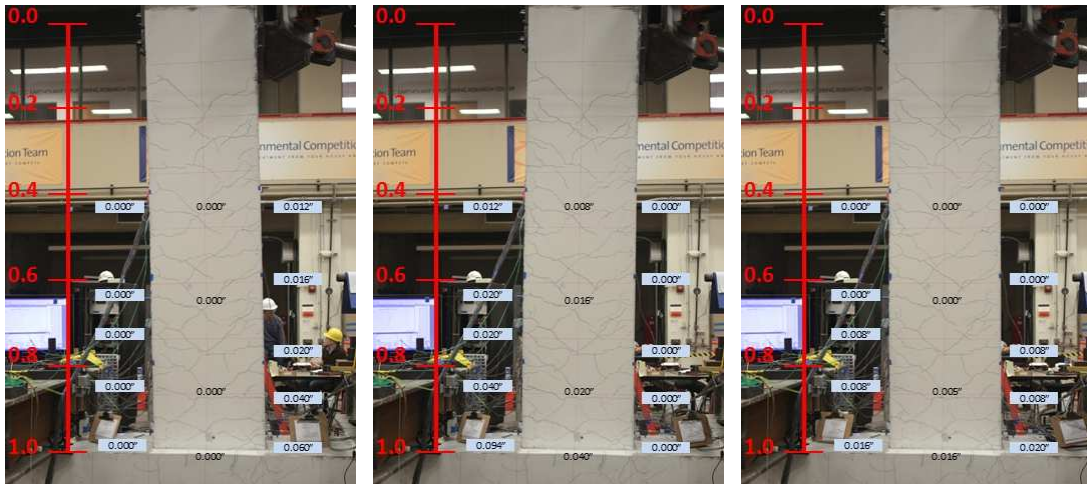Figure C-25: Measured Crack Widths at Drift Ratio of 1.25% – Specimen SBM100

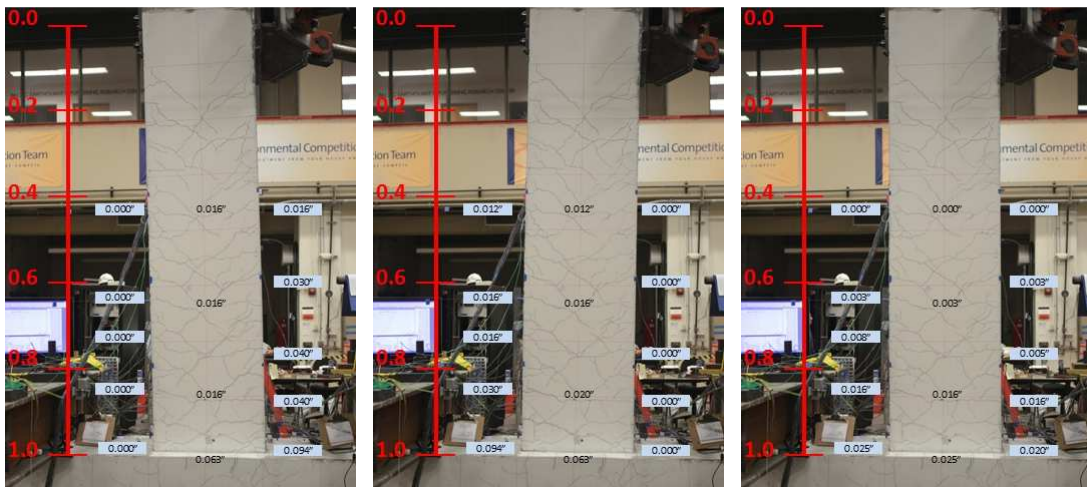Figure C-26: Measured Crack Widths at Drift Ratio of 1.75% – Specimen SBM100

Figure C-27: Measured Crack Widths at Drift Ratio of 2.45% – Specimen SBM100

Figure C-28: Measured Crack Widths at Drift Ratio of 3.45% – Specimen SBM100
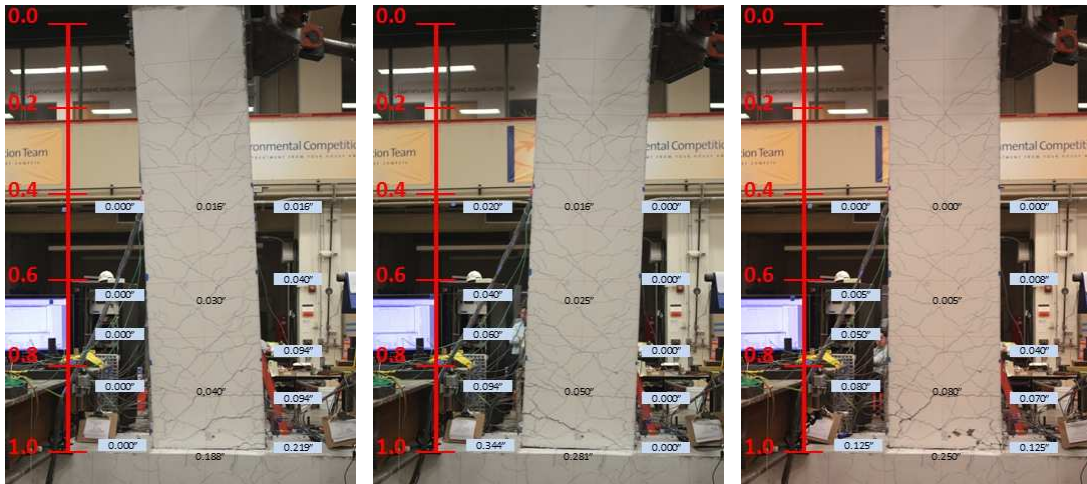
Figure C-29: Measured Crack Widths at Drift Ratio of 4.85% – Specimen SBM100